DIPLOMARBEIT

Assessing Activity and Dose Values computed by Image-Based Quantification of Y-90 SPECT/CT Data

zur Erlangung des akademischen Grades

Diplom-Ingenieur

im Rahmen des Studiums

Technische Physik E 066 461

eingereicht von

Konrad Lotter, BSc

Matrikelnummer 01226180

ausgeführt am Atominstitut
der Fakultät für Physik der Technischen Universität Wien

in Zusammenarbeit mit Hermes Medical Solutions, dem Bundesamt für Eich- und Vermessungswesen und dem Allgemeinen Krankenhaus der Stadt Wien

Betreuung

Univ.Prof. Dr.techn. Franz Josef Maringer

Wien, 29.01.2019

(Unterschrift Verfasser) (Unterschrift Betreuer)

Acknowledgement

No scientific project ever really is the work of one person alone, but always consists of contributions from several people, some of whom I want to thank at this point.

First of all I want to express my profound thanks to my supervisor Franz Josef Maringer for his mentoring during this project and before. Without the need to check back with him at every little step I performed, he offered feedback and ideas whenever necessary. I am also very thankful for the opportunities of introducing my work to a larger audience he created.
Additionally I thank Karin Poljanc (ATI) for her help during the starting phase of this project and Hannah Wiedner (BEV) for her feedback on the abstracts and presentations.

I am also most grateful to Markus Diemling of Hermes Medical Solutions, who not only arranged the organisation of this project with Hermes and the AKH, but who took the time to explain the details of Y-90 SPECT in the beginning and to comment and help whenever necessary afterwards. Moreover I appreciate the work of the team at Hermes and especially of Antti Sohlberg in the background.

Additionally I would like to thank the team at the Department of Nuclear Medicine at Allgemeines Krankenhaus Vienna for providing the means and facility to perform this study on SIRT dosimetry. I am especially thankful to Alexander Haug for providing the patient data and details about the treatment and to Markus Raidl and also to Patrick Binder for their help with the phantom measurements.

Unluckily the measurements on an anthropomorphic liver phantom could not be performed in time to include them in this thesis, but they will be part of a publication at ICRM 2019. Therefore my sincere thank you also goes to Jon Gear of the Institute for Cancer Research London for his kind offer to lend me the liver phantom and his help during shipment and afterwards.

To present my work at the MRT Dosimetry workshop in Prague last September was a great opportunity and also gave me lots of new ideas and approaches. Therefore I want to express my thanks to Österreichischer Verband für Strahlenschutz for covering my expenses on the journey to Prague.

Last but not least my gratitude goes to my family and friends for their encouragement and support during the months it took me to complete this work.

Abstract

Selective internal radiation therapy (SIRT) is a promising treatment for liver carcinoma by injecting Y-90 bearing microspheres in the hepatic artery. Typical challenges of dose calculations involving internal radiotherapy do not apply, as the spheres get trapped permanently in the micro-vessels. Therefore, it is imminently important to determine activity and dose with an accurate and traceable method.

As Y-90 is a pure beta-emitter and decays without emitting any gamma radiation conventional SPECT/CT cannot be performed and the continuous bremsstrahlung spectrum must be utilized to acquire SPECT/CT images. In this study the commercially available software package HybridRecon (Hermes Medical Solutions) is used for evaluation of phantom measurements and data from 17 patients treated at AKH Vienna (with Y-90 activities ranging from 0.58 GBq to 2.77 GBq). The Monte Carlo based approach for scatter and attenuation correction and collimator modelling allows quantification and yields activity concentration data.

The whole dataset was analyzed and a large influence of the volume of interest threshold selection on the resulting activities was found. To counter this problem a mathematical relation between threshold and activity was introduced. The accuracy of the computed results was verified by comparing applied and measured activities and the under-estimation of the activity concentration was quantified.

Following the EANM guidelines an uncertainty budget was calculated for all relevant cases considering the influence of the different factors on the resulting uncertainty.

Using the established formulae and additional estimations for the tumour volumes pre-treatment dose calculations were performed. Those results were compared with dose values obtained from the quantified SPECT images. Different approaches for obtaining dose value from the activity concentration data were evaluated and local deposition of all energy was assumed, because of the very limited range.

The comparison showed very good agreement within the uncertainty range for measured and calculated doses for the body phantom and also plausible results for the patient dataset.

In conclusion, this study is a proof of concept of quantitative Y-90 SPECT reconstruction with credible results for measured activities in phantoms and patients. Activity concentration values can be obtained from the quantified SPECT images and can be used to compare the internal absorbed dose with pre-treatment calculations. Different factors can be allowed for in an uncertainty budget and therefore a traceable method for activity and dose evaluation is made available. In future studies a Monte Carlo based 3D-dose model including interactions could be envisaged.

Zusammenfassung

Selective internal radiation theraphy (SIRT) ist eine vielversprechende Behandlungsmethode für verschiedene Formen von Leberkarzinomen. Hierbei werden wenige Mikrometer große Y-90-haltige Mikrosphären in die Leberarterie injiziert mit dem Ziel, durch hochenergetische Betastrahlung tumoröses Gewebe zu schädigen. Da sich die Sphären in der Mikrovaskulatur verfangen und permanent in der Leber verbleiben, müssen viele Herausforderungen der Dosimetrie in anderen Formen der molekularen Radiotherapie nicht berücksichtigt werden. Umso wichtiger ist es daher auf eine valide Methode zur Dosisberechnung zurückgreifen zu können.

Durch die Verwendung des kontinuierlichen Bremsstrahlungsspektrums kann SPECT/CT Bildgebung betrieben werden, obwohl Y-90 keine Gammastrahlung emittiert. Im Zuge dieser Arbeit wurde die kommerziell verfügbare Software HybridRecon von Hermes Medical Solutions (Stockholm, Schweden), zur Rekonstruktion verwendet. Durch die auf Monte-Carlo Algorithmen gestützte Simulation mit vollständiger Streuungs-, Absorptions- und Kollimator-Modellierung können quantitative Ergebnisse erzielt werden. Messungen an einem Jaszczak und einem NEMA IEC Body Phantom sowie ein Datensatz von SIRT Patienten des AKH Wien (verabreichte Aktivitäten zwischen 0,55 und 2,77 GBq) wurden damit ausgewertet.

Da ein großer Einfluss des gewählten Thresholds auf die gemessene Aktivität festgestellt werden konnte, wurde der Datensatz mit mehreren reproduzierbaren Thresholds ausgewertet und die gemessene Gesamtaktivität mit dem tatsächlichen Wert verglichen. Innerhalb der Messunsicherheit wurden überwiegend gute Übereinstimmungen erzielt und somit ein prinzipielles Funktionieren der Rekonstruktion erwiesen. Weiters wurden gemessene und gerechnete Werte für die Aktivitätskonzentration verglichen und ein Unsicherheitsbudget nach den EANM Guidelines wurde erstellt.

Mit den bekannten Formeln zur Dosisbestimmung und unter Zuhilfenahme von zusätzlich ermittelten Lebervolumina konnte ein Vergleich zwischen berechneten und gemessenen Dosen durchgeführt werden. Letztere konnte aus der Aktivitätskonzentrationsverteilung der SPECT Bilder ermittelt werden und verschiedene Herangehensweisen zur Auswertung wurden angewandt. Unter Zuhilfenahme eines Korrekturfaktors konnte eine gute Übereinstimmung zwischen gerechneten und gemessenen Dosen beim Body Phantom und plausible Ergebnisse im Patientendatensatz erzielt werden. Für alle Dosen wurde ausschließlich eine lokale Abgabe der Energie angenommen.

Zusammenfassend belegt diese Arbeit, dass quantitative Y-90 SPECT Bildgebung funktioniert und glaubhafte Resultate für Aktivitäts- und Dosiswerte liefert. Durch die Aufstellung eines Unsicherheitsbudgets und unter Berücksichtigung von Korrekturen steht eine nachvollziehbare Methode zur Verfügung, um Dosisberechnungen vor der Behandlung zu validieren.

Erklärung

Ich erkläre eidesstattlich, dass die vorliegende Arbeit von mir selbstständig und nach den anerkannten Grundsätzen wissenschaftlichen Arbeitens verfasst wurde. Es wurden ausschließlich jene Quellen und Hilfsmittel, insbesondere jene Literatur, verwendet, die als solche kenntlich gemacht wurden.

Common Abbreviations

BSA	body surface area
CT	computed tomography
EANM	European Association of Nuclear Medicine
EMPIR	European Metrology Programme for Innovation and Research
HCC	hepatocellular carcinoma
LOR	line of response
MAA	macroaggregated albumin
ME	mid-energy
ML-EM	Maximum Likelihood Expectation Maximisation
MRT	molecular radiotherapy
OSEM	Ordered Subsets Expectation Maximisation
PET	positron emission tomography
PM	photomultiplier
ROI	region of interest
SIRT	selective internal radiation therapy
SPECT	single photon emission computed tomography
SPECT/CT	combined SPECT and CT imaging
SUV	standardized uptake value
TACE	transarterial chemotherapy
VOI	volume of interest

Contents

1 Introduction

Hepatocellular carcinoma (HCC) is the sixth most common form of cancer with approximately 782 000 thousand new cases worldwide in 2012. Moreover patients with HCC diagnosed at later stages have usually a very poor prognosis and the disease is almost always fatal, causing HCC to be the second most deadly cancer type. (Wang, et al., 2017)

Surgical resection or liver transplantation are considered to be the best treatments, but only between 10 % and 20 % of patients are applicable, as liver damage due to other diseases often prohibits this sort of treatment, but is also very common in HCC patients. External radiation beam therapy is equally often not feasible, because of the danger of damage to the healthy parts of the liver. For external doses to the liver of 40 Gy there is already a 50 % chance of radiation-induced liver disease. (Hsieh, et al., 2016)

This leaves transarterial embolization therapies as the main treatment option. Transarterial chemotherapy (TACE) is the standard procedure and manages to prolong the patients' survival. However not all patients are qualified for this therapy and very strong side effects can occur severely limiting the patients' quality of life. (Wang, et al., 2017)

1.1 Selective Internal Radiation Therapy

Another approach that has been increasingly used over the last couple of years is selective internal radiation therapy (SIRT)[1], a treatment, where Y-90 bearing microspheres are injected into the hepatic artery and irradiate the tumour. The basis of this procedure is the fact that tumourous tissue is supplied via the hepatic artery, while healthy liver tissue mainly receives blood from the portal vein. Normally activities ranging between 1 GBq and 3 GBq are injected consisting of millions of glass or resin-based microspheres bearing Y-90. The blood flow transports the spheres towards the tumours and into smaller vessels, where they get trapped permanently in the microvasculature. Therefore in this treatment only the physical half life needs to be taken into account as the microspheres take no part in the metabolism. The details of the clinical practice will be discussed further in section 2.5 .

Y-90 is a pure beta-emitter decaying into the stable Zr-90 with a half-life of 64.00 h and a mean beta energy of 933 keV. Additionally there is a very low probability ($1.4 \cdot 10^{-6}$) for a decay into an exited state and a subsequent gamma decay emitting 2186 keV radiation. In this process pair production can occur. (Browne, 1997)

[1] Sometimes also referred to as TARE (=transarterial radioembolization) in the literature

1.1.1 History of SIRT

Yttrium was discovered in the late 18th century as part of a new mineral named Ytterbite after its site of occurrence near Ytterby in Sweden. In the 1950s different studies by Biermann, Breedis and Young established that liver tumours are supplied mainly via the hepatic artery, while healthy tissue receives its blood supply from the portal vein. Later research discovered that more than 80 % and less than one third of the blood is supplied via the hepatic artery for cancerous and healthy tissue respectively. This is the basis for any kind of selective embolization treatment of liver tumours. (Westcott, et al., 2016)

After previous studies on rats by Grady et al, Norman Simon published the first paper on Y-90 treatment of humans in 1968. He treated 5 patients with carcinous liver metastasis in The Mount Sinai Hospital, New York and injected activities varying between 15 mCi and 50 mCi (= 0.55 GBq and 1.85 GBq) of carbonized Y-90 bearing microspheres into the hepatic artery. As illustrated in figure 1, methods quite similar to today's clinical practice were used for diagnostics and post treatment imaging. Simon used Au-198 scintigraphy scans for localization of the tumour and did a bremsstrahlung scan for verifying the distribution of the Y-90 after treatment. The device used for the latter was a rectilinear scanner yielding low quality planar images, but the possible advantages of a gamma camera are already mentioned in the article.

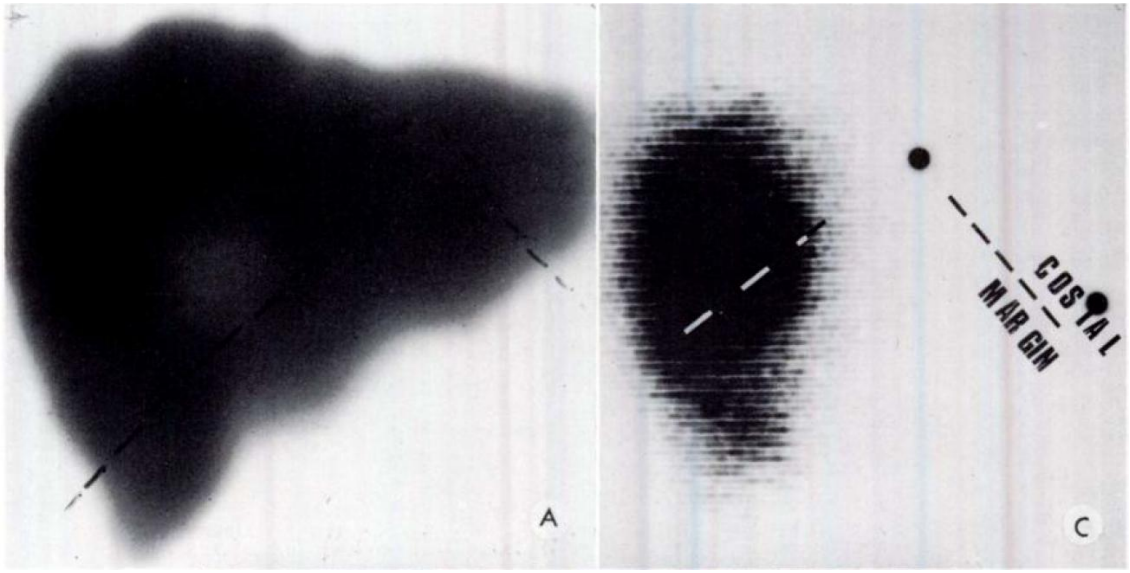

Figure 1: Simon's illustrations of an Au-198 Scintigraphy scan (left) and a Y-90 bremsstrahlung scan from a rectilinear scanner (right) (Simon, et al., 1968)

Simon also did some rudimentary dosimetry calculating doses for a homogeneous distribution of the radionuclide in the liver with a formula very similar to the one given in section 3.8.1. Additionally small LiF dosimeters were inserted in the liver during one treatment showing a large gradient between the doses to tumour and healthy liver tissues.

All the same the medical outcome of the treatment was mixed with an improvement of the patients' syndromes reported in most cases, but severe radiation damage to the stomach due to incorrect placement of the catheter observed in two others. (Simon, et al., 1968)

These results and the unpromising outcome of several other studies led to a decrease of interest in SIRT in the following decades. While Simons' main problem of imprecise application of activity could be solved in later years with advanced catheterization techniques other studies reported radiation damage to the liver and gastrointestinal tract. Furthermore leakage of microspheres caused yttrium to escape and get into the bone marrow leading to the deaths of some patients.

Subsequent research focused on a deeper understanding of the vascular structure of the liver and its tumours and on the development of new methods to bind the yttrium in the microsphere and avoid the above mentioned problems. Additionally Meade et al and later Anderson investigated the optimal size of microspheres and determined it to be about 40 µm. (Westcott, et al., 2016)

In the late 1980s and early 1990s the first clinical studies were made, using glass or resin-based microspheres similar to those still in use. Herba reported a stabilisation of the disease or a slowing of the progression in his 15 patient trial and introduced the idea of a pre treatment Tc-99m-MAA scan to determine the lung shunting fraction (see section 2.2). In another series of trials Gray introduced the name SIRT for the procedure and worked on optimizing the applied dose. In a large scale study with 70 patients a favourable tumour response and a mean extension of progression free time by 4.4 months was found in comparison to chemotherapy.

Based on the favourable outcome of this and other studies the FDA (Federal Drug Administration) approved the glass microspheres TheraSphere currently produced by Nordion (Ontario, Canada) in 1999 and the resin-based variation manufactured by Sirtex Medical Ltd. (north Sidney, Australia) in 2002. This approval is the basis for large scale application of SIRT and since then many studies are aiming to evaluate the effectiveness and the best use of this treatment. (Westcott, et al., 2016)

1.1.2 Results of recent Clinical Trials

Recently several large clinical studies on the use of SIRT for both HCC and metastatic liver cancer have ended. In three studies named FOXFIRE, FOXFIRE-Global and SIRFLOX comprising 14 different countries and 1103 patients totally the effects of treatment of metastatic colorectal cancer in the liver with chemotherapy versus combined SIRT and chemotherapy treatment were evaluated. As visible in figure 2 no significant variation of overall survival was found. However patients treated also with SIRT enjoyed a slightly prolonged time of no liver cancer progression. Additionally a definite advantage in adding

SIRT treatment was found for right sided cancer, which has a poorer prognosis and this is currently investigated further. Following these results future application will probably focus more on selecting specific patient groups that could significantly profit from SIRT treatment. (Wasan, et al., 2017)

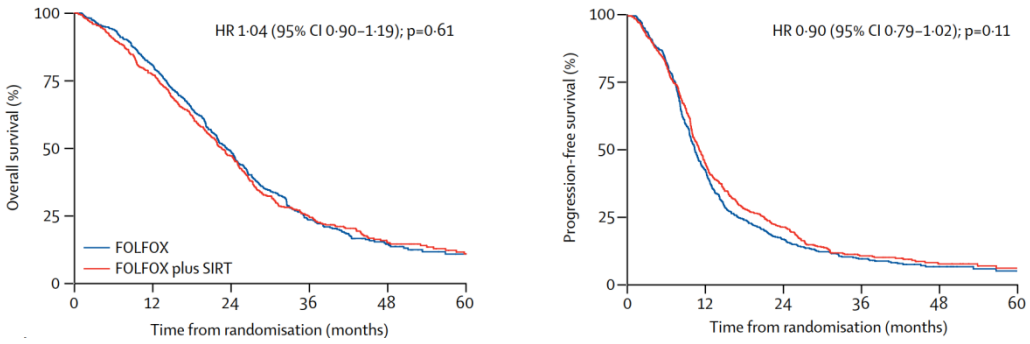

Figure 2: comparison of treatment results with chemotherapy (blue) and a combination of chemotherapy and SIRT (red) (Wasan, et al., 2017)

For the treatment of HCC with SIRT similar results were found in two large studies (SARAH and SIRveNIB) involving 819 patients, who were either treated with chemotherapy only or a combination of chemotherapy and SIRT. Again no positive effect on overall survival was found. However a prolonged cancer progression free time and a better overall tumour response could be proved. SIRT also has less severe side effects and offers a better quality of life to the patients. (Hui, et al., 2018) Moreover a recent retrospective research indicated that a SIRT treatment can improve the chances of surgical liver resection afterwards. (Pardo, et al., 2017)

1.2 MRT Dosimetry Project

The project M*etrology for Clinical Implementation of Dosimetry in Molecular R*adiotherapy (short MRT Dosimetry) is part of the *European Metrology Programme for Innovation and Research* (EMPIR) and is a joint effort of 6 national metrology institutes, 13 clinical facilities and many scientific and industrial collaborators. It is a follow-up of the MetroMRT project (*Metrology for molecular radiation therapy*), which was running from 2012 to 2015 and continues to address the same field. (MRT Dosimetry, 2017)

Molecular radiotherapy (MRT) comprises a group of treatments, amongst them SIRT, where an unsealed source (usually an alpha- or a beta-emitter) is inserted into the body, similar to the application of radioactive tracers in nuclear imaging, but in larger doses. Either because the agent is only absorbed selectively or because of the way of insertion the radionuclides are enriched in the tumourous regions and should deliver a far larger dose to tumours than to healthy tissue. Examples are the widely used radioiodine therapy for thyroid cancer, where I-131 is ingested and mainly absorbed in the thyroid gland, or treatment for bone metastasis with Ra-223 or Sa-158 that is absorbed into the bone, because of its chemical similarity to calcium.

More sophisticated methods like radiopeptite therapy and the bonding of radionuclides to modified antibodies are also performed often using radionuclides like Lu-177. Unlike SIRT in most forms of MRT the radionuclide is partly washed out and to establish the effective half life and the time dependent distribution in the body becomes one of the main challenges. (Buscombe, et al., 2012)

Until the start of the MetroMRT project activities and not doses were the key quantity normally used in MRT treatment. This was mainly due to the very sophisticated dosimetry necessary and the absence of any standardized procedures. However it was shown that the dose to the tumour could vary as much as two orders of magnitude consequently leading to unpredictable treatment results.

In the MetroMRT project the practical experience from nuclear medicine was for the first time combined with the input from metrology and the basis for a change was made. Utilizing the gamma decays or in some cases bremsstrahlung radiation quantitative imaging can be performed yielding precise data of the radionuclide concentration in different parts of the body. If several images are taken and the biological mechanisms are known absorbed doses can be calculated. For this purpose a primary dose standard for liquid radionuclide solutions was also developed in the course of the MetroMRT related work. (MetroMRT, 2015)

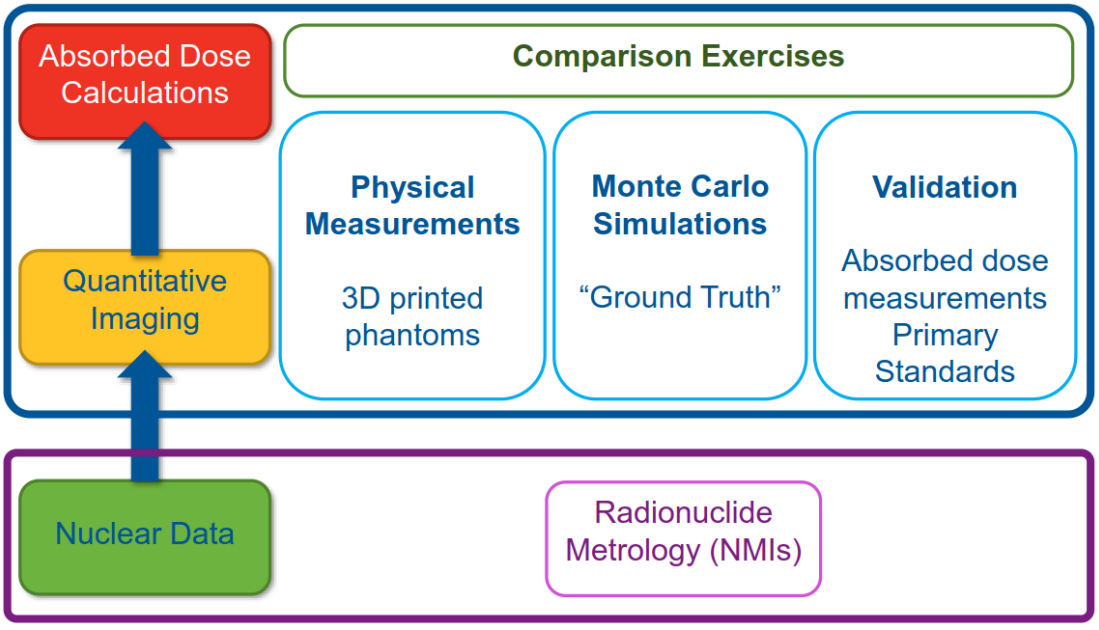

Figure 3: structure and main objectives of the MRT Dosimetry project (Robinson, 2018)

The follow-up project MRT Dosimetry focuses on the clinical implementation and is closely working together with MRT clinics. In the course of the project a traceable dosimetric chain should be established as shown in figure 3. The efforts made in this context will also help the involved centres to comply with the EC Directive 2013/59/EURATOM, which makes the implementation of dosimetry in MRT compulsory.

To achieve this goal metrological institutes and clinics are working closely together. Among other objective the Y-90 branching ratio (necessary for PET imaging) should be established more precisely, anthropomorphic phantoms for calibration measurements are developed with novel 3D printing methods. One of these is the 3D liver phantom AbdoMan developed by Jonathan Gear and colleagues. Using a 3D printing technique a realistic representation of the liver and abdomen could be created and measurements verifying dose calculations and quantification can be performed. (Gear, et al., 2016) To increase the comparability between different centres comparison exercises are performed and standardized methods (e.g. for calculating uncertainties) are introduced. Finally new and more accurate ways of determining the dose utilizing Monte Carlo simulations and detailed modelling of the metabolism are developed. (MRT Dosimetry, 2017)

This thesis covers challenges and approaches into more precise dosimetry in SIRT and should therefore be understood as a contribution to the MRT dosimetry project. During a workshop in Prague in September 2018 work in progress and results were presented and important input was acquired. More details about this can be found in the appendix, section C.1 .

1.3 Objectives of this Project

While quantitative evaluation of Y-90 PET imaging does exist, Y-90 Bremsstrahlung SPECT is typically only used for qualitative evaluation of the SIRT treatment and to verify the correct distribution of the applied activity. To the best of my knowledge quantitative evaluation of Y-90 SPECT using HybridRecon and a large set of patient images is performed for the first time in this thesis.

The objective is to evaluate the quantitative reconstruction performed in HybridRecon, to further use the acquired data for an estimation of the dose from the SPECT images and to compare these with calculated values. Ideally a traceable technique taking into account metrological aspects can be developed for evaluating doses in SIRT.

In order to achieve this, phantom measurements were performed and a dataset of 17 patients made available by Allgemeines Krankenhaus Vienna was evaluated in this thesis. Total activity, activity concentration, tumour volumes and doses were obtained after the reconstruction of all images. In this thesis several criteria for the construction of volumes of interest and different techniques for dose evaluation using Y-90 SPECT images were developed. The correction of the so called spill-out effect using a recovery factor was investigated and an uncertainty budget was created by adapting the EANM guidelines (Gear, et al., 2018) to fit all relevant cases.

A proof of concept for quantitative reconstruction with HybridRecon can be concluded from the results in section 3.5 and credible results for the comparison of measured and calculated doses are obtained for the patient dataset (see section 3.9). Furthermore good agreement between theoretical predictions and phantom measurements is observed for both the evaluation of activity (section 3.3) and the use of dose values corrected with a recovery coefficient (section 3.8.5). The detailed consideration of uncertainties (see sections 3.2 and 3.8.3) and the effort made in this thesis to avoid the common issue in nuclear medicine of arbitrarily defining volumes of interest (section 3.4.1) yield traceable results and make the used methods easily reproducible.

2 Materials and Methods

2.1 SPECT Imaging

Single photon emission computed tomography usually referred to as SPECT is a technique for acquiring 3D images of an activity distribution in a patient's body. Normally discrete gamma rays are detected. One example is the 140 keV photo peak of Tc-99m, which is a short lived isotope and the "working horse" of nuclear imaging. However it is also possible to utilize bremsstrahlung from fast beta-particles as is done with Y-90 and will be discussed later in more detail.

A SPECT device consists of one or two gamma cameras (also called Anger camera after its inventor), which are mounted on a gantry and rotate around the imaging table producing a series of images from different angles. Gamma cameras have been in clinical use for several decades to supply 2D images and work according to the design depicted in figure 4.

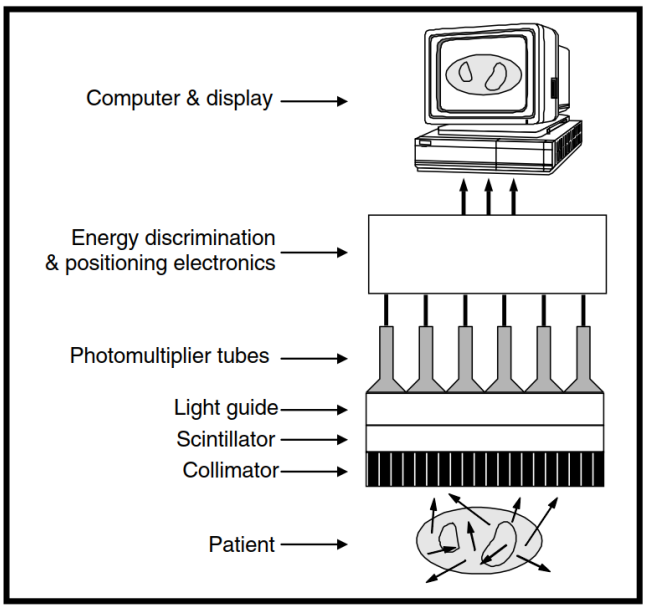

Figure 4: schematic design of a gamma camera, as also used in SPECT imaging (Zeng, et al., 2004)

The gamma radiation is detected in a scintillator crystal usually consisting of thallium doped sodium iodide NaI(Tl). There flashes of visible (or near UV) light are induced and transmitted through a light guide into an array of photomultipliers (PM). The events are amplified and detected as current. Additionally it is possible to determine the energy of the incoming gamma photon by summing over all events detected simultaneously by neighbouring PMs. Using this information incoming rays of energies other than the selected window around the expected peak can be discarded. However it is not possible to focus gamma radiation like light in a photographic camera. In order to be still able to

get a reasonably well defined image collimators are used. The most common type is a parallel hole collimator where a lead foil (called septa) separates an array of hexagonal holes. Photons arriving perpendicularly to the detector plane are transmitted, while those from oblique angles should be absorbed in the lead. However different types of unwanted detection can still occur, hence making correction and modelling of the collimator necessary as further described in section 2.3 . (Zeng, et al., 2004)

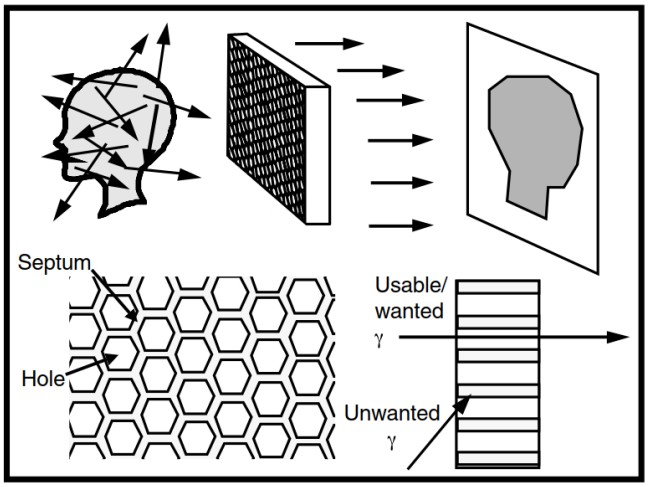

Figure 5: design of a parallel hole collimator and one example of unwanted detection. (Zeng, et al., 2004)

A photon coming through the collimator is then detected in the scintillator as described above and can be mapped to position coordinates according to which PM in the array detected it. With adequate acquisition times this basic principle leads to the formation of an image in the camera.

2.1.1 Basic Concept of Tomographic Image Reconstruction

In this section a basic explanation of two dimensional image reconstruction will be given following the description in Kinahan, et al., (2004). An idealised case is described and physical effects like unwanted detections or scattering, the finite diameter of the collimator holes and the finite field of view of the imaging device will not be considered. The principle can be extended to the three dimensional case fairly easily therefore describing the real SPECT reconstruction process. Detailed explanations and a stringent mathematical description can be found in the literature (e.g. Figl, (2014)).

With these assumptions every hole in a collimator is only sensitive to a well defined one dimensional line of response (LOR) that can be described as a line integral

$$p(x_r, \Phi) = \int_{-\infty}^{\infty} f(x,y)dy \quad \text{with} \quad \begin{pmatrix} x \\ y \end{pmatrix} = \begin{pmatrix} cos\Phi & -sin\Phi \\ sin\Phi & cos\Phi \end{pmatrix} \begin{pmatrix} x_r \\ y_r \end{pmatrix}$$

The main problem of image reconstruction is to calculate an unknown $f(x,y)$ from a known $p(x_r,\Phi)$. For a fixed direction Φ the line integrals for all possible x values form a projection as visible in figure 6a. A set of projections for all possible Φ values forms a so called sinogram (depicted in figure 6b). The name has been chosen, because a fixed point (x_0,y_0) in the image can be described by the set of all lines of response passing through it with the equation $x_r = x_0\, cos\Phi + y_0\, sin\Phi$

The transformation $f(x,y) \rightarrow p(x_r,\Phi)$ is called Radon or xray transform[2] in two dimensional imaging.

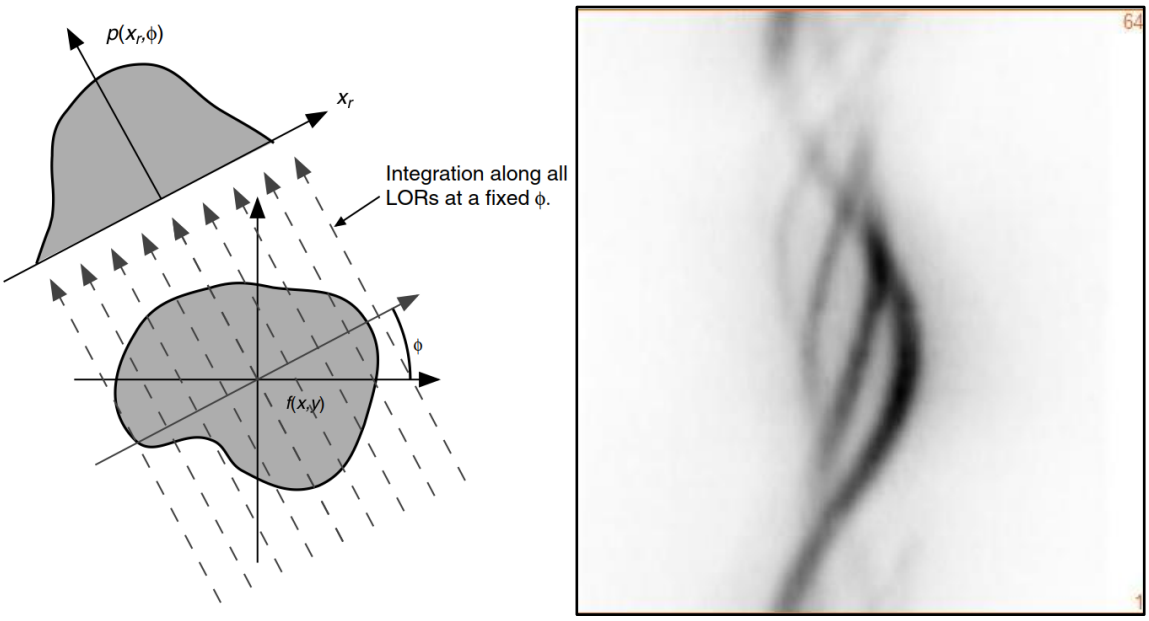

Figure 6a: schematic drawing of a projection along all possible LORs for a fixed Φ (Kinahan, et al., 2004) 6b: Sinogram of a SPECT image of the NEMA IEC Body Phantom created in HybridRecon

The so called central section theorem[3] shows according to Kinahan, et al., p. 427 : *"[...] that the Fourier transform of a one-dimensional projection is equivalent to a section, or profile, at the same angle through the center of the two-dimensional Fourier transform of the object."*

$$P(v_x,v_y) = \widehat{p(x_r,\Phi)} = \int_{-\infty}^{\infty} p(x_r,\Phi)\mathrm{e}^{\mathrm{i}2\pi \mathrm{x_r} \mathrm{v_{xr}}}\,\mathrm{dx_r}$$

$$= \int_{-\infty}^{\infty}\int_{\infty}^{\infty} f(x,y)e^{i2\pi x_r v_{xr}}\,dx_r dy$$

$$F(v_x,v_y) = \widehat{f(x,y)} = \int_{-\infty}^{\infty}\int_{\infty}^{\infty} f(x,y)e^{i2\pi(xv_x+yv_y)}dxdy$$

[2] In 2D those transformations are identical, in 3D they have to be distinguished.
[3] Figl calls it projection slice theorem

It can be shown that $\Rightarrow P(v_{xr}, \Phi) = F(v_x, v_y)|_{v_{yr}=0}$

This means as also illustrated in figure 7 that the Fourier transform of the known $p(x_r, \Phi)$ is equivalent to an unknown Fourier transform $\widehat{f(x,y)}$ of a section of the image defined by the angle Φ. Therefore the two dimensional inverse Fourier transform of P will describe a section of the object that has been imaged.

This reconstruction algorithm is called direct Fourier method, but yields unpromising results in real operation due to the limited number of angles available in clinical imaging. Another approach is the so called backprojection were a constant value is inserted along all LORs forming an approximation of the initial object. Once again contrasts are very low and star shaped artefacts appear due to the finite number of images and physical effects not considered in the theoretical discussion. Therefore the solution most often used in clinical practice is the filtered backprojection, where frequencies are filtered in the Fourier space. High frequency components related to smaller structures in the image are enhanced, while lower modes are suppressed or cut off enhancing contrast and structures at the cost of an increased noise level. (Gemmell, et al., 2003)

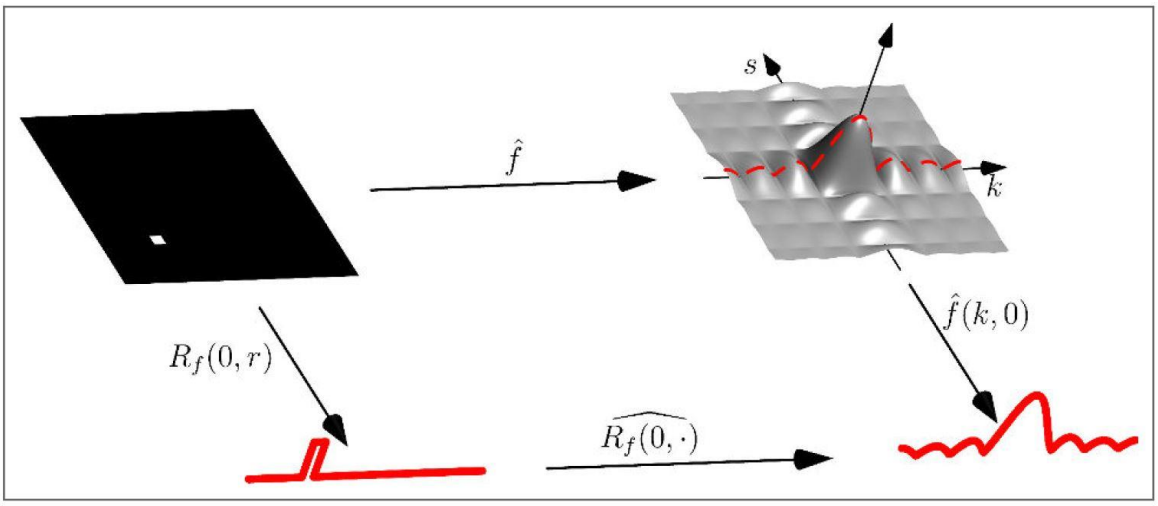

Figure 7: illustration of the central section theorem: the Fourier transform $\widehat{R_f}$ of the projection R is equal to the Fourier transform $\hat{f}$ of a section of the image, the nomenclature is slightly different from above (Figl, 2014)

However HybridRecon, the software employed for reconstruction in this project (see section 2.3), uses an iterative OSEM Algorithm. In iterative reconstruction the image is divided into small parts, usually quadratic pixels for 2D approaches and voxels in the 3D case.

A system model H relating the image to the data needs to be established in order to describe the relation between the i[th] projection (p_i) and the activity in the j[th] voxel (f_j) as follows:

$$\overline{p_i} = \sum_{j=1}^{N} H_{ij} f_j$$

Additionally a statistical model for the data has to be established describing how the individual measurements vary around their mean values. It is common to use a Poisson distribution as this describes the behaviour of photons. But variations of this model as well as approaches using Gaussian or other distributions are also in use. Next an objective criterion for the best image has to be found, which is commonly and also in the OSEM algorithm a maximum likelihood approach. This yields unbiased results that will equal the real value after an infinite number of iterations. (Kinahan, et al., 2004)

Here the Maximum Likelihood Expectation Maximisation (ML-EM) will be described as it is the basis for the OSEM algorithm:

$$f_j^{(n+1)} = \frac{\hat{f}_j^{(n)}}{\sum_{i'} H_{i'j}} \sum_i H_{ij} \frac{p_i}{\sum_k H_{ik} \hat{f}_k^{(n)}}$$

$\hat{f}_i^{(n)}$ current estimate of the i[th] voxel

$f_i^{(n+1)}$ next estimate based on the current one

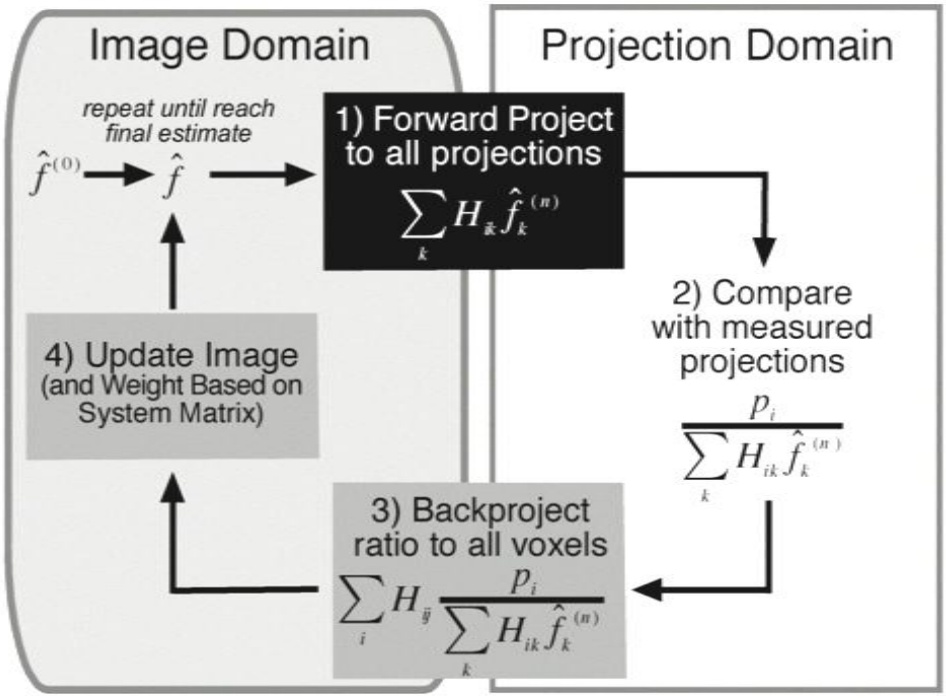

Figure 8: flow diagram of the ML-EM algorithm (Allesio, et al., 2006)

The algorithm starts with an initial guess for the image f_0 usually a uniform distribution over all voxels and creates a projection from it, known as forward projection. This simulated projection is then compared to the real one and multiplied with a factor in order to approach the real data. Next the corrected projection is backprojected to form an image, which is used to improve the previous estimate by applying a weighted correction factor to it. Then the new image is once again used as basis for a forward projection creating the next simulated projection and so forth as illustrated in figure 8.

With this technique the low frequency components in the Fourier space representing large structures are computed within a few runs of the algorithm, but it takes between 20 and 50 iterations to get a good quality solution. As this algorithm involves a forward and a backprojection in each iteration computation times can be high. (Allesio, et al., 2006)

To overcome this challenges the Ordered Subsets Expectation Maximisation Algorithm (OSEM) was introduced by Hudson and Larkin in 1994. (Hudson, et al., 1994) The OSEM algorithm is a slight modification of the ML-EM method dividing the image into a number of subsets.

$$f_j^{(n+1)} = \frac{\hat{f}_j^{(n)}}{\sum_{i' \in S_b} H_{i'j}} \sum_{i \in S_b} H_{ij} \frac{p_i}{\sum_k H_{ik} \hat{f}_k^{(n)}}$$

During the backprojection steps the summation is done only over the subset S_b resulting in the imaged being updated b times in one iteration for a number b of subsets. This procedure yields good results after only a few iterations converging approximately b times faster than the unmodified ML-EM algorithm.

Further details of the HybridRecon software and the methods of correcting SPECT images will be discussed in the section after the next.

2.2 Imaging in SIRT

Before the application of the microspheres in SIRT preliminary imaging is performed. This usually consists of an angiogram, where a contrast fluid is injected into the vasculature and a CT is performed to make it visible. This is used to identify any branches where microspheres could leak out of the liver into for example the gastro-intestinal tract causing unwanted radiation damage. Additionally the angiogram can allow an estimate of how much of the liver is affected by tumours necessary for the calculation of the optimal Y-90 activity to be applied.

Using Tc-99m-MAA a SPECT scan can be performed prior to treatment. Tc-99m is a widely used radionuclide for SPECT imaging with a half live of 6.00 h and an energy of 142.7 keV. (Browne, et al., 2017) For SIRT pre-treatment it is applied in the form of macroaggregated albumin. Normally activities between 140 MBq and 185 MBq are administered in a way

similarly to the SIRT treatment. The size and behaviour of these particles is very similar to the Y-90 bearing microspheres and the scan is done in order to estimate the ratio of activity uptake in tumours and healthy liver tissue and the so called lung shunting fraction. Because of a connection of the blood vessels some microspheres can escape into the lung causing radiation pneumonia and to evaluate this danger the MAA SPECT is used to estimate the fraction of microspheres likely to move into the lung. (Voutsinas, et al., 2018)

If the lung shunting fraction is higher than 25 Gy preferably 20 Gy or 10 % of the intended dose, depending on the model used for calculation, either the total dose is reduced or some vessels are cauterized prior to the treatment. (Sirtex Medical Limited, 2016) There are also approaches for dosimetry utilizing the MAA SPECT (see for example Botta, et al., (2018)). However the similar uptake of Tc-99m-MAA and SIRT spheres has been questioned in recent years and the validity of approaches relying heavily on Tc-99m is investigated (e.g. Allred, et al., (2018), Lenoir, et al., (2012)).

Normally after the microspheres are administered post-treatment imaging is performed. As Y-90 is a pure beta emitter it is quite challenging to image with two parallel approaches being in use since several years. As mentioned previously a very low probability branch of the decay leads to a high energy gamma emission and consequently to pair-production enabling PET (positron emission tomography) imaging. Although PET is widely considered to be superior to SPECT imaging mainly due to the advanced possibilities of correction for attenuation and scatter, the very low intensity still makes it challenging to perform and does not lead to results as good as in other PET studies.

Additionally SPECT is more readily available at many facilities making the possibility of doing SPECT desirable. This is possible not using any discrete gamma decays, but the continuous bremsstrahlung spectrum generated by the fast electrons. Normally a mid-energy (ME) collimator and an energy window of about 50 – 150 keV are used. Not having a peak to focus on significantly affects image quality and contrast, highlighting the necessity of advanced correction techniques as employed in this study.

2.3 Image Reconstruction with HybridRecon

For this study Hermes HybridRecon Oncology version 2.2.2 is used for the reconstruction and Hermes Hybrid Viewer PDR version 3.0.2 is employed for the evaluation of data. Both programmes are provided by Hermes Medical Solutions (Stockholm, Sweden). HybridRecon is still under development and feedback from this project will be given to Hermes. It is based on a modified OSEM algorithm and was developed by Antti Sohlberg and colleagues. (Sohlberg, et al., 2008), (Sohlberg, et al., 2011), (Porter, et al., 2018), (Bexelius, et al., 2018)

The basic principle of the OSEM algorithm was explained in section 2.1.1 and is expanded by corrections for scatter, attenuation and the response of collimator and detector. The splitting into subsets is achieved by considering the data at different energies. This also helps to overcome the challenge of a continuous spectrum.

2.3.1 Attenuation Correction

The main challenge to image quality in SPECT is incorrect image reconstruction due to attenuation. In tissue the emitted photons experience elastic and inelastic scatter causing changes in direction and energy. The most relevant process for inelastic scatter in this energy range is the Compton effect, where the photons are deflected and loose energy. Because of this, erroneous detections of scattered photons can occur in other parts of the detector and a high number of photons are lost, since they either leave the detector's field of view or are absorbed in the tissue.

Therefore uncorrected SPECT images always show an intensity gradient with the number of counts decreasing from the edges to the centre. In order to get rid of these ring shaped artefacts and to correct for the ostensible decrease in activity uptake with increasing tissue depth an attenuation correction needs to be performed. While this involves rather complex calculations in normal SPECT the process is quite easily accomplished in SPECT/CT.

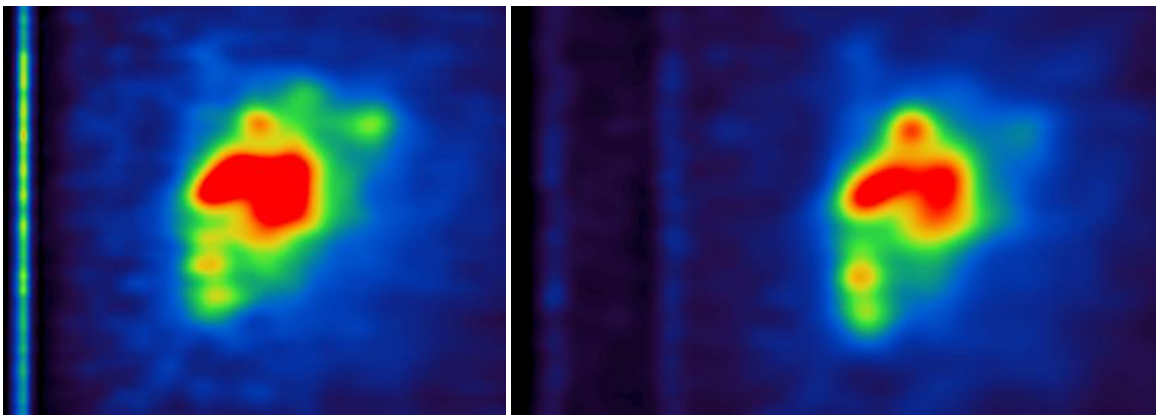

Figure 9: example for the effects of attenuation correction. Patient DB sagitarial view Left: reconstruction with the default software of the Siemens Symbia Intevo SPECT and no attenuation correction, artefacts at the borders are pronounced and forms are distorted. Right: reconstruction with HybridRecon applying attenuation correction results in enhanced image quality

The main advantage of combined SPECT and CT[4] imaging is a common reference for both datasets. On the one hand this allows a simply fusing of SPECT and CT images and centres

[4] *"CT* (= computed tomography, note) *images are acquired by using a high-output x-ray tube and an arc of detectors in a fixed geometry to acquire cross sectional transmission images of the patient as the x-ray tube and detector configuration rapidly rotates around the patient […]"* Resolutions of about 1 mm or less can be achieved. (Patton, et al., 2008)

of high activity can be related precisely to anatomic features. On the other hand CT data can be used as a very accurate representation of attenuation in different body parts.

Each measured intensity I is attenuated as follows

$$I = I_o \cdot e^{\sum_i -\mu_i x_i}$$

I_0	initial intensity
μ_i	effective attenuation coefficient of each tissue type i
x_i	thickness of each tissue region i

Using a reconstruction technique like filtered backprojection an attenuation map (often called μ-map) can be constructed from the CT intensity measurements. Next a conversion into standardized Hounsfield units is made and the different energies used for CT and SPECT need to be addressed. As attenuation is highly energy dependent the attenuation coefficients acquired during the CT scan with x-rays of typical energies lower than those used in SPECT are scaled to match the SPECT energy range. Theoretically this is accomplished by using a simplified representation of the bilinear behaviour of the attenuation coefficients. In clinical practice pre-calculated look-up tables are accessed and allow easy conversions. (Patton, et al., 2008)

Using the corrected attenuation map scaling factors are applied to correct the SPECT image as shown in figure 10.

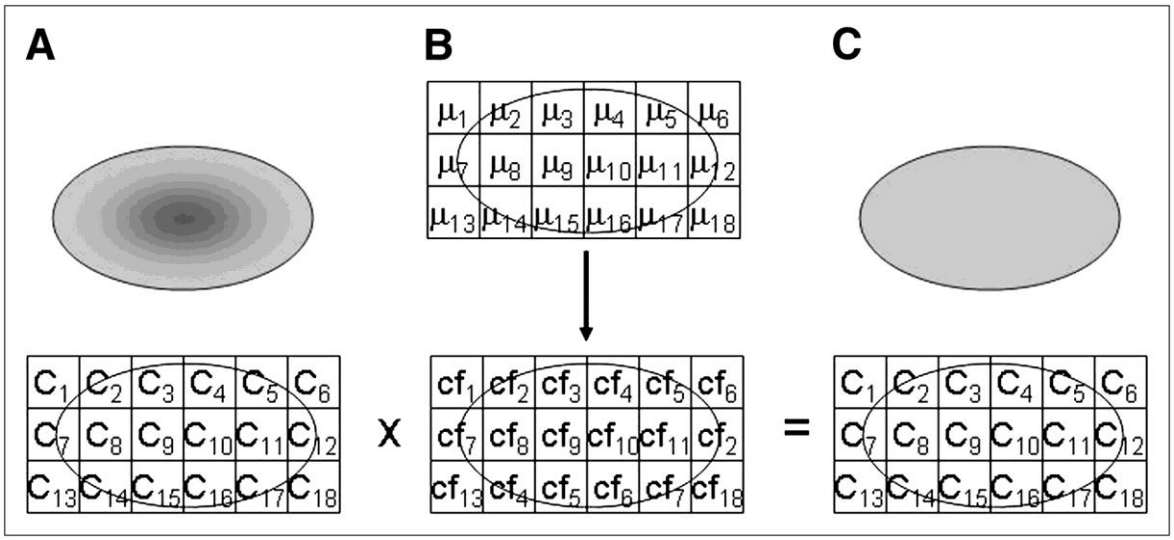

Figure 10: schematic representation of the attenuation correction. Uncorrected SPECT data (A) is multiplied with correction factors acquired from the CT scan (B), yielding a SPECT image with better quality and no gradient in count data (C) (Patton, et al., 2008)

In HybridRecon a rotation-based projector is used for the forward projection. This means that the projection plane is fixed and the image is rotated. This makes the application of attenuation correction very easy as it is only necessary to do a sum of the appropriate

columns of the attenuation map and apply it to each respective voxel. (Bexelius, et al., 2018)

2.3.2 Scatter Correction

A Monte Carlo based scatter correction of the forward projection is performed only for the first two iterations in order to save calculation time. It is based on the principle of convolution-based forced detection. (de Jong, et al., 2001) As visible in figure 11 in this simulation model the paths of a large number of photons are sampled and the response at the detector is simulated. As only one in 10^5 sampled photons would reach the detector without directional constraints the photons are forced to scatter towards the collimator (= forced detection).

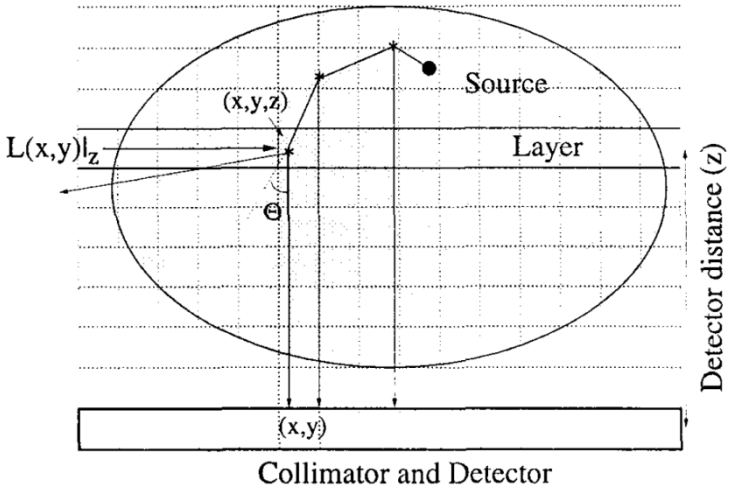

Figure 11: schematic drawing of the convolution based forced detection method. At the interaction site (x,y,z) a copy of the photon is forced to scatter towards the detector and is stored in a sub-projection L(x,y) together with its weight and its scatter position. Next the photon is multiplied with an intensity I_z according to the detector response function. (de Jong, et al., 2001)

An emission distribution map is generated by dividing the counts in each voxel by the total number of counts and from this the starting position of a photon is randomly sampled. It is randomly assigned a direction and an energy value sampled from a pre-calculated bremsstrahlung energy spectrum. The range d is calculated according to $d = -\frac{\ln(r)}{\mu_{Max}}$ where r is a random number and μ_{Max} is the maximum attenuation coefficient in the attenuation map. At the first interaction site a copy of the original photon is generated and forced to follow a path parallel to the collimator hole axis. At the collimator the photon is stored in another sub-projection map and its weight is multiplied to correct for the probabilities of not having been absorbed photo-electrically, not having undergone Compton-scattering, not having been attenuated and having scattered in the desired angle θ in the direction to the collimator.

For the original photon a new path is sampled and at the next interaction site a new copy is again forced to scatter to the collimator. This process is repeated until 10 interactions have happened, the photon energy has decreased below 75 % of the lower limit of the energy window or the photon leaves the density map. (Bexelius, et al., 2018)

2.3.3 Collimator and Detector Response Modelling

To simulate the behaviour of collimator and detector the scattered photons yielded by the forced detection method and stored in sub-projections need to be convoluted with a detector response function. Usually Gaussian models are used for this purpose, but with higher energy photons and no clear energy peak the possible events at the collimator need to be modelled more precisely.

To achieve this without excessive calculation times pre-calculated look-up tables are used. These are generated by another Monte Carlo simulation that models the response to point sources of various energies and with various distances from the detector. For this purpose a parallel hole collimator, hexagonally shaped holes and a rectangular sodium iodine detector crystal are assumed. Next the photons are traced in the collimator following the same delta-tracking algorithm as for the determination of pathlength in the scatter correction algorithm.

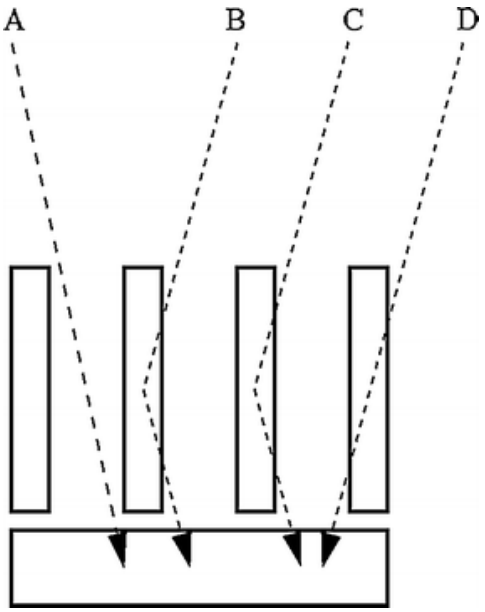

Figure 12: different behaviour of photons simulated in the collimator: A geometric collimation, B Scatter, C x-ray fluorescence, D wall penetration **(Sohlberg, et al., 2011)**

As illustrated in figure 12 four different events are simulated: the direct detection of a geometrically collimated photon, the penetration of the collimator walls, coherent and Compton scatter inside the collimator and the absorption of a photon in the collimator walls causing the emission of lead x-ray photons.

Furthermore the photons are also tracked inside the detector and partial deposition and full deposition of energy are recorded. The final position, where the photon is detected, is calculated as the energy weighted mean of all events caused by this photon and blurred with energy depended Gaussian functions.

With this technique an image of the detected point sources is created, which represents the detector-collimator response function. Those are stored in the look-up tables and accessed for evaluating the scattered photons stored in the sub-projection maps. Distances and energies not represented in the tables are computed by linear interpolation. (Sohlberg, et al., 2011)

After all corrections are applied a projection is formed by summing the convolved layers and the OSEM algorithm is performed as previously explained. During the backprojection, which is also rotation based only attenuation correction and collimator and detector response modelling are applied to save calculating time. The implementation in the GUI and the reconstruction parameters used in this project will be discussed in the next section.

2.4 Practical Example

In this section the practical reconstruction of a SPECT/CT image with HybridRecon is illustrated as an example for the workflow that has been performed during this project for all available images. The example shown is from patient DB, which is part of the dataset of SPECT and CT measurements provided by the AKH Vienna.

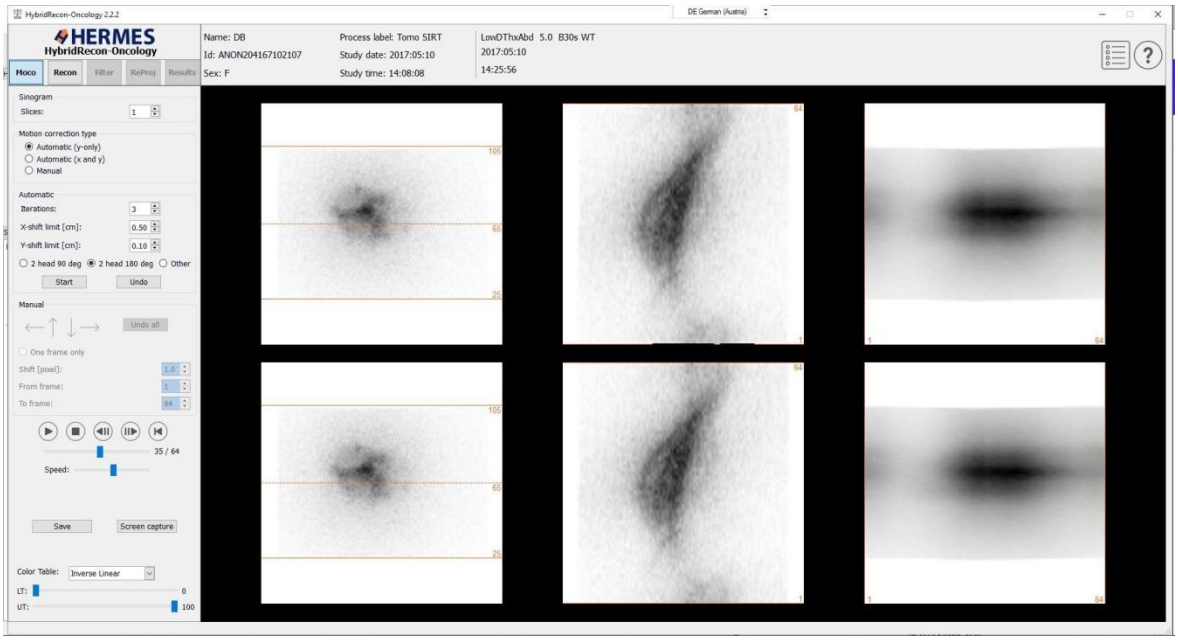

Figure 13: image shift correction dialogue in HybridRecon

After selecting Y-90 as administered isotope the screen shown in figure 13 allows correcting for any shift during the imaging and defines the camera parameters.

Next all parameters necessary for the iterative image reconstruction and the application of corrections need to be set up. The set of parameters used for all quantitative reconstructions is shown on the next page. The dataset is reconstructed with 4 iterations and 16 subsets, which is the default setting and close to the setting found to be best by Porter, et al., (2018). For the post-reconstruction filtering the default setting to a Gaussian with 1 cm FWHM is equally left unchanged. Some other filter settings have been investigated in the course of this study, but no definite improvement was found and the use of the default is probably the least arbitrary.

The parameters for the CT and attenuation correction as well as the collimator dimensions are derived from the header files of the SPECT measurements and the details of the mid-energy (ME) collimator provided by Siemens. The parameters for computing the scatter correction are also set to the default values.

In order to do quantitative reconstruction a conversion factor between measured counts and activity concentration needs to be determined and inserted in the 'SUV' submenu. This has been done as part of the phantom measurements and is described in more detail in section 3.1. A more detailed description of all possible parameter settings on the next page can be found in the HybridRecon documentation (Hermes Medical Solutions, 2017).

In the next step the positional agreement of the SPECT and the CT image can be reviewed and a translation correction can be performed. Although a few reconstructions with manual translation corrections have been made during the early phase of this study no correction was performed for the quantitative reconstructions, which are further evaluated. On the one hand it is quite unlikely that the patient has moved in the short time between the SPECT and the CT scan thereby causing a translation, on the other hand the influence of manual shifts on the quantitative results is hard to estimate and quite arbitrary. However the agreement between SPECT and CT images after the reconstruction process seems to be generally very good.

After the translation correction the actual image reconstruction is performed taking about 2-3 minutes.

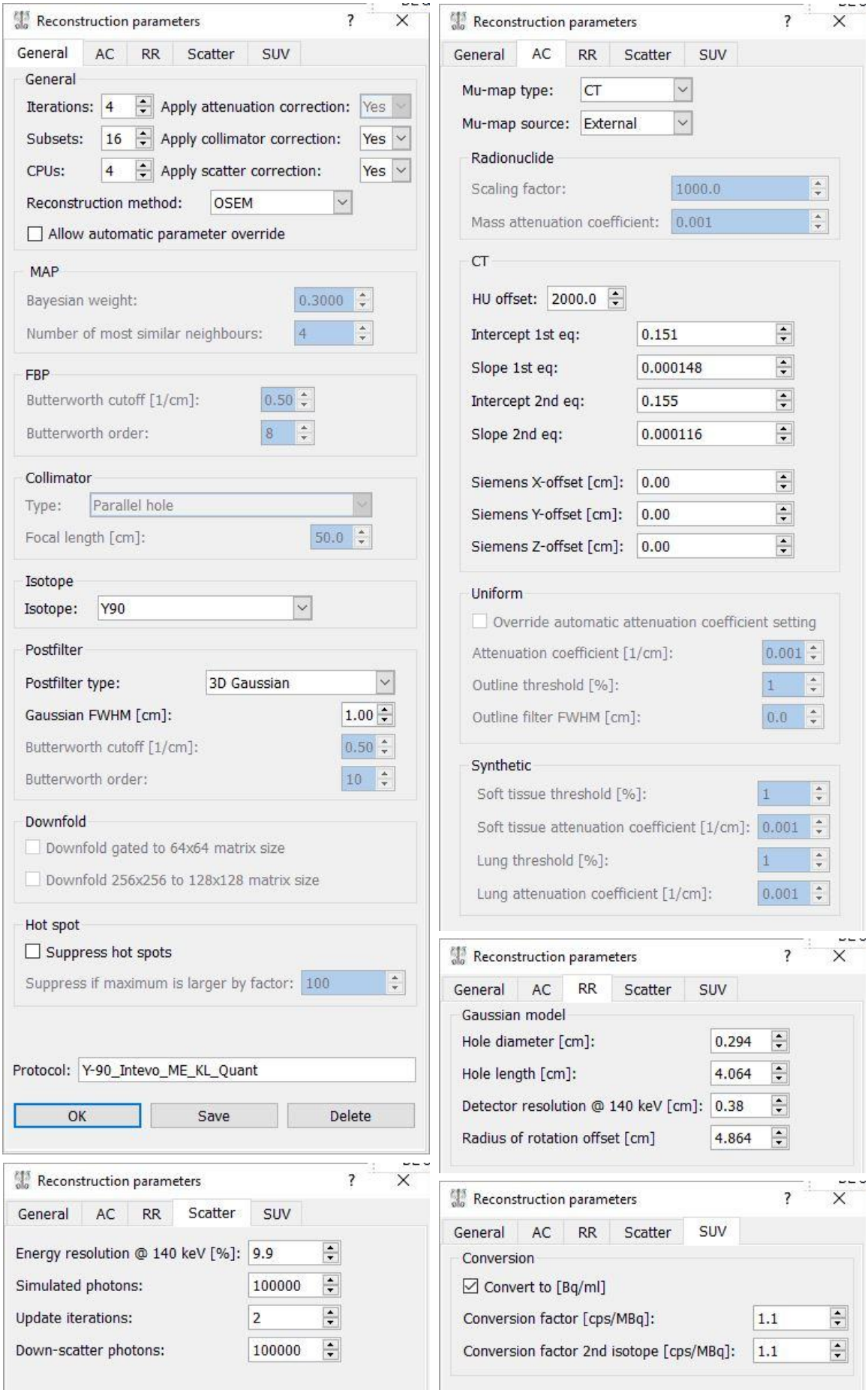

Figure 14: parameters used for all quantitative reconstructions with HybridRecon in this project

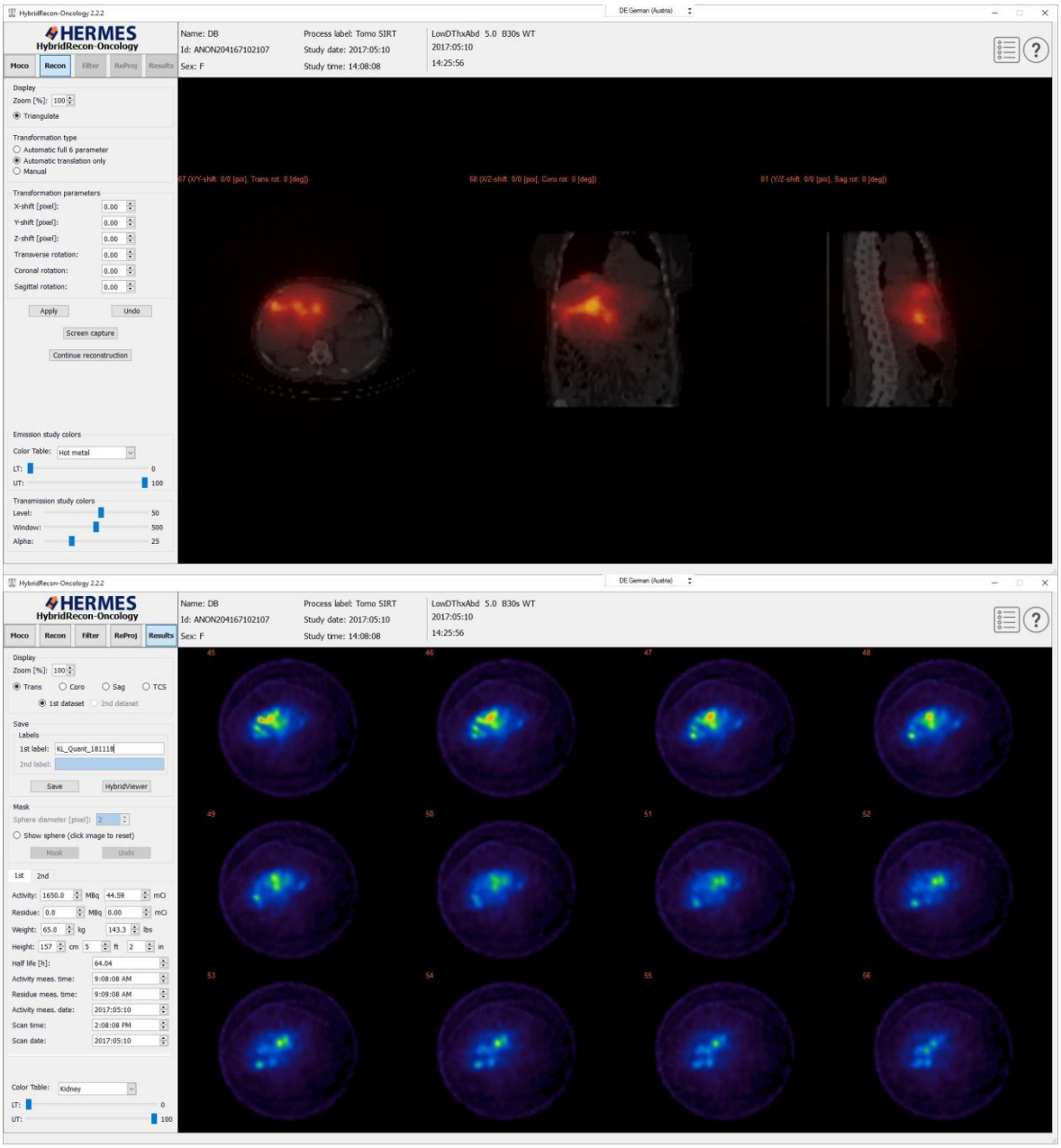

Figure 15: Top: the dialogue for applying a translation correction, allowing for a shift between SPECT and CT image, Bottom: the dialogue for inserting details for the quantification of the reconstruction.

After that the details necessary for quantification need to be set. These are the patient's height and weight, the measured activity and the residue after administration as well as the respective times for measurements and the scan. As not all these details were available the administered activity was always correctly set and the residue always kept at 0. Additionally no precise documentation of activity measurement times is available, but an average time span of 3-5 hours between activity measurement and SPECT scan was estimated by the performing technician. Therefore the time of the activity measurement is always set to date exactly five hours before the time of the scan, which is precisely known out of the header file.

Due to the relatively long half live of Y-90 an uncertainty of 2 hours does not have a very large impact. For the above given example and an administered activity of 1.65 GBq the largest possible error made, would be about 0.04 GBq.

After this last step the reconstructed image can be viewed and evaluated in Hybrid Viewer.

2.5 Clinical Practice

In this project a dataset consisting of 17 patients is evaluated. All were treated at Allgemeines Krankenhaus der Stadt Wien (AKH Vienna) between May 2017 and May 2018 and the data was provided by Dr. Alexander Haug of the clinical department of nuclear medicine. It would have been desirable to have a larger dataset to work on, however this was not possible as the SPECT imaging facilities were changed in early 2017. Therefore it would not have been possible to precisely quantify earlier data and additionally no CT-based attenuation correction would have been available.

Figure 16: the Siemens Symbia Intevo SPECT/CT in the department of nuclear medicine of AKH Vienna

All patients in the dataset were treated with SIR-Spheres manufactured by SIRTEX Medical Europe GmbH (Bonn, Germany). These are biocompatible microspheres coated with a polystyrene resin and between 20 and 60 microns in diameter. The yttrium is incorporated into the resin matrix by ion exchange and immobilized afterwards. The spheres are provided in water in vials calibrated to contain 3 GBq of activity and containing about 40 million spheres each. This yields a specific activity of about 75 Bq per sphere. (Westcott, et al., 2016), (Sirtex Medical Limited, 2016)

Before the treatment imaging was performed and the activity to administer was then calculated according to the results. SIRTEX provides two formulae for calculating activity and dose prior to the treatment and of those the BSA method (=body-surface-area) was chosen. (Sirtex Medical Limited, 2016)

$$A(GBq) = BSA - 0.2 + \frac{\%\ tumour\ involvement}{100}$$

$$BSA(m^2) = 0{,}20247 \cdot height(m)^{0{,}725} \cdot weight(kg)^{0{,}425}$$

$$\%\ tumour\ involvement = \frac{V_{Tumour}\ \cdot 100}{V_{Liver}}$$

However it should be noted that the quantity of tumour involvement was not calculated as given above, but estimated by the treating physician. The other model yields more precise results, when a clearly defined large tumour exists and will be discussed in the section on dosimetry.

With the described technique activities between 0.56 and 2.77 GBq were determined and administered. However the mean activity of 1.71 +/- 0.487 GBq is probably more representative as the lowest value of 0.56 GBq represents the second treatment for this specific patient. All patients listed in table 1 were adults with 12 men and 5 women in the dataset.

Name	Gender	Weight (kg)	Height (cm)	applied A (GBq)	V Liver (mL)
BM	F	115	169	1.790	1989
DB	F	65	157	1.650	1846
EE	M	86	174	1.120	1670
ER	M	64	184	1.840	not given
KK	M	74	174	1.740	2510
MH	F	56	169	1.340	1240
MK	M	85	174	1.770	1083
OH	M	70	180	1.830	1395
RL	M	63	165	1.290	1937
SE	F	63	160	1.620	1734
SF	M	75	170	1.940	2175
SJo	M	70	174	1.690	1028
SJu	F	45	168	2.770	2310
SM	M	95	174	1.706	1753
WC	M	75	165	0.580	3009
WH	M	93	172	2.150	1476
ZP	M	71	172	2.370	2413

Table 1: overview of the relevant patient data of this project. The patients' names were anonymised as displayed, M indicates a men, F a woman

The activity is prepared according to the specifications provided by the manufacturer and a VEENSTRA Instruments Dose Calibrator VDC-404 is used for calibration. Three to five hours after the microspheres are injected via a transarterial infusion into the hepatic artery, the SPECT/CT imaging is performed. All images were acquired on a Siemens Symbia Intevo SPECT/CT, which features a double headed gamma camera.

For normal patient studies an acquisition time of roughly 15 minutes is used (25 s per frame) and 32 frames are measured by each camera in a 180 degree arc, resulting in an angular step size of 5.625°. The energy window is set as 105 – 195 keV and thus a bit higher than in similar studies.

2.5.1 Phantom Measurements

For calibration and evaluation purposes phantom measurements were performed at AKH Vienna in May 2018 at the beginning of this thesis. A Jaszczak phantom and a NEMA IEC Body Phantom (EN 61675-1, 2014) were measured with the same settings as for clinical acquisition and also with longer timeframes.

In preparation for the measurement all inlays were removed from the Jaszczak phantom, because a homogeneous distribution of activity in a large volume was desired for the calibration measurements, according to the instructions by Hermes. Then the empty phantom was filled with warm tap water taking care not to leave any air bubbles.

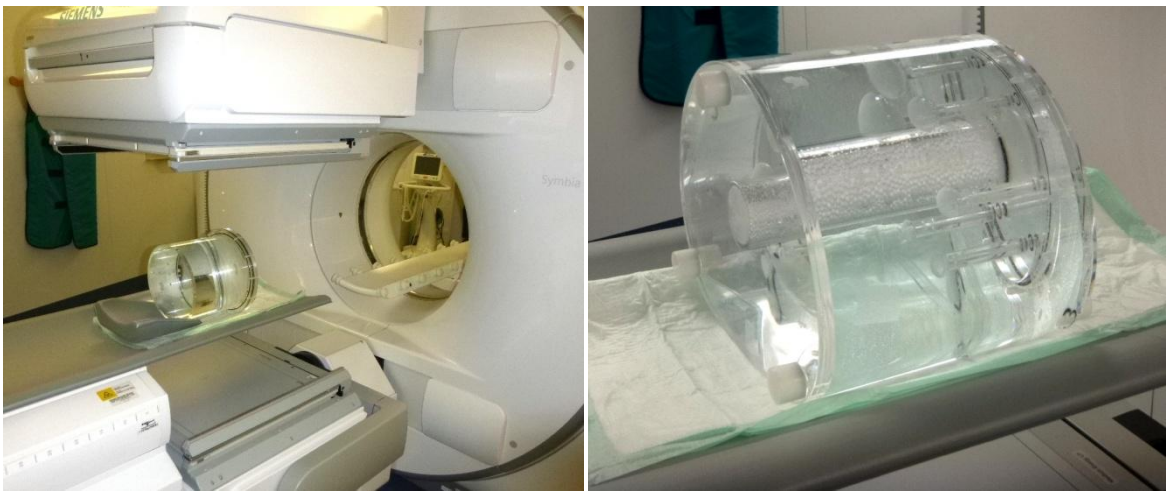

Figure 17: Left: the Jaszczak phantom in the SPECT/CT measurement set-up, Right: the NEMA IEC Body phantom, the spherical inlays are easily visible

In order to perform phantom measurements it is not possible to use Y-90 microspheres as a homogeneous distribution in water could not be achieved. Therefore the Y-90 intended for phantom measurements was provided in water soluble form as yttrium chloride. The activity was calibrated at an ISOMED 2010 and 0.564 GBq were injected into the water via a syringe and then distributed. Next two measurements on the standard SPECT/CT set-up

for Y-90 imaging were performed: one measurement with the default acquisition time of 25 s per frame one with 50 s per frame.

The NEMA IEC Body phantom was prepared in a similar way. The activity was dissolved in 50 ml of water and activity and residue in the syringe were measured. The six spherical inlays were filled with the Y-90 solution and care was taken to avoid the formation of water bubbles. The bulk of the phantom around the inlays was again filled with warm tap water. Detailed activities can be found in table 2 below and were calculated from the specifications given in the phantoms' data sheets.

For the body phantom three measurements were performed in the clinical set-up: acquisition times were 15 min (25 s/frame), 30 min (50s/frame) and a long-term measurement of 8 h (900 s/frame).

	Activity (MBq)	**V_{total} (mL)**	**V_{activ} (mL)**	**A Conc (MBq/mL)**
Jaszczak Phantom	564.62	6815.70	6815.70	0.0828
Body Phantom	465.06	9700.00	47.84	9.7216
Inlay d=37 mm	257.84		26.52	9.7216
Inlay d=28 mm	111.74		11.49	9.7216
Inlay d=22 mm	54.20		5.58	9.7216
Inlay d=17 mm	25.01		2.57	9.7216
Inlay d=13 mm	11.18		1.15	9.7216
Inlay d=10 mm	5.09		0.52	9.7216

Table 2: overview of the phantom measurements performed at AKH Vienna. If not measured the quantities were calculated using specifications from the data sheet.

3 Results and Discussion

3.1 Correction Factors

3.1.1 Conversion Factor

In order to be able to perform any quantitative measurements a conversion factor from counts per second (cps) to activity (Bq) needs to be defined. To achieve this, a measurement of the Jaszczak phantom was performed in the clinical set-up according to the procedure given by Hermes as described in section 2.5.1.

The reconstruction was done with a special instance of HybridRecon that performs a normal reconstruction process, but yields a conversion factor based upon the precisely known data of the phantom measurements.

$$\frac{C\ (cps)}{\tilde{Q}} = A\ (MBq)\ \rightarrow\ \tilde{Q} = \ 1.1 \pm 0.0\ cps/MBq$$

This factor was found to be 1.1 without any uncertainty in the given digits. ROIs[5] encompassing different amounts of the phantom can be defined and the evaluation was done with ROIs of 50 %, 70 % and 90 % the size of the Jaszczak phantom. It does not seem reasonable to define a smaller ROI as this only increases the chance of faulty results due to larger influence on inhomogeneities. Additionally the same evaluation was performed on the measurement with 30 min acquisition time, also yielding a factor 1.1 with ROIs defined as above. This indicates that no further uncertainty is introduced by the calibration and will be considered in the uncertainty budget (section 3.2).

3.1.2 Partial Volume Effect

The measurements of the NEMA IEC Body phantom can be used to estimate the so called partial volume effect. This effect can lead to a severe underestimation of an activity in a given volume and is the more pronounced the smaller the volume is.

The reason for the effect is illustrated in figure 18. When an object is smaller than the spatial resolution of the detector or undershoots the resolution in time a spill-out of counts occurs. Therefore the activity that is really constrained in a smaller volume is blurred over a large part of the image. This can significantly affect measured activities and activity concentrations.

[5]A ROI (=region of interest) or VOI (=volume of interest) can be defined in HybridViewer and is a fundamental instrument of all evaluations in this study. Only the area/volume inside it will be considered as "interesting" and will therefore be evaluated (e.g. for its total activity). Classically a VOI is used to outline an organ or a lesion and very often defined arbitrarily. In section 3.4.1 the definition of the VOIs used for a part of this project will be discussed in detail.

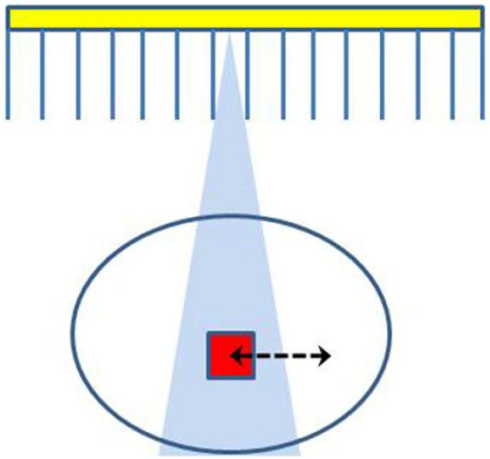

Figure 18: schematic illustration of the partial volume effect, the arrow indicates possible movement of the object. (Erlandsson, et al., 2012)

Sophisticated correction techniques have been developed, but will not be applied in this project. The main reason for this is that the size of the lesions or of centres of activity concentration is not exactly known and the correction is heavily depended on this measure. However a recovery factor $R = \frac{C}{C_{total}}$ can be determined for the inlays in the body phantom. (Erlandsson, et al., 2012)

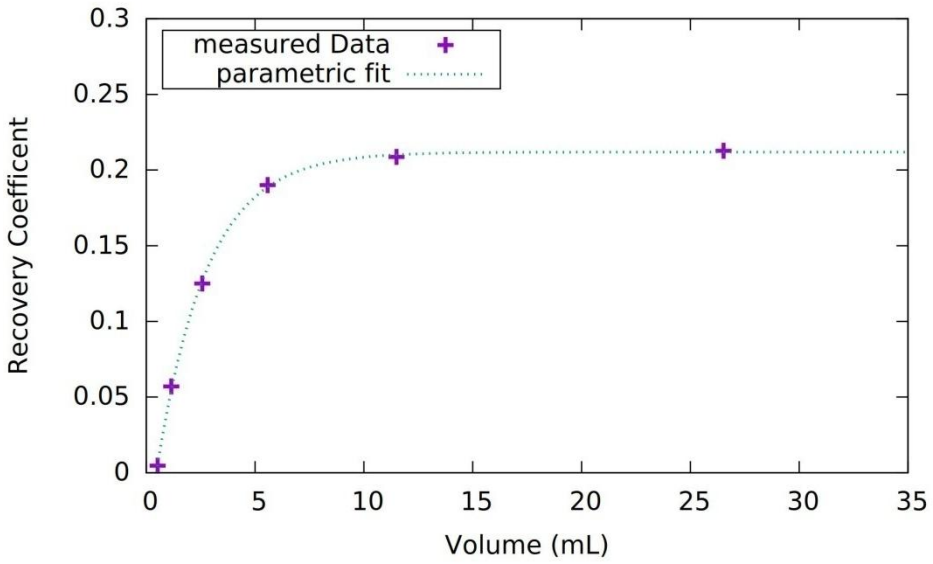

Figure 19: parameterized fit of the recovery coefficient for the body phantom

In order to achieve this VOIs representing the real inlays were placed on the CT image and then evaluated. Thus the recovery factor depicted in figure 19 is computed. A nonlinear least-squares Marquardt-Levenberg algorithm was used to fit a parameterized solution and $f(x) = a \cdot e^{bV} + c$ was found to be the best guess. The uncertainties computed with the fit will be used in the next section.

3.2 Uncertainty Budget

Before the patient dataset is evaluated in detail an estimation of the uncertainty budget will be made. The calculations for an uncertainty budget of the body phantom will closely follow the EANM (European Association of Nuclear Medicine) guidelines (Gear, et al., 2018) and a modification for the evaluation of the patient data will be attempted.

According to Gear, et al. several sources of uncertainty have to be considered for the results of quantitative reconstruction: volume and voxelisation effects, the calibration factor, uncertainties in activity measurements and finally the recovery coefficient.

The uncertainty of a single value x_i in a dataset with n entries can be calculated with the well known formula

$$\sigma_i = \sqrt{\frac{(\bar{x} - x_i)^2}{n-1}}$$

While the standard deviation of the mean value s_{mean} is determined as follows, taking also the Student's t-distribution into account.

$$s_{mean} = t_P(n) \cdot \sqrt{\frac{1}{n}\sum_{i=1}^{n} \sigma_i^2}$$

t_p depends on the number of samples n and is tabulated, see for example Lichten, (1999).

In case a value $y = f(x_1, x_2, \dots x_n)$ is calculated from several variables, which all have uncertainties the Gaussian law of error propagation must be applied:

$$\sigma_y = \sqrt{\sigma_{x_1}^2 \left(\frac{\partial f}{\partial x_1}\right)^2 + \sigma_{x_2}^2 \left(\frac{\partial f}{\partial x_2}\right)^2 + \cdots + \sigma_{x_n}^2 \left(\frac{\partial f}{\partial x_n}\right)^2}$$

For determining the activity in a volume of interest the count rate must be multiplied with a conversion factor Q, as given above. Note that for this approach $C \cdot Q = A$ was chosen and therefore $Q = \frac{1}{\bar{Q}} = 0{,}909 \ \pm 0{,}0$.

Additionally a recovery coefficient can be applied.

$$A_{VOI} = C \cdot Q \cdot R$$

C	count rate (cps)
Q	conversion factor (MBq/ cps)
R	recovery coefficient

$$\sigma(A_{VOI}) = A_{VOI}\sqrt{\frac{1}{C^2}\sigma^2(C) + \frac{1}{Q^2}\sigma^2(Q) + \frac{1}{R^2}\sigma^2(R)}$$

Now the uncertainties of all variables will be determined and allowed for. The uncertainty of the count rate can also be computed, but in this project it will be determined empirically according to a technique that has also been suggested by the author of the EANM guidelines. (Gear, 2018)

A non-quantitative reconstruction of the Jaszczak phantom was performed with normal parameters. 29 ROIs with a fixed diameter of 5.0 cm were placed in all layers of the phantom image (all values can be found in appendix A.1) and the count rate and mean number of counts per unit area were evaluated for all ROIs. A relative uncertainty[6] of 7.8 % of the mean value was found and will be included in the uncertainty budget.

In this phantom measurement a relatively large amount of activity is distributed homogeneously in a volume much bigger than what is typically encountered in the clinical environment. Therefore this measurement will be considered as an ideal situation and the computed uncertainty will be used as an estimate of the minimum uncertainty of every measured count rate. Due to the fact that the uncertainty was estimated using ROIs possible voxelisation effects are also already included in the uncertainty value. Therefore $\sigma_C = \sigma_C(V)$ and the covariance of σ_C and $\sigma_R(C, V)$ must also be taken into account.

The uncertainty of Q is introduced during the calibration process and can be expressed as follows

$$\left(\frac{\sigma(Q)}{Q}\right)^2 = \left(\frac{\sigma_{A_{cal}}}{A_{cal}}\right)^2 + \left(\frac{\sigma_{C_{ref}}}{C_{ref}}\right)^2$$

$\sigma_{A_{cal}}$ is the uncertainty of the activimeter used for calibrating the activity applied to the Jaszczak phantom. The device used was an ISOMED 2010 and the uncertainty was estimated to be about 20 % by the retailer. The medical physicist supporting the phantom measurements estimated an even higher uncertainty as Y-90 is a pure beta emitter and has some degree of self absorption. Additionally the activity was measured in a non standard geometry further inhibiting a precise measurement. The uncertainty estimated by the retailer will be included in the uncertainty budget.

The second term describes the uncertainty for measuring the count rate in the Jaszczak phantom and defining a linear calibration factor. To get an even more precise estimate of that value than discussed above a non-quantitative reconstruction was performed. The

[6] As the uncertainty of individual measurements and not the uncertainty of the mean value is relevant here σ_i will be calculated as given in the beginning of this section

count rate of several VOIs of different sizes was plotted and a linear fit was performed yielding a calibration factor and its uncertainty.

$$C(cps) = A(MBq) \cdot Q \quad \rightarrow \quad Q = 1.108 \pm 0.0036 \ (\pm 0.32\ \%)$$

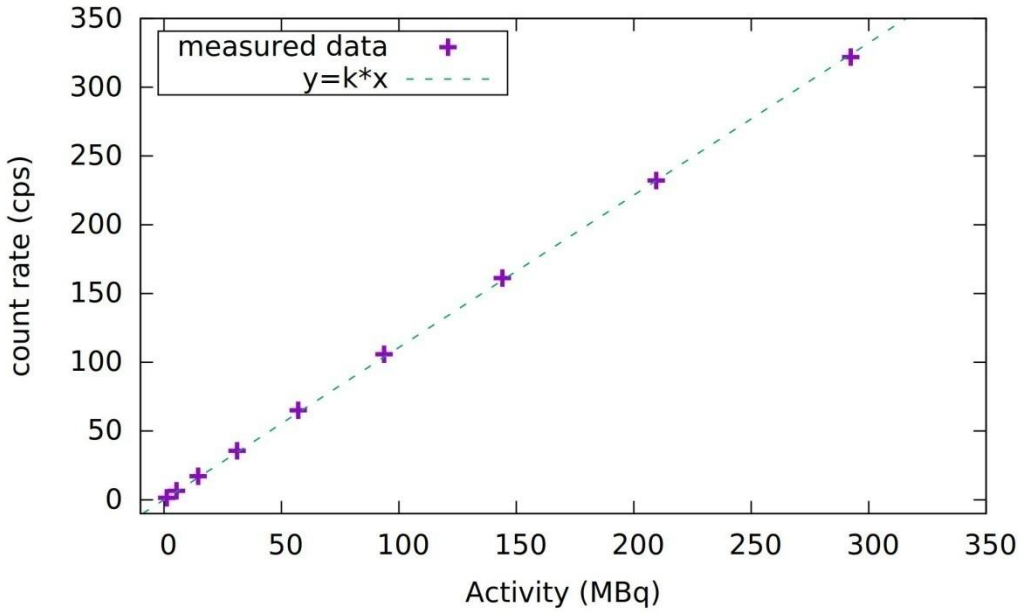

Figure 20: linear fit of a conversion factor from cps to MBq

As described in the last section a parametric fit was made to find a mathematical expression for the recovery coefficient. The values and absolute uncertainties of the fit parameters can be found in table 3 and are used together with the covariance matrix $\mathbf{V_b}$ yielded by the fit to determine σ_R.

$$\sigma^2(R) = \boldsymbol{g}_b^T \boldsymbol{V_b} \boldsymbol{g}_b \qquad \text{with } g_b = \begin{pmatrix} \frac{\partial f}{\partial a} \\ \frac{\partial f}{\partial b} \\ \frac{\partial f}{\partial c} \end{pmatrix} \text{ and } V_b = \begin{pmatrix} \sigma_a^2 & \sigma_{ba} & \sigma_{ca} \\ \sigma_{ab} & \sigma_b^2 & \sigma_{cb} \\ \sigma_{ac} & \sigma_{bc} & \sigma_c^2 \end{pmatrix}$$

Also taking into account that the recovery coefficient depends on the volume $\mathbf{V_b}$ must be modified

$$\boldsymbol{V_{b,V}} = \begin{pmatrix} \boldsymbol{V_b} & 0 \\ 0 & \sigma^2(V) \end{pmatrix} \qquad \text{in order to align the dimensions } g_b \text{ is modified as } g_b = \begin{pmatrix} \frac{\partial f}{\partial a} \\ \frac{\partial f}{\partial b} \\ \frac{\partial f}{\partial c} \\ \frac{\partial f}{\partial V} \end{pmatrix}$$

Inlay d (cm)	applied A (MBq)	measured A (MBq)	calc. Recovery Factor	absolute Uncertainty	relative Uncertainty (%)
3.70	257.84	50.88	0.207	0.013	6.216
2.80	111.74	22.99	0.199	0.010	4.907
2.20	54.20	9.47	0.161	0.012	7.265
1.70	25.01	2.12	0.094	0.016	17.041
1.30	11.18	0.22	0.034	0.025	74.649
1.00	5.09	0.06	-0.002	0.039	1791955

Table 3: recovery factors for the inlays calculated using the parametric fit and their uncertainties computed as given above, the smallest inlay does not yield meaningful results

The uncertainty of the volume mainly depends on the voxel width a and can be approximated as

$$\frac{\sigma(V)}{V} = \frac{3\sigma_{Vox}}{d} \quad \sigma_{Vox} = \sqrt{\frac{a^2}{6}}$$

As mentioned the correlation between C and R needs to be considered and for this the theoretical expression for $\sigma(C)$ is necessary.

$$\frac{\sigma(C)}{C} = \frac{\varphi}{2R}\frac{\sigma(V)}{V} \text{ and } \varphi = \operatorname{erf}\left(\frac{2r}{\sigma\sqrt{2}}\right) - \frac{2\sigma}{r\sqrt{2\pi}}\left(1 - e^{-\frac{2r^2}{\sigma^2}}\right)$$

r is the radius of a spherical VOI and $\sigma = \left(\frac{FWHM}{2\sqrt{\ln(2)}}\right)^2$ is an uncertainty value associated with the spatial resolution. Gear, et al. calculate the covariance term as follows

$$\sigma(R,C) = \frac{\varphi C}{2RV}\frac{\partial R}{\partial V}\sigma^2(V) \quad with \quad \sigma(V) = \frac{a^2}{6}$$

Using the empirically determined uncertainty for C this can be modified for this project as

$$\sigma(R,C) = \frac{\sigma(C)}{C} C \frac{\partial R}{\partial V}\sigma(V) = \sigma(C)\sigma(V)\frac{\partial R}{\partial V}$$

Summing up the uncertainty for the activity measured in a small VOI with a known recovery coefficient (for example in a body phantom) can be given as

$$\boxed{\sigma(A) = A\sqrt{\frac{1}{C^2}\sigma^2(C) + \frac{1}{Q^2}\sigma^2(Q) + \frac{1}{R^2}\sigma^2(R) + \sigma(C)\sigma(V)\frac{\partial R}{\partial V}}}$$

In the next section the total activity measured in the patient datasets will be evaluated. For this case no recovery coefficient is applied and therefore the above given formula needs to be newly adapted. Additionally after several other attempts described in section 3.4.1 a best threshold value for drawing a VOI that includes the total activity applied to the liver was found. That value is computed as the mean of the individual best threshold values and the thereby introduced uncertainty needs to be included.

$$A_{Tot} = C(V_{Threshold}) \cdot Q \quad and \;\; C(V_{Threshold}) = \frac{C}{n \cdot a^3} V_{Threshold}$$

a voxel width

n number of voxels

$$\sigma\big(C(V)\big) = C(V) \sqrt{\frac{1}{C^2}\sigma^2(C) + \frac{1}{V_{Thres.}^2}\sigma^2(V_{Thres.})}$$

$$\rightarrow \; \sigma(A_{Tot}) = A_{Tot} \sqrt{\frac{1}{C(V)^2}\sigma^2(C(V)) + \frac{1}{Q^2}\sigma^2(Q)}$$

Finally some considerations for the uncertainty in dosimetric calculations need to be made. As discussed in section 3.8.4 a post-treatment dose evaluation can be performed by multiplying the activity concentration with a constant factor:

$$D = \frac{\langle E \rangle A_0}{m} \int_0^\infty e^{-\ln(2)\mathrm{t}/\mathrm{t}_{1/2}}\, dt = \frac{\langle E \rangle A_0 t_{1/2}}{m\, ln(2)} =$$

$$= \frac{\langle E \rangle t_{1/2}}{\ln(2)\, \rho} A_{Conc} = A_{Conc} \cdot const$$

This approach implies the assumption that the range of the emitted particles can be neglected. As the mean range[7] of Y-90 beta particles with a mean energy of 0.93 MeV is 4.0 mm and the voxel size is 4.8 mm this assumption seems valid. However to estimate the uncertainty introduced with this approach the fraction of electrons with a range more than twice the mean range will be determined in this thesis. The mean range was obtained from NIST (National Institute of Standards) (Berger, et al., 2017) and the Y-90 beta spectrum from the Radar Group (Stabin, et al., 2003). The necessary values, which are not tabulated, were obtained by linear interpolation between the next neighbours. Summing up the data presented in table 4 a fraction of 9.6 % of all electrons emitted by

[7] In this context the CSDA range is used. *"CSDA range: a very close approximation to the average path length traveled by a charged particle as it slows down to rest, calculated in the continuous-slowing-down approximation. In this approximation, the rate of energy loss at every point along the track is assumed to be equal to the total stopping power. Energy-loss fluctuations are neglected. The CSDA range is obtained by integrating the reciprocal of the total stopping power with respect to energy."* (Berger, et al., 2017)

beta decay of Y-90 has a range larger than 8.1 mm and will likely not be detected in the same voxel as they were emitted in.

Energy (keV)	total stopping power (MeV cm^2/g)	CSDA range (cm)
800.00	1.8860	0.3314
900.00	1.8650	0.3847
933.60		0.4028
1000.00	1.8510	0.4385
1500.00	1.8290	0.7110
1673.05		0.8056
1750.00	1.8310	0.8476

Energy range (keV)			fraction
1598.80	-	1713.00	0.0430
1673.05	-	1713.00	0.0151
1713.00	-	1827.20	0.0342
1827.20	-	1941.40	0.0246
1941.40	-	2055.60	0.0150
2055.60	-	2169.80	0.0064
2169.80	-	inf	0.0011
Fraction of electrons with E > 1.67 MeV			**0.0964**

Table 4: tabulated range of beta particles in tissue and energy distribution of Y-90

Therefore a conservative assumption for the uncertainty introduced by the constant dose conversion factor will be made. Assuming all electrons with a range larger than 8.1 mm will be detected in a wrong position the fraction of electrons with these energies can be added as an additional uncertainty.

$$\sigma(D) = D\sqrt{\frac{1}{A_{Conc}^2}\sigma^2(A_{Conc}) + \frac{1}{const^2}\sigma^2(const)}$$

$$A_{Conc} = \frac{C}{V}\cdot Q \cdot R = C_{Spec}\cdot Q \cdot R$$

$$\sigma(A_{Conc}) = A_{Conc}\sqrt{\frac{1}{C_{Spec}^2}\sigma^2\left(C_{Spec}\right) + \frac{1}{Q^2}\sigma^2(Q) + \frac{1}{R^2}\sigma^2(R)}$$

As this approach requires an activity concentration not an activity value the uncertainty of the count rate per unit area that has been estimated from the images of the Jaszczak phantom will be used. All values can be found in appendix A.1 and a relative uncertainty of 8.2 % will be included in the uncertainty budget. As this approach is independent of the

volume, the covariance between R and C can be neglected. For the dose calculations data with and without recovery coefficients will be used and the appropriate formulas to calculate the uncertainty will be selected.

In order to facilitate the calculation of uncertainties for the whole dataset a simple MATLAB script (The MathWorks, Inc., 2017) has been written during this thesis and was used for the calculation of all uncertainties given in the following sections. The code can be found in appendix B.1 .

In table 5 the uncertainty budgets for the cases given above are summarized. If a constant value is applied for all cases it is given as relative uncertainty, if the uncertainty depends on the measured data an example will be given.

	Activity Body Phantom Body	**Total A Patients**	**Activity Concentration**	**Dose from A Conc**
$\sigma(A_{Calc})/A_{Calc}$	20.00 %	20.00 %	20.00 %	20.00 %
$\sigma(C_{ref})/C_{ref}$	0.32 %	0.32 %	0.32 %	0.32 %
$\sigma(Q)/Q$	20.03 %	20.03 %	20.03 %	20.03 %
$\sigma(C)/C$	7.60 %	7.60 %	8.20 %	8.20 %
$\sigma(Voxel)/V$	(1.94 %)	(1.94 %)	/	/
$\sigma(R)/R$	(6.20 %)	/	/	(6.20 %)
$\sigma(V_{Thres})/V$	/	12.30 %	/	/
$\sigma(const.)/const.$	/	/	/	9.60 %
total uncertainty	(24.09 %)	(27.45 %)	23.48 %	(24.38 %)

Table 5: uncertainty budget for the different cases discussed above, if the value is dependent on the sample it is set in parenthesis

3.3 Phantom Measurements

Before analyzing the patient dataset the phantom measurements from May 2018 were evaluated.

In the figure below the activities measured in the respective inlays of the body phantom are plotted together with their uncertainties (detailed values are listed in appendix A.2). To acquire the data spherical VOIs with the diameter of the real inlays were placed in the SPECT image and evaluated. Then a recovery factor was calculated and applied as described above.

The calculated uncertainty of 24 % for the largest inlay seems quite reasonable, when one considers the additional difficulties, due to the continuous bremsstrahlung spectrum. It is equally comprehensible that the uncertainty grows with decreasing volume as the relatively low image quality gets more accentuated.

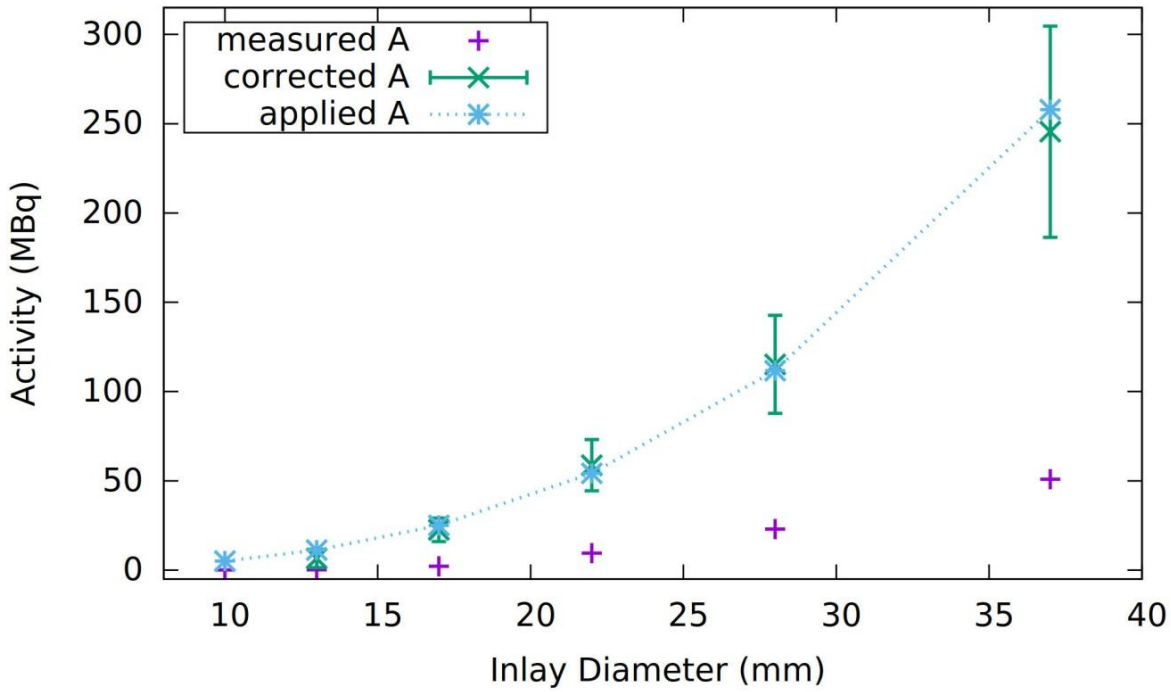

Figure 21: activity measured in the different inlays of the body phantom. The relative uncertainty of the corrected activities (blue) increases with decreasing inlay size.

For further quality control the data from the Jaszczak phantom was used for determining total activity and SUV value. SUV is the abbreviation for standardized uptake value, is given as the ratio between applied activity concentration and measured activity concentration $SUV = \frac{c(A_{applied})}{c(A_{measured})}$ and is frequently used in nuclear medicine to measure the uptake of a radionuclide (Kinahan, et al., 2010). If the assumption is valid that with application of all corrections the true activity concentration is measured a SUV value of 1.0 should be found. Taking the values from a VOI drawn over a large part of the Jaszczak phantom, a mean SUV value of 1.03 could be determined. This points to a good quality of the reconstruction and the applied corrections.

For further evaluation VOIs of different sizes were constructed and the measured activities were plotted together with their uncertainties. As visible in figure 22 the total activity is slightly underestimated in comparison to the real value of applied activity. This is obviously consistent with a too low concentration value and indicates that even for very large sources a small spill-out effect can occur. Performing a linear interpolation between the measured points one sees that the activity is underestimated by 5.1 % for a VOI with the real phantom volume, if the VOI is enlarged until the correct activity is measured the volume is overestimated by 2.1 %. Overall these are very precise results with the applied activity well within the range of uncertainty of the measured values. It can be concluded that measurements of large homogeneous activity distributions can be performed with high precision and that no significant bias is introduced during the reconstruction.

The large uncertainty is mainly caused by factors not directly connected with the phantom measurement like the initial calibration of activity.

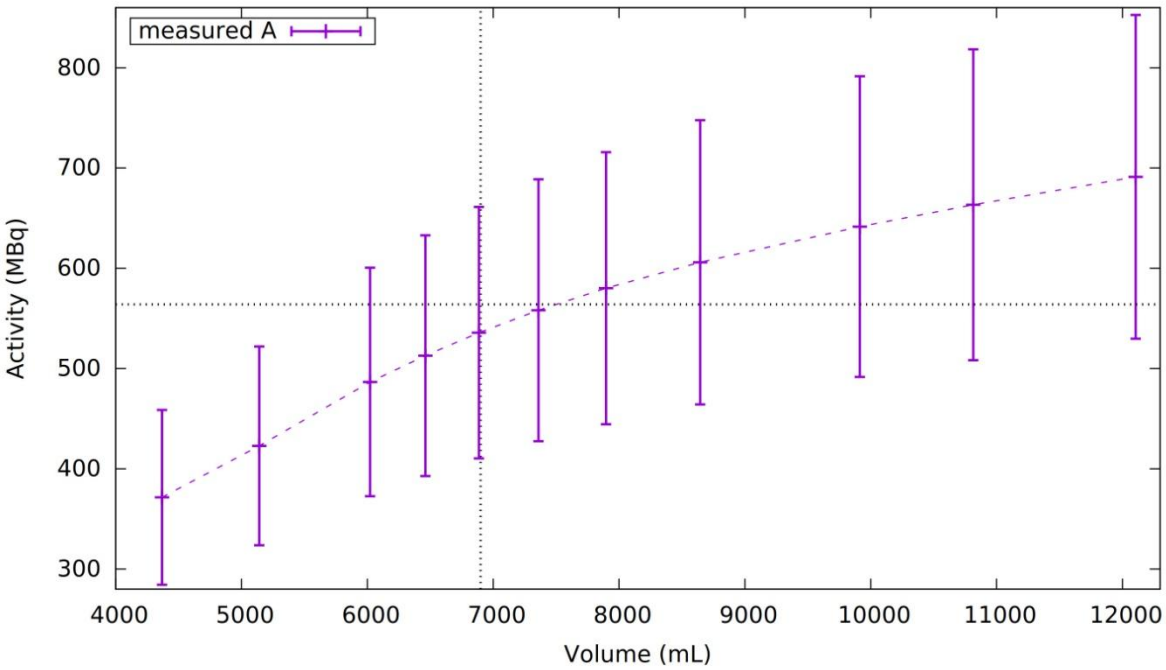

Figure 22: activities measured in VOIs of different sizes in the Jaszczak phantom

3.4 Evaluation of Patient Data

Before performing any dose calculations it was an objective of this thesis to evaluate the credibility of the reconstructions of the patient images. To do this the total activity will be determined. Unlike other treatments in MRT the applied activity does not change over time due to metabolism as the Y-90 bearing microspheres get trapped in the microvasculature. This also means that all the applied activity should be measured in the liver region. The only relevant exception is the lung, as a small part of microspheres might be transported with the blood flow from the liver into the lung, the so called lung shunting fraction.

However this phenomenon is considered during the treatment planning and the lung shunting fraction can for example be estimated with a Tc-99m-MAA SPECT scan. If it is likely that a dose higher than 20 Gy will be applied to the lung some blood vessels can be cauterized to minimize unwanted exposure or the total dose can be reduced. (see section 2.2)

For this project unfortunately no precise data of the lung shunting is available. Therefore it will be assumed that a maximum of 10 % of the applied activity has been displaced to the lung and all the rest should be measured in the liver region.

3.4.1 Threshold Selection

In order to be as consistent as possible the criterion for the threshold value of the VOI has to be considered. Although it is not uncommon in nuclear medicine to simply expand the VOI until it covers all activity that is considered relevant this introduces a huge arbitrary element into any evaluation and will therefore be avoided during this project.

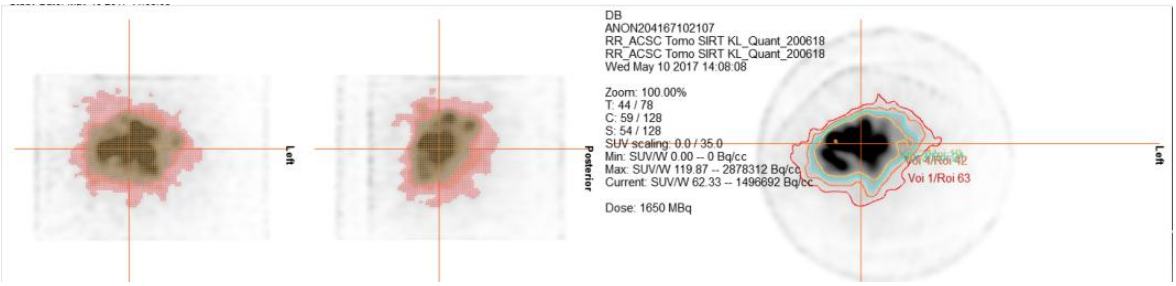

Figure 23: Evaluation of total activity for patient DB using VOIs of different sizes

Patient DB	Threshold SUV	A Conc (Bq/mL)	V (mL)	A tot (MBq)
VOI 1	3.16	266050.69	7335.08	1951.50
VOI 2	11.75	600625.69	1912.25	1148.55
VOI 3	8.39	491192.97	2741.41	1346.56
VOI 4	5.50	382051.22	4140.95	1582.05
applied		**V_{Liver} ca.**	2300.00	1650,00

Table 6: values measured with the VOIs depicted above

In figure 23 and table 6 the example of patient DB illustrates how large an influence the selection of the VOI has. As much as 70 % difference can be found in VOIs created with thresholds ranging from 2.5 % of the maximum (SUV = 3.16) to 10 % of the maximum (SUV = 11.75). This example clearly illustrates the need to find a way of choosing the thresholds of the VOIs in a reproducible and logical way in order to avoid introducing a large element of uncertainty, because of arbitrary VOI definitions.

Apart from simply drawing volumes of interest it is possible in Hybrid Viewer to define different criteria for the construction of a VOI. As visible in figure 24 a constant SUV or activity concentration value can be chosen as threshold and a volume of interest will be constructed out of a continuous region with values higher than the given threshold. Moreover it is possible to define the threshold as a fraction of the maximum value instead of a constant figure. Then a volume of interest will for example be constructed out of a continuous region of values higher than 20 % of the maximum SUV value.

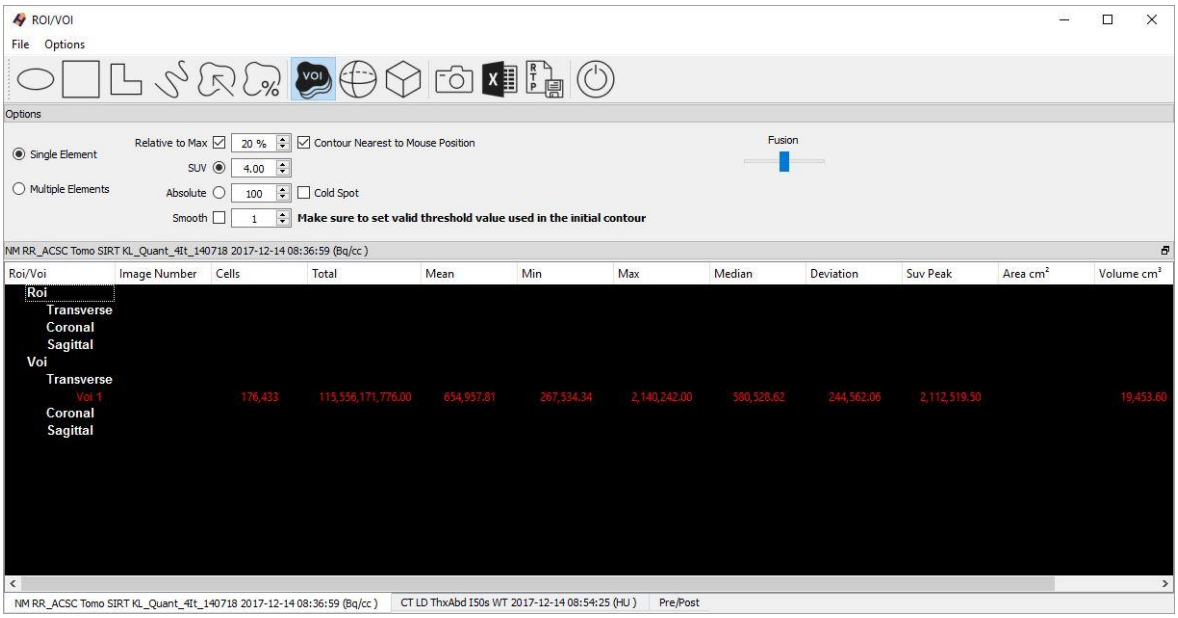

Figure 24: dialogue for choosing different ways of defining a VOI in Hybrid Viewer

Referring to the literature several approaches to the selection of threshold values can be found, see for example Porter, et al., (2018). Of these definitions the approach introduced by Shcherbinin, et al., (2008) was used during this thesis. He suggests a threshold value of 20 % of the maximum SUV value to get VOIs closely resembling the real active volume.

Additionally new threshold criteria were created for this thesis and their usefulness was investigated. The whole dataset was evaluated with VOIs with a constant threshold value of SUV=4.0 . This idea seemed reasonable, because for the patient DB in the example above and several similar cases the activity measured in a VOI with a threshold value of 4.0 is closest to the activity really applied.

Shcherbinin not only suggests a value of 20 % of the maximum SUV value for obtaining the most accurate results for the volume of a VOI, but also a threshold of 1 % of the maximum SUV for measuring the activity most precisely. However the latter did not work out for this project as for some patients large artefacts are visible, which completely distort the result if they are included in a VOI. In spite of the attenuation correction that is applied during the reconstruction process artefacts remain on the borders of the image and sometimes also outlining the patient's shape. These artefacts are variably pronounced in the data set and the activity in these voxels should probably not be included in the evaluation. Moreover the value of 1 % did not produce a separation between relevant activity and a possible background, basically including the whole image in one large VOI.

The idea of a background correction was investigated to compensate for this. 6 spherical VOIs with a diameter of 10 cm were placed in the edge layers of each image and the maximum and mean SUV values were obtained.

Next a mean was calculated for both sets of six values, yielding estimations of the mean and of the maximum background SUV values. Out of these values new thresholds were constructed

$$Threshold(SUV) = mean\ background(SUV) + max.\ SUV \cdot 0.01$$
$$Threshold(SUV) = max.background\ (SUV) + max.\ SUV \cdot 0.01$$

However this method is still not able to handle the image artefacts very well, because the VOI used for estimating the background sometimes include parts of these artefacts and thus yield higher background values. Furthermore the positioning of the background VOIs introduces again an arbitrary element into the VOI threshold definition.

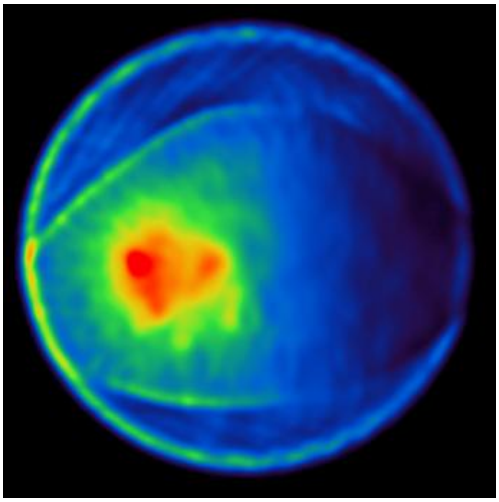

Figure 25: patient ER as an example for very pronounced image artefacts

Consequently the approach including a background correction was dropped and a mathematical relation between threshold and activity was investigated. For all patients VOIs were drawn using a wide range of different thresholds (usually the thresholds were ranging from 30 % of the maximum value to 4 % of the maximum value). Constraint ROIs were defined in order to exclude the aforementioned artefacts and only the area inside these ROIs was evaluated. The total activity inside the VOI was plotted against the threshold value and a parametric fit was performed.

The aim was to investigate, if there is a common threshold value that can always be used to define a VOI containing the applied activity. Additionally the relation between volume and activity of a VOI can be described mathematically. The parameterisation as $A = a + b \cdot A_{Threshold}^{c}$ seemed most promising. As before a nonlinear least-squares Marquardt-Levenberg algorithm was used for fitting and the detailed results can be found in appendix A.3. An example of the fit and the resulting thresholds can be viewed in figure 26. For fit parameter c a general behaviour following $A \propto \frac{1}{A_{Threshold}^{1/3}}$ can be assumed. This seems reasonable when the threshold value is compared to a radius. A change in the radius will lead to a threefold increase of a spherical volume. A similar

situation can be assumed here. The fit depicted below is very representative for the regular behaviour of the datapoints, which clearly follow an underlying trend.

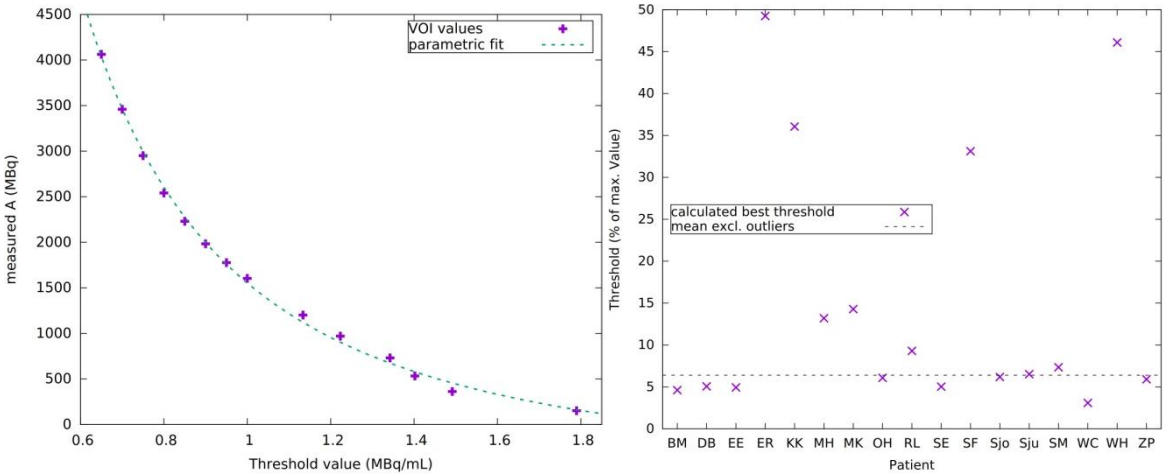

Figure 26 Left: patient SF example for the parametric fit describing a relation between threshold value and measured activity, Right: computed threshold values yielding the correct applied activity, the outliers are clearly visible

As visible in the plot above some data sets display a distinctly different behaviour, but for the others a common best threshold value could be found. The decision was made to exclude the patients ER, KK, SF and WH as outliers[8] and to use a mean best threshold value of 6.4 +/- 0.8 % of the maximum SUV values for the other datasets.

A reasonable explanation for the outliers was investigated, but the four patients do not seem to share distinct common characteristics. Liver volume, weight, height, body mass index and applied activity were compared, but for none of these measures a common trend shows. However it was found that the patients MH, WH, KK, SF and ER have been treated and imaged consecutively and with pauses of several weeks to other patients. Therefore some misalignment of the SPECT/CT or a faulty or different parameter setting during this period seems very reasonable. The data in the Dicom header that summarizes many image parameters has been examined to that aspect, but only small differences have been found. It is likely that those differences exist only due to varying inputs by different operators and they are probably not significant. All the same this assumption could explain, why the data from these four patients cannot be considered fully reliable and will therefore not be included in some of the evaluations.

3.5 Total Activity

The data displayed in the two figures below summarizes the total activity obtained from the evaluation made for this thesis using the aforementioned dataset of 17 patients. For each patient volumes of interest were defined according to the three criteria discussed in

[8] The patients MH and MK also show a slightly different behavior, but not as pronounced as the others. However this seems to be consistent with the explanation given.

the previous section. Additionally the applied activity is visible in the plot. In figure 27 the four outliers ER, KK SF and WH are clearly showing different behaviour with all three VOIs overestimating the applied activity by more than 4 GBq. Moreover the patients MH and MK show one severe overestimation each, which probably is not sufficient evidence two classify them as outliers.

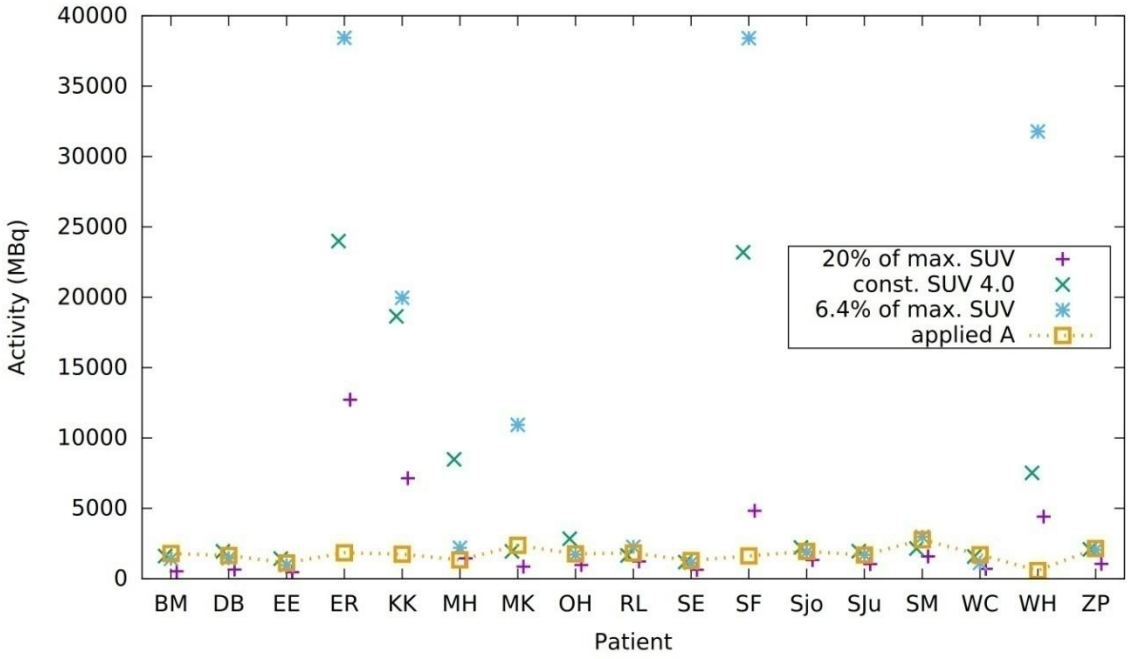

Figure 27: total activity measured for all patients with three different types of VOIs

As the outlying value for MH is the VOI constructed using a fixed SUV value and as the SUV is a measure for comparing applied and measured activity a different activity distribution seems likely. Probably the microspheres have been distributed more homogeneously in the liver than in other patients. This explanation does not work for the severe overestimation in patient MK as the threshold for the concerned VOI is dependent on the maximum value. However this threshold was defined as a mean value across the whole dataset and MK is one of the patients, where the optimal threshold value that has been calculated as described above is farthest from the mean. This makes an incorrect estimation using the mean value likely.

On the page after the next the total activity is plotted once again excluding the previously discussed outliers and with an estimate of the uncertainty for each VOI. The uncertainty has been calculated as discussed in section 3.2 and a possible uncertainty of the applied Y-90 activity has been neglected.

The VOIs constructed with a threshold of 20 % of the maximum SUV value (VOI 1) obviously underestimate the real activity and only in one of the 13 evaluated patients is the applied activity in the uncertainty range of the measurement result. However this was to be expected, because the threshold criteria should yield a roughly correct volume. A

conclusion that can be drawn from this is that a spill-out effect exists also for the real liver images and not only for the body phantom. As will be shown in a later section these VOIs already overestimate the real liver volume, but the activity is still severely underestimated. Therefore the applied activity is probably blurred over a large part of the image.

On the other hand the results for the other two types of VOI look very promising. For the VOI with a constant threshold of SUV = 4.0 (VOI 2) as well as for the VOI with a threshold of 6.4 % of the maximum SUV value (VOI 3) the applied activity is inside the uncertainty range for all but three patients. The relative uncertainty for all VOIs is around 23 % and values and uncertainties can be found in appendix, section A.4 .

It is not obvious if VOI 2 or VOI 3 gives a more precise estimate of the total activity. Subjectively the VOI 3 datapoints seems to be somewhat closer to the applied activity values, indicating this is the best available evaluation criterion. This assumption is also corroborated by analysing the normalized distance between measured value and applied activity. Viewing the arithmetic mean for VOI 1, VOI 2 and VOI 3 no real distinction can be found with values of 855, 851 and 902 MBq for the respective normalized mean difference between measured and applied activity. However the outlying values for patient MH for VOI 2 and for patient MK for VOI 3 distorted this mean value somewhat and therefore the geometric mean[9] has been calculated as well. This measure is less influenced by few outlying values and yields a mean normalized difference of 742, 320 and 211 MBq for VOI 1, VOI 2 and VOI 3 respectively.

Additionally the normalized difference has been plotted in figure 29. All datapoints except the outliers have been taken into account. The scatter plot shows the same results as discussed above: VOI 1 yields the most imprecise results VOI 2 and VOI 3 yield equally good results with a slight edge to VOI 3.

The conclusions to be drawn from the analysis of the total activity are very favourable. For the majority of patients the applied activity is measured in the image with an uncertainty of a few hundred MBq. While this uncertainty is still large the results are decent taking into account the large errors occurring in nearly all applications of quantitative imaging in nuclear medicine and the especially difficult circumstances, because of Y-90 being a pure beta emitter.

9

$$\bar{x}_{geom} = \sqrt[n]{\prod_{i=1}^{n} x_i}$$

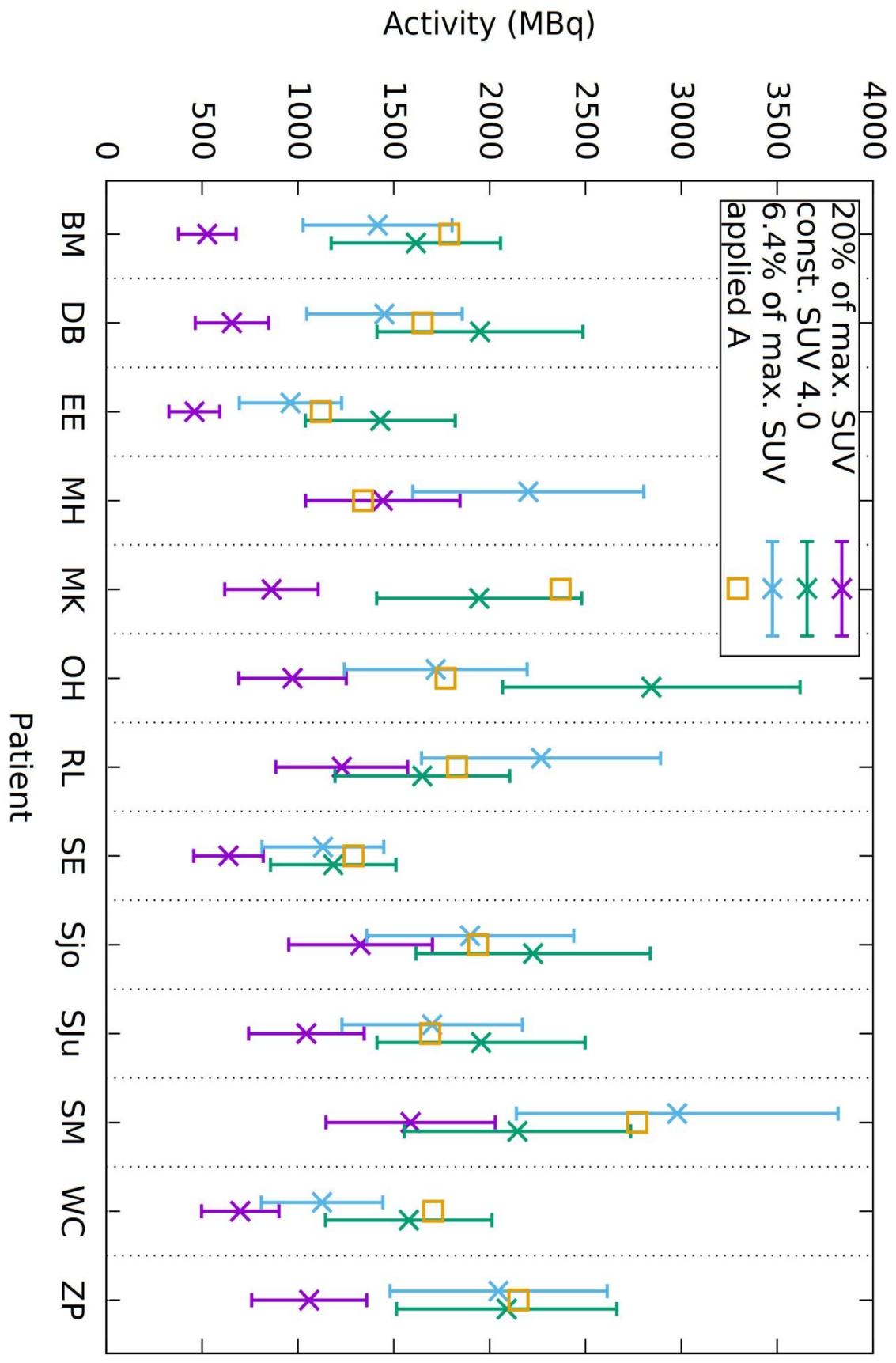

Figure 28: total activities and uncertainties obtained by evaluating the dataset with the three different types of VOI defined above, ER, KK, SF and WH have been excluded as outliers

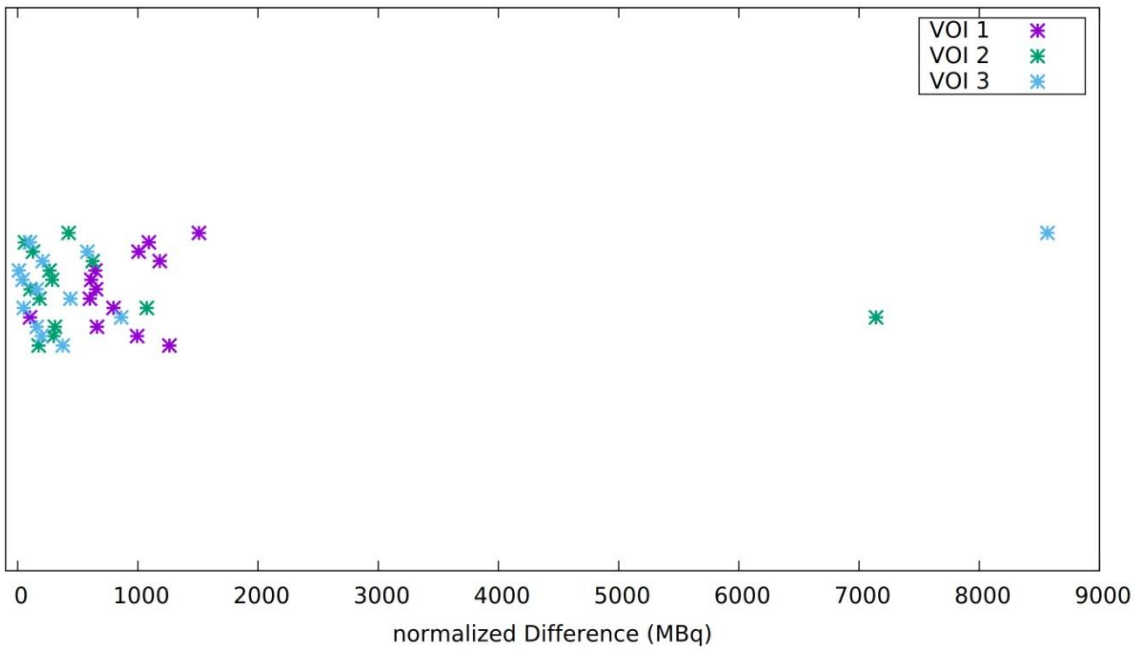

Figure 29: normalized difference between measured values and applied activity for VOI with 20 % of max. SUV value threshold (purple), VOI with constant threshold SUV=4.0 (green) and VOI with 6.4 % of max. SUV value threshold (blue)

The measurement of the total activity serves as an initial proof that the quantitative image reconstruction implemented in HybridRecon is working and no large bias leading to constant over- or underestimation of activity seems to be introduced this way. The fact that the most precise results are achieved with VOIs with a threshold of 6.4 % of the maximum SUV value shows that more or less all of the applied activity can be detected in the image. It also indicates that the artefacts visible in many images should not be taken into account during the evaluation. They should only be considered as a by-product of the reconstruction process and not as a spot, where activity that has really been applied seems to be concentrating on the image. Therefore the decision to exclude them using constraint ROIs during the evaluation has been correct.

Nevertheless the measurement of the total activity also shows that some form of spill-out effect cannot be avoided and that a VOI that yields a realistic estimate of the total activity has to be considerably larger than the real liver volume. Obviously this also creates an underestimation of the activity concentration, a fact that has to be borne in mind, when the activity concentration is used for quantitative evaluation.

3.6 Activity Concentration

To further investigate the behaviour of the activity concentration in this thesis VOIs with a volume equal to the real liver volume have been drawn. The mean activity concentration in these VOIs is plotted below in figure 30 and shows the measured concentration of the activity in the VOI spread homogeneously over the whole liver. Additionally the activity

concentration is calculated using the values for applied activity and known liver value. It should be noted that the assumption of a homogeneous activity distribution in the liver is highly unrealistic and is only used for the purpose of investigating a possible underestimation of the activity concentration due to the spill-out effects discussed in the previous section. Detailed values can be found in appendix A.5 .

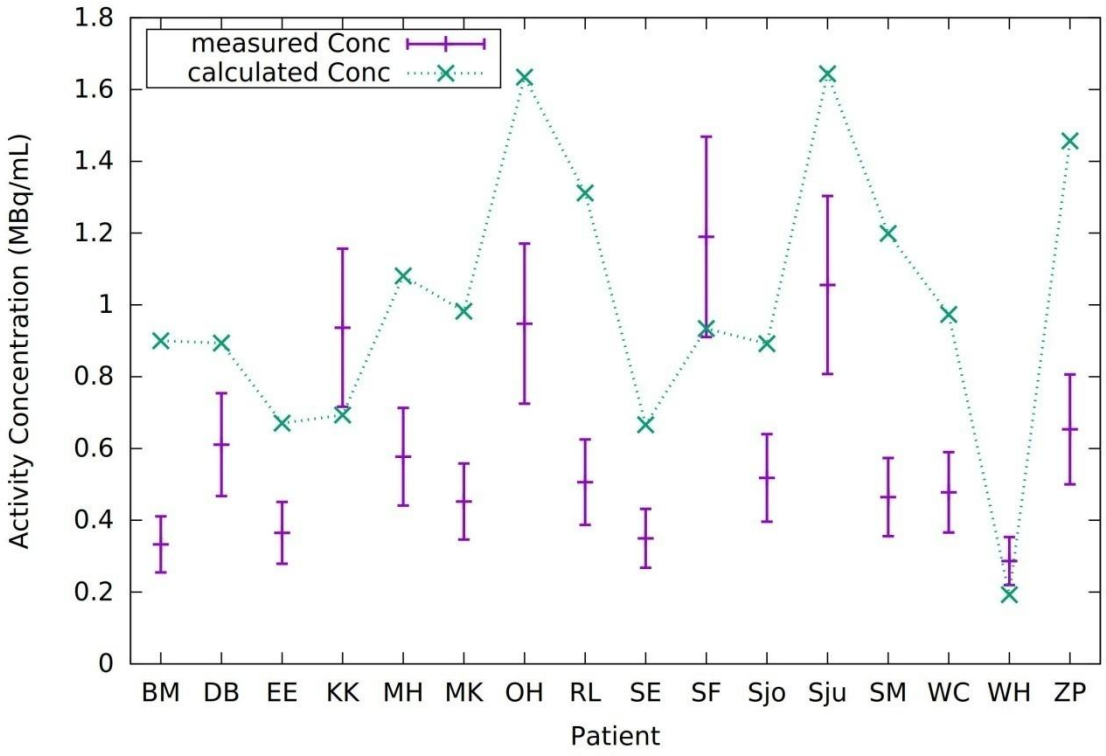

Figure 30: plot of the measured activity concentration in a VOI with a volume equal to the known liver volume (purple) and calculated activity concentration from the known values (green)

The first interesting feature of the plot above is that for the three patients KK, SF and WH, which have previously been identified as possible erroneous measurements an activity concentration is measured that, is higher than the calculated one. Patient ER is not included in this plot as no liver volume could be provided by AKH Vienna. A large dosage error for three patients in a row seems to be highly unlikely. Therefore the only reasonable explanation for measuring a higher activity concentration than can be achieved if the applied activity is spread homogeneously in the liver volume is an error during imaging or reconstruction. As already discussed in section 3.4.1 the former seems more likely.

Additionally it stands out that the measured activity concentration is always significantly lower than the calculated one. This was to be expected considering the results reviewed in the last section, because the total applied activity is blurred over the image.

It might be possible to define an empirical recovery factor using the quotient between measured and applied activity. This is probably not a very common approach for this sort of imaging as recovery factors usually are used for small features and might be considered completely redundant in high quality reconstruction like Monte Carlo based techniques. However a possible correction of the activity concentration will be considered in the dosimetry section.

3.7 Liver Volume

Another aspect that will be briefly considered during the evaluation in this thesis is the accordance of the real liver volume and the volume of the various volumes of interest. From the previous sections it is apparent that the volume of a VOI yielding a good estimate of the applied activity will be significantly larger than the volume of the patient's liver that has been defined during examination in the hospital. However the threshold of 20 % of the maximum SUV value was chosen in order to create a VOI that gives a realistic estimate of the real volume.

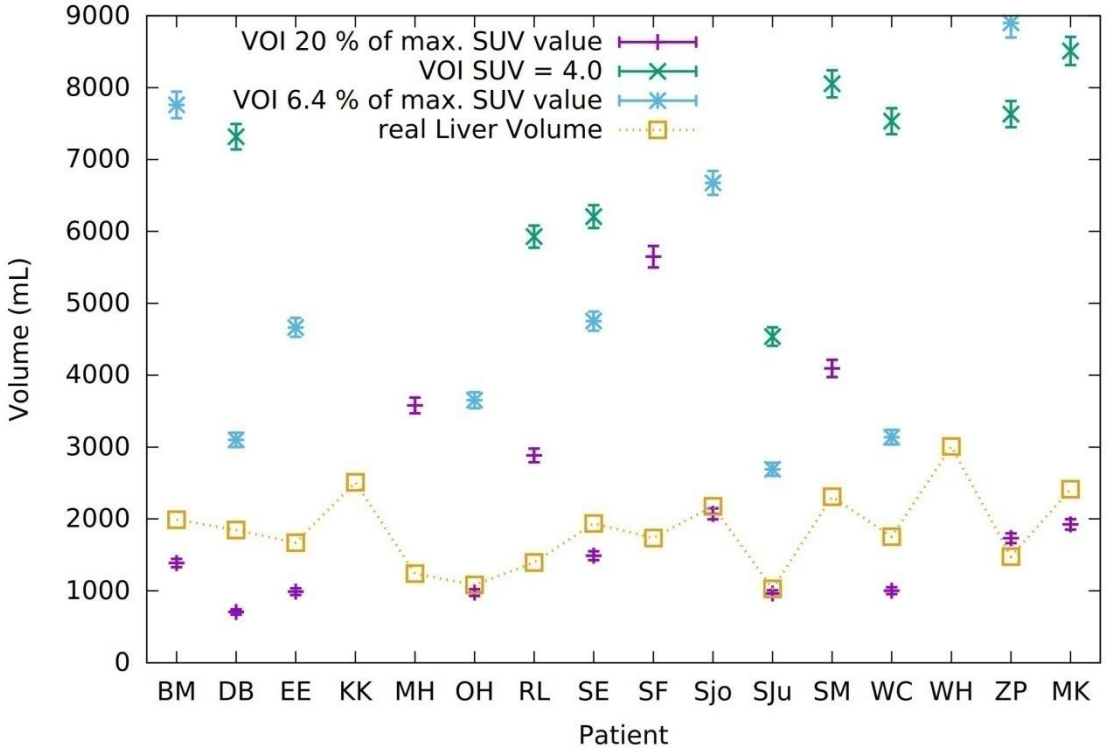

Figure 31: comparison of real liver volume (orange) and measured data. Patient ER is not included as no data of his actual liver volume is available

Considering the data plotted in figure 31 this assumption seems to be more or less valid. The relevant VOI indicated with purple dots consistently yields the best approximation of the liver volume. With the exception of the patients previously marked as outliers the estimation of the volume is even within a few hundred mL for most patients. The fact that for 7 patients the volume is underestimated by the 20 % threshold could signify that a

better criterion for creating a VOI representing the real volume could be found using a threshold, which is a bit lower. It should be pointed out that the indicated error bars for the measurements only estimate the uncertainty for the volume of a VOI caused by the rather larger voxel size. As the volume is very much dependent on the definition of the VOI, which does not show up in the uncertainty budget it is not surprising that for many patients the real value is far outside of the indicated uncertainty range.

3.8 Dosimetry

As already pointed out in the introduction to this work the knowledge about how much activity is applied and even where this activity is located does not fully enable one to judge the effect of a radionuclide in the body. To achieve this, a dose has to be calculated taking into account the effect of the radiation.

3.8.1 Pre-Treatment Calculations

As already briefly discussed in section 3.2 the usual procedure for SIRT is to calculate a desirable dose to the tumour from previously known values and to administer an according amount of activity during the treatment.

In the package insert for SIR-spheres (Sirtex Medical Limited, 2016) and in the relevant literature (Dieudonne, et al., 2016), (Spahr, et al., 2017) different approaches can be found. They all have in common that any long range interactions are neglected and the assumption is made that all energy will be released locally. As the mean range of Y-90 beta radiation is 4.0 mm compared to a voxel size of 4.8 mm this approach seems reasonable and a possible error has been included in the uncertainty budget. Together with the fact that the microspheres stay permanently in the body and are not affected by the metabolism and therefore only the physical half-life needs to be considered and no time dependence exists dosimetry for SIRT is greatly facilitated.

Hence the most intuitive approach is to define a constant conversion factor between activity and dose. According to the ICRU (The international Commission on Radiation Units and Measurements, 2011 p. 27) the dose is defined as:

"The absorbed dose, D, is the quotient of $d\bar{\varepsilon}$ by dm, where $d\bar{\varepsilon}$ is the mean energy imparted by ionizing radiation to matter of mass dm, thus $D = \frac{d\bar{\varepsilon}}{dm}$ Unit: $J\,kg^{-1}$ The special name for the unit of absorbed dose is gray (Gy)."

Following the MIRD (Committee on Medical Internal Radiation Dose) guidelines (Bolch, et al., 2009) the mean absorbed dose D in a given tissue r_T can be written as:

$$D(r_T) = \sum_{r_S} \tilde{A}(r_S) \cdot S(r_S \rightarrow r_T)$$

$\tilde{A}(r_S)$ time integrated activity in source r_S

$S(r_S \rightarrow r_T)$ S value *"radionuclide-specific quantity representing the mean absorbed dose rate to target tissue r_T"* (Bolch, et al., 2009 p. 478)

As stated above only the physical decay needs to be considered for the activity

$$\tilde{A}(r_S) = \int_0^\infty A(rs,t) = A_0 \int_0^\infty e^{-\lambda t}\, dt = \frac{A_0}{\lambda}$$

A_0 activity at t=0, applied activity

λ decay constant $\lambda = \ln(2)\,/t_{1/2}$

and all energy will be considered as being absorbed in the liver.

$$S(r_S \rightarrow r_T) = \frac{1}{m(r_T)} \sum_i E_i Y_i \Phi(r_S \rightarrow r_T, E_i) = \frac{\langle E \rangle}{m(r_T)}$$

$m(r_T)$ mass of target tissue

$E_i Y_i$ mean energy of the ith transition times probability of this transition

$\Phi(r_s \rightarrow r_T, E_i)$ fraction of emitted energy absorbed in the target tissue

$\langle E \rangle$ mean energy of beta-decay

Φ can be set to 1, because of the assumption that all energy is released locally. If this is not the case it will take a value between 0 and 1.

Therefore the absorbed dose can simply be described as

$$D = \frac{\langle E \rangle\, A_0}{m\, \lambda} = \frac{\langle E \rangle t_{1/2}}{\mathrm{m}\, \ln(2)}$$

$$\boxed{D(Gy) = \frac{933\ keV \cdot 64\ h\ \cdot A_0}{m\ ln(2)} = \frac{49.67 \cdot A_0(GBq)}{m(kg)}}$$ [10]

To insert the mass of the whole liver for m would imply that the activity gets distributed homogeneously across the whole liver. Therefore a more complex formula is used and the doses to tumour and healthy liver tissue are considered independently.

$$D_T = \frac{49.67\ A_T}{m_T} = \frac{49.67 A_0}{\frac{m_T A_0}{A_T}} = \frac{49.67 A_0}{m_T \left(1 + \frac{A_0}{A_T} - \frac{A_T}{A_T}\right)} = \frac{49.67 A_0}{m_T \left(1 + \frac{A_{NL}}{A_T}\right)}$$

[10] Using a slightly different mean energy of 926.7 keV Spahr, et al. (2017) calculate the constant as 49.38

Including the lung shunting fraction L the so called partition model can be derived. With the knowledge of tumour mass m_T, liver mass m_L lung shunting fraction and the ratio of activity uptake A_T/A_{NL} in the tumour and the healthy liver tissue, doses to the tumour and healthy liver can be computed for a given activity. The inverse formula can be used to define the necessary amount of activity before the treatment.

$$D_T(Gy) = \frac{49.67\ A_0\ (GBq)(1-L)}{m_T(kg)\ \left(1+\frac{A_{NL}}{A_T}\right)}$$

$$D_{NL}(Gy) = \frac{49.67\ A_0\ (GBq)(1-L)}{(m_L(kg)-m_T(kg))\ \left(1+\frac{A_T}{A_{NL}}\right)}$$

This formula can be generalized to describe the dose to any given part with the mass m_i and activity uptake A_i (Spahr, et al., 2017)

$$\boxed{D_i(Gy) = \frac{49.67\ A_0\ (GBq)(1-L)}{m_i(kg)\ \left(1+\frac{A_{0\backslash i}}{A_i}\right)}}$$

3.8.2 Tumour Volume

An essential variable for the dosimetric calculations in this section is the volume and mass of the patients' tumours. Unfortunately this quantity is hard to define as many cases feature a multitude of small tumours or the edges are not clearly defined.

Due to this problem the formulae above are often not used in clinical practice. As already stated in section 2.5 in this project the BSA model was applied to define the necessary amount of activity.

$$A(GBq) = BSA - 0.2 + \frac{\%\ tumour\ involvement}{100}$$
$$BSA(m^2) = 0{,}20247 \cdot height(m)^{0{,}725} \cdot weight(kg)^{0{,}425}$$
$$\%\ tumour\ involvement = \frac{V_{Tumour}\ \cdot 100}{V_{Liver}}$$

For the same reason the tumour volume was not precisely measured, but the tumour involvement was estimated by the treating physician relying on his expertise and the general state of the patient's liver. This is doubtless a valid approach, but introduces a problem for dosimetric calculations. As no dose can be calculated from the BSA model a crossover to the partition model has to be accomplished for subsequent dose calculations.

The ratio of activity uptake in tumour versus healthy liver tissue is available from the MAA SPECT performed during the preliminary examinations. Unfortunately the lung shunting fraction is unknown and will therefore be assumed to be 0. Thereby only a small additional uncertainty is introduced as the real value for L can usually be expected to vary between 0 and 0.1 (see section 2.2).

In order to calculate doses an estimate for the tumour volume needs to be created without being able to rely only on data supplied by the hospital. In order to achieve this, two different approaches have been devised and applied in this thesis. Below the tumour volume is derived from the formula for the BSA model inserting all the other known quantities.

$$V_T(mL) = (A(GBq) - BSA(m^2) + 0.2) \cdot V_L(mL)$$

As visible in table 7 this approach yields negative tumour volumes for about half of the patients. As these results are obviously impossible all values should be considered with some reserve.

Name	V liver (mL)	V Tumour (mL) BSA	V NT (mL) BSA	V Tumour (mL) VOI	V NT (mL) VOI	VOI Thres. (%)
BM	1989	-468	NaN	509	1480	32
DB	1846	359	1487	274	1572	32
EE	1670	-1150	NaN	438	1232	32
MH	1240	-123	NaN	565	675	40
MK	2413	1378	1035	721	1692	32
OH	1083	91	992	534	549	32
RL	1395	470	925	638	757	60
SE	1937	-322	NaN	243	1694	32
Sjo	2175	652	1523	580	1595	32
Sju	1028	414	614	181	847	40
SM	2310	2020	290	453	1857	60
WC	1753	144	1609	193	1560	32
ZP	1476	758	718	601	875	40

Table 7: tumour and healthy liver volumes (V NT) calculated using the BSA model and measured using a VOI, the VOI threshold is given in the last column

Alternatively the tumour volume was estimated using the Y-90 Bremsstrahlung SPECT scans. This is a reasonable idea, because nuclear imaging is widely used for tumour diagnostics although usually with far better image quality. For determining a threshold value likely to yield a realistic estimate of the tumour volume the data from the IEC NEMA Body Phantom was used. For the body phantom thresholds of 32.5 %, 32.4 % and 30.2 % of the maximum value yield the correct volume for the three largest inlays respectively.

Therefore the rounded mean of 32 % of the maximum value was used to determine VOIs representing the tumourous volumes in the patient images.

The doses calculated from those volumes using the formulae of the partition model given above seemed reasonable except in five cases, where unrealistically large or small doses resulted. To get the best possible estimate the calculation was redone for these five patients using higher thresholds of 40 % or in two cases 60 %. Although this introduces an arbitrary element it seems a better solution than to compare the measured values with totally unrealistic calculations.

All the same it is obvious that the calculated dose values can be biased, because data from the measurement is used to calculate values for comparison with that same measurement. However due to the fact that the important data for tumour values was not available this still allows some pre-treatment dosimetry, which would otherwise have been impossible.

3.8.3 Uncertainty

In order to meet the metrological requirements also for the calculated doses an uncertainty budget has been compiled in the course of this thesis. Therefore the uncertainties of the individual factors of the pre-treatment dose calculation (as also given in table 8) had to be considered and allowed for. The total uncertainty consists of

$$\sigma(D_T) = \frac{\sigma(const)\ \sigma(A_0)\ (1-\sigma(L))}{\sigma(m_T)\left(1+\frac{1}{\sigma\left(\frac{A_T}{A_{NL}}\right)}\right)}$$

$$\sigma(D_{NL}) = \frac{\sigma(const)\ \sigma(A_0)\ (1-\sigma(L))}{\left(m_L(kg)-\sigma(m_T)\right)\left(1+\sigma\left(\frac{A_T}{A_{NL}}\right)\right)}$$

Applying the Gaussian law of error propagation given in section 3.2 this can be written as

$$\sigma(D_T) = D_T \cdot \cdot \sqrt{\frac{1}{const^2}\sigma^2(const)+\frac{1}{A_0^2}\sigma^2(A_0)+\frac{1}{L^2}\sigma^2(L)+\frac{1}{m_T^2}\sigma^2(m_T)+\frac{1}{\left(\frac{A_T}{A_{NT}}\right)^2\left(\frac{A_T}{A_{NT}}+1\right)^2}\sigma^2\left(\frac{A_T}{A_{NT}}\right)}$$

$$\sigma(D_{NT}) = D_{NT} \cdot \cdot \sqrt{\frac{1}{const^2}\sigma^2(const)+\frac{1}{A_0^2}\sigma^2(A_0)+\frac{1}{L^2}\sigma^2(L)+\frac{1}{m_T^2}\sigma^2(m_T)+\frac{1}{\left(\frac{A_T}{A_{NT}}+1\right)^2}\sigma^2\left(\frac{A_T}{A_{NT}}\right)}$$

	Dose Patients	Dose Body Phantom
$\sigma(const.)/const.$	10.00 %	10.00 %
$\sigma(A_0)/A_0$	5.00 %	20.00 %
$\sigma(L)/L$	10.00 %	/
$\sigma(m_T)/m_T$	20.00 %	2.00 %
$\sigma(A_T/A_{NL})/(A_T/A_{NL})$	5.00 %	5.00 %
total uncertainty	25.87 %	23.57 %

Table 8: uncertainty budget for the calculated dose to patients and body phantom

The error introduced by the constant takes into regard that the dose deposition is supposed to happen locally as explained previously. Because the calibration of activity for application to the patients is performed with the VEENSTRA Instruments Dose Calibrator in a dedicated set-up a smaller uncertainty than for the phantom measurements can be postulated in accordance with the instrument's specifications. As the lung shunting fraction usually does not exceed an amount of 10 % of the applied activity this value is conservatively assumed to be the uncertainty added by setting L=0.

The problems regarding the definition of tumour volumes are taken into account by assuming at least 20 % uncertainty. The ratio of activity in tumour and healthy tissue is derived from the MAA SPECT scan. Because these scans are rather precise and an exact estimate is hard to accomplish an uncertainty of 5% will be assumed.

For the body phantom the dose can also be calculated before the measurement and a similar uncertainty budget can be obtained. The uncertainty for measuring the applied activity is defined as 20 % as explained in section 3.2 and the lung shunting fraction does not enter into the formula. The masses and the activity ratio for the respective inlays are not measured, but calculated from the volumes given in the datasheet (EN 61675-1, 2014). So only a small uncertainty is introduced, due to possible small errors in filling the inlays, resulting air bubbles and possible differences to the calculated amounts of activity in each inlay.

The uncertainty budget for the doses obtained by analysis of the images has already been discussed in section 3.2

3.8.4 Post-Treatment Dosimetry

Two different approaches were developed in this thesis to extract dosimetric information out of the image data. The dose is calculated from the activity concentration in both cases as follows (Dieudonne, et al., 2016):

$$D(Gy) = \frac{49.67 \cdot 10^{-6}\, A_{Conc}\,(Bq/mL)}{\rho(g/mL)}$$

Using an average tissue density $\rho = 1.04\ g/mL$ the dependency on volume is converted to a dependency on mass. The value for the activity concentration is obtained in two different ways. First the volumes of interest drawn to determine the tumour volume were further analyzed and a tumour dose was calculated using the values for maximum and mean activity concentration. To estimate the exposure of the healthy liver a VOI with the size of the real liver volume was drawn and the mean between the highest activity concentration not included in the tumour VOI and the minimum activity concentration was calculated representing the mean dose to healthy liver tissue.

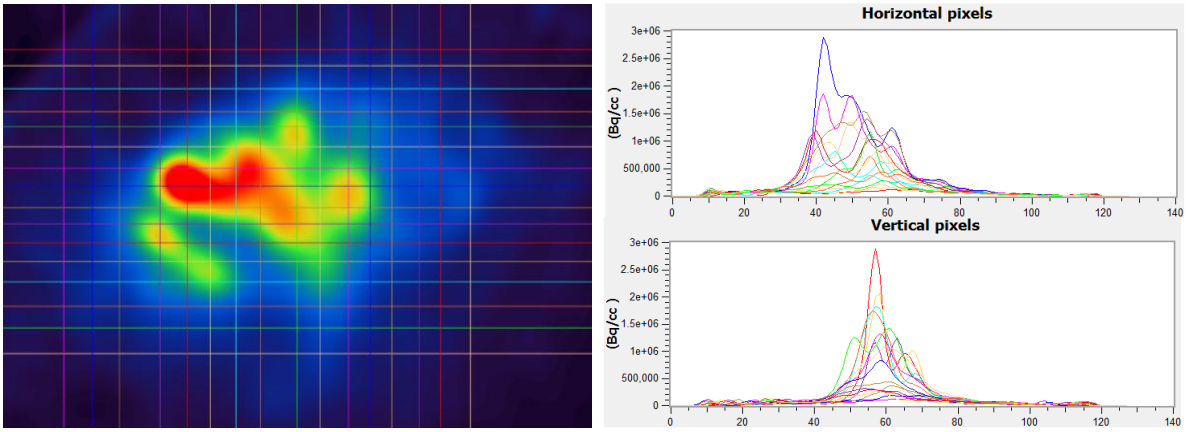

Figure 32: in one layer of the image horizontal and vertical activity concentration distributions are evaluated using Hybrid Viewer

The second approach is more sophisticated and utilizes the activity profiles that can be obtained in Hybrid Viewer. As visible in figure 32 an evenly spaced grid of activity profiles is extracted from one layer of each image. The chosen layer includes the voxel with the highest activity concentration and is probably the most representative.

The activity concentration is then further analyzed with a MATLAB (The MathWorks, Inc., 2017) script written for this purpose and included in this thesis (see appendix B.2) with the aim to recreate a two dimensional activity distribution that can be converted into a dose.

In a first step each horizontal and vertical activity concentration profile is placed in the appropriate row or column of a matrix. (Figure 33a) Next each profile is copied in all neighbouring columns respectively rows of the matrix, but multiplied with an exponential factor that causes a decrease of the values. The values are scaled down the more the further the column or row is located from the actual position and so an interpolation of the space between the individual rows and columns obtained from Hybrid Viewer is achieved. (Figure 33b) In a next step the matrixes of horizontal and vertical concentration values are added up and renormalized.

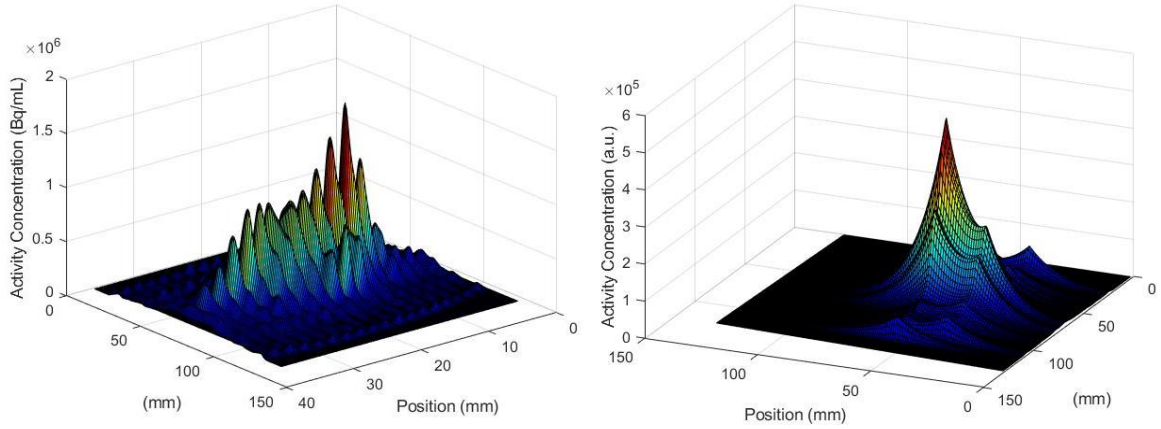

Figure 33a: the vertical activity concentration profiles are placed in the appropriate spot (left), 33b: the distance between them is interpolated (right)

Thus a representation of the activity concentration of one slice of the image is created in MATLAB and converted into a dose in the next step. Additionally a moving mean is applied that replaces the value of every pixel with the mean of that pixel and its adjourning neighbours. This is done to smooth out artefacts from the previous steps, but is only used for plotting and does therefore not bias the evaluation.

The data can be analyzed much deeper in MATLAB and the possibility to apply a recovery coefficient to correct for too low activity concentration values due to spill-out effects can be investigated.

The data will be presented both graphically and numerically. The mean value of the highest 20 % of doses is used as a representation of the tumour dose and the mean value of all values lower than 70 % of the maximum dose is used as a representation of the dose to healthy liver tissue. However the lowest 5 % of values are not included in this calculation as they likely represent only background noise.

Moreover a 3D plot is created to allow a graphical representation of the dose distribution as well as a histogram plot.

3.8.5 Body Phantom

Before analyzing the patient data the technique described above will be used to evaluate the images of the NEMA IEC Body phantom.

In figure 34 the good agreement between the relevant layers of the SPECT image and the dose distribution created in MATLAB can be observed. The structure of the five largest inlays is clearly visible and a pronounced decrease of dose values is separating the individual inlays. This illustrates the possibility to obtain activity distributions closely reflecting the real object and to create a realistic dose distribution for one layer utilizing

the technique described above. The image in figure 34 is already modified with a recovery coefficient that is different for every inlay and was applied to the relevant part of the distribution.

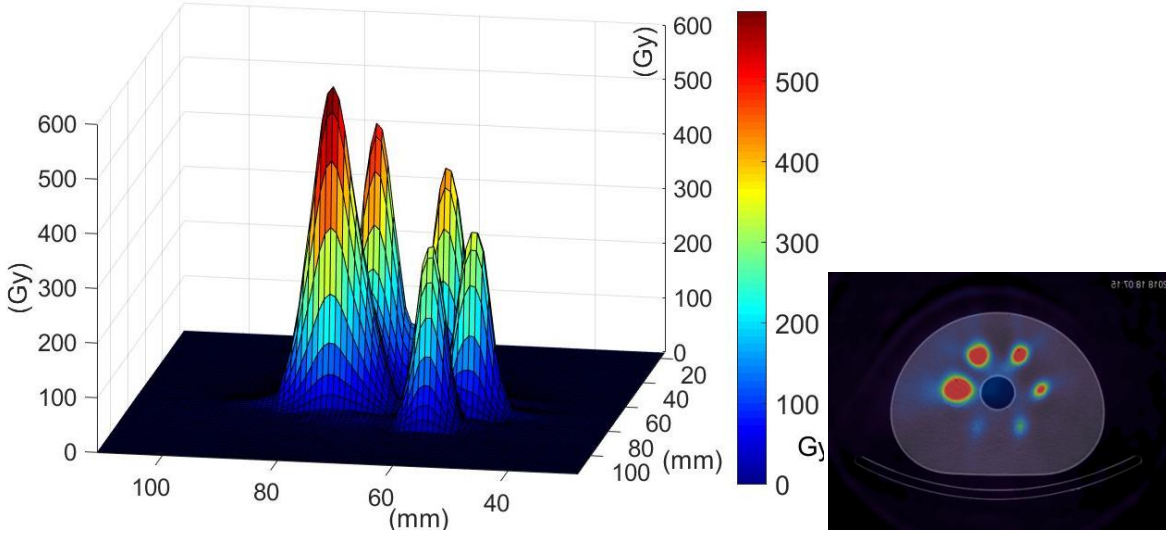

Figure 34: dose distribution in the most relevant image layer of the body phantom, the 3D plot is a very good representation of the real distribution. The activity concentration was modified with a recovery factor before dose calculation

In figure 35 the comparison between calculated doses and measured values with and without a recovery coefficient is plotted (detailed data can be found in appendix A.6). As a constant activity concentration was applied to every inlay the same dose should theoretically be obtained every time. However the size of the inlays is at the lower limit of the resolving power of the Y-90 SPECT resulting in pronounced spill-out effects as previously discussed. The smallest inlay with 1 cm diameter will not be included at all in this evaluation as hardly any reliable values can be obtained for it.

Therefore it is to be expected that the obtained dose values are lower than the theoretical calculations and also that the values decrease with decreasing inlay diameter. To compensate for this a recovery coefficient was applied. The coefficient is the same as in section 3.1.2 and should correct the spill-out effect and therefore a possible underestimation of the activity distribution. The additional uncertainty is allowed for.

The expected underestimation of measured dose values is very pronounced, as only about half of the calculated dose is measured. Additionally the values are decreasing with the inlay diameter. It is noteworthy that the dose in the smallest analyzed inlay with a diameter of 1.3 cm can no longer be distinguished from the value obtained for the cold area, which is theoretically exposed to D= 0, but for which a dose of D= 29.7 +/- 7.0 Gy is measured. The second smallest inlay (diameter 1.7 cm) shows a mean dose of D= 73.5 +/-17.3 Gy and is therefore well defined. This allows one to estimate the resolution power of Y-90 SPECT imaging in similar cases to be between 1.3 and 1.7 cm.

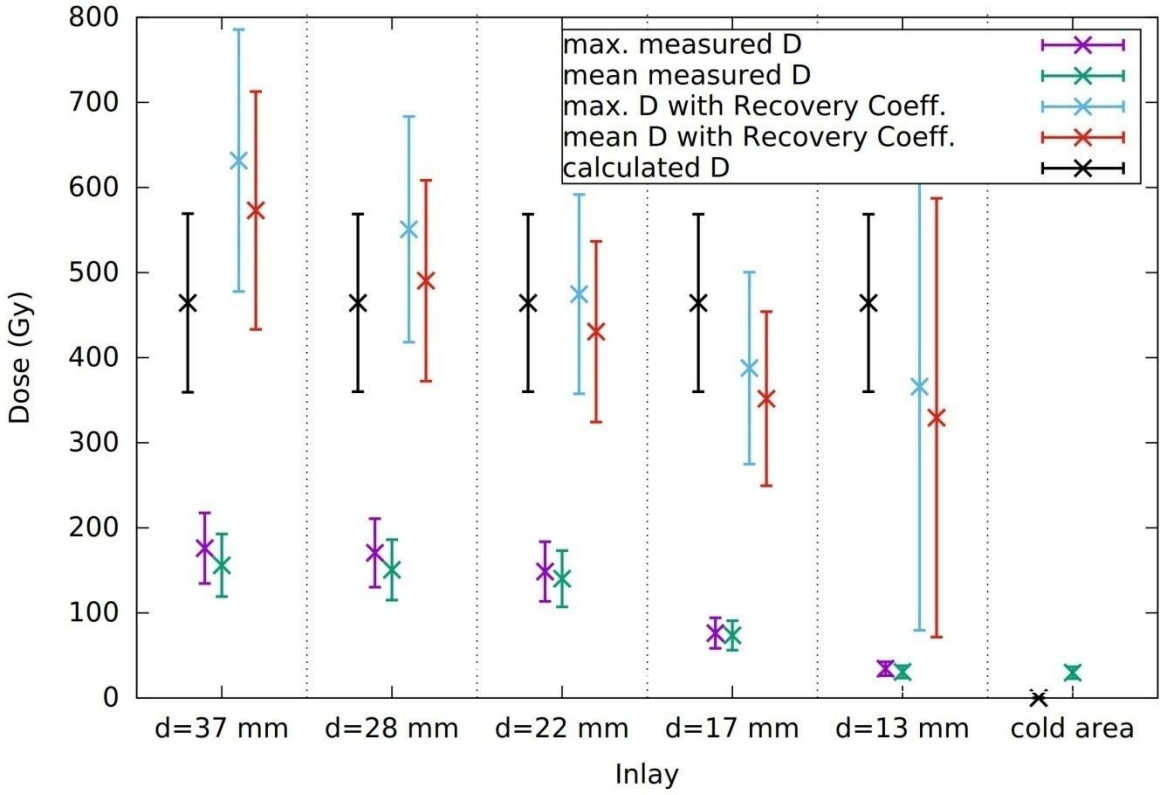

Figure 35: comparison of calculated dose (black) and measurements without recovery coefficient (purple, green) and with a correction for spill-out (blue, red)

The correction with a recovery coefficient leads to a slight overestimation of the real value and does not manage to overcome the decrease in dose with decreasing inlay size despite the fact that a different recovery coefficient was applied to each inlay. Nevertheless the measured results are within the uncertainty range of the calculated values for every inlay. The smallest inlay shows such a large uncertainty that the resulting dose for this inlay can be considered completely meaningless. This is however consistent with the observation that this dose cannot be separated from the cold background with any accuracy.

Equally interesting to observe is the small difference between maximum and mean measured dose values. This indicates a high dose to an extended area and is once again consistent with the observations of the 3D plot.

In conclusion the evaluation of the body phantom can serve as prove of concept for post treatment dose measurements in Y-90 SPECT. The well known parameters of the phantom measurement allow a reliable calculation of dose values and the measured values are in rather good accordance after applying a necessary correction for the spill-out. Even the uncertainty is not excessive in comparison to other studies in nuclear medicine (Shcherbinin, et al., 2008) (Mikell, et al., 2015). The high uncertainty for calculated values as well as measured ones is obtained due to the challenge of measuring the applied activity with any precision in a non standard geometry.

3.9 Post-Treatment Patient Dosimetry

The whole dataset of 13 patients excluding the 4 outliers was evaluated as previously described using VOIs and the activity concentration distribution created in MATLAB. An example of the latter can be found in figure 36 together with the image layer it was created from. As the activity distribution in real patients is far more complex than in a phantom the influence of only analyzing one layer of the images also needs to be evaluated.

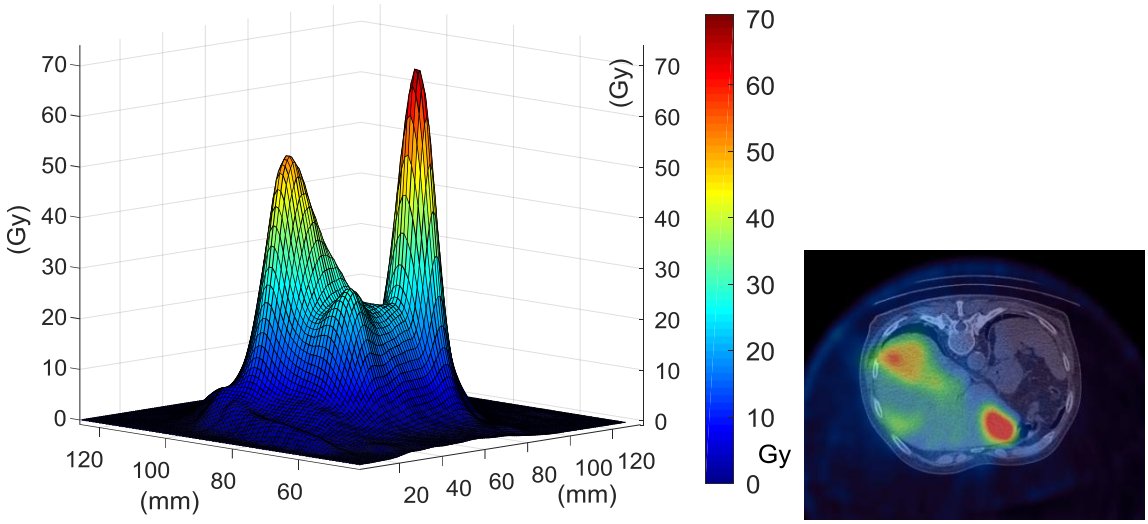

Figure 36: patient SJo, the dose distribution as calculated in MATLAB and the relevant layer of the SPECT/CT image are in good accordance

As for the body phantom the agreement between the calculated dose distribution and the image seems to be fine. In figure 37 and 38 the doses to tumour and healthy liver tissue with and without a correction with a recovery coefficient are plotted. All values depicted in the plots can be found in the appendix in section A.7.

In orange colour the dose values for a homogeneous distribution of the applied activity in the liver volume are depicted. Black and red mark the calculated doses, black indicating that the tumour volume was obtained from a VOI. The doses calculated with tumour volumes derived from the BSA model are drawn in red.

It is immediately visible that the latter approach cannot be considered reliable as only for 8 patients tumour volumes could actually be calculated and of those eight a higher dose to healthy tissue than to the tumour is computed in four cases. Because it is very likely that these results are erroneous, little credibility can be given to the values remaining in the other four cases.

The calculated doses relying on tumour values obtained by drawing a VOI could be biased because data from the measurement is used. All the same the results seem reasonable in most cases. The tumour dose is always higher than for a homogeneous activity

distribution and in the range of what can be expected for SIRT treatment. Moreover the calculated doses to healthy liver tissue are below a hypothetical homogeneous distribution in all but one case and only one other value is so low as to be definitely unrealistic.

Three different measured doses are included in the plots. For the tumour dose the maximum measured dose is indicated in purple. The mean dose found in the VOI used for defining tumour volume is indicated in green and blue is the mean dose to the tumour extracted from the dose distribution in MATLAB. To obtain the latter value the mean of all pixels with a dose of 80 % of the maximum or higher was used just as in the body phantom

The healthy liver dose is evaluated using the minimum dose found in a liver sized VOI (purple) the mean dose in that VOI excluding the tumour volume (green) and the mean from the MATLAB dose distribution utilizing all values between 5 % and 70 % of the maximum value.

A general statement about the agreement of measured and calculated dose is hard to make. For the tumour dose in three cases there is no measured value within the uncertainty range of the calculated dose, for the healthy liver tissue this happens in 6 cases. The measured tumour doses (purple and blue) are only in two of 13 cases below a hypothetical homogeneous dose distribution and the measured doses to the healthy liver are never higher than a homogeneous activity distribution would be.

This rough quality evaluation points to a basic reliability of the measured dose values, albeit with a high uncertainty and a high fluctuation. A separation between the dose to the tumour and to the healthy liver can be observed and emphasises the basic principle of selective internal radiation therapy.

The approach of calculating a dose from the mean concentration value of a VOI is apparently not successful. The tumour doses measured this way are below the values for a homogeneous dose in the majority of cases and also do not agree well with the calculated tumour dose values.

The behaviour of the other two values is similar to what has been observed in the body phantom probably illustrating again an extended area exposed to higher doses.

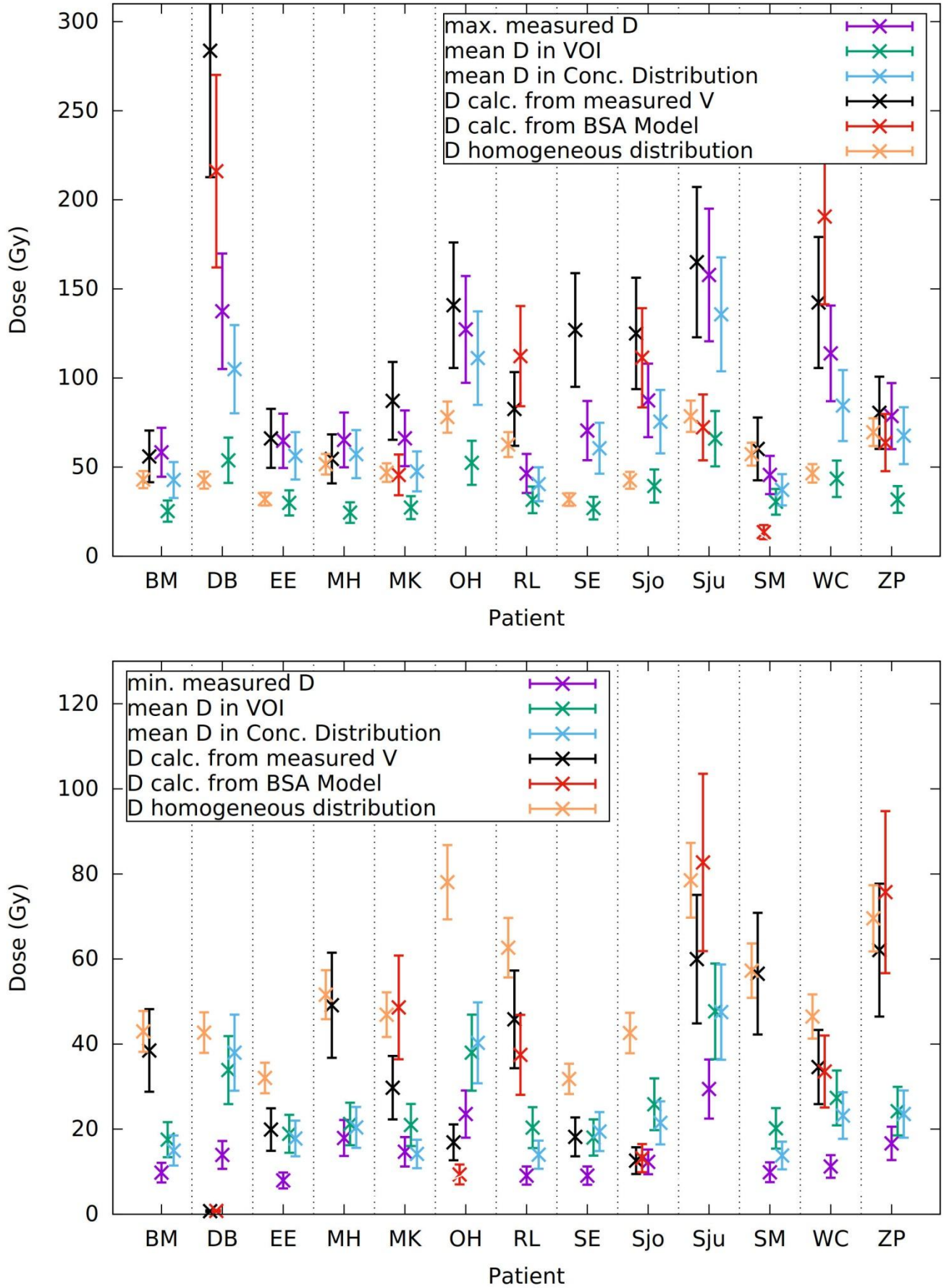

Figure 37 Top: comparison of calculated and measured dose to the tumour, Bottom: comparison of doses to healthy liver tissue, no spill-out correction is applied.

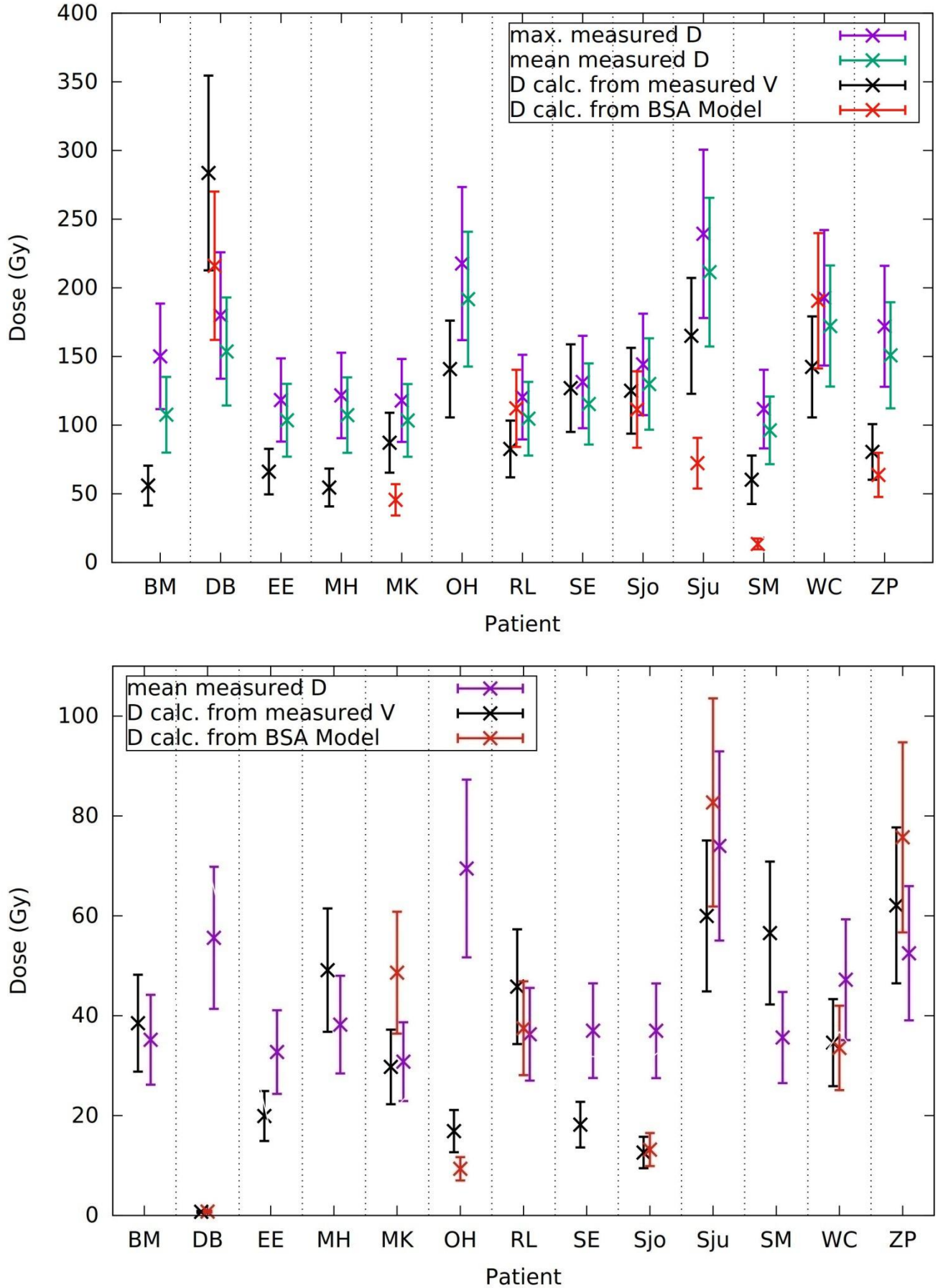

Figure 38 Top: comparison of calculated dose and dose measured in MATLAB and modified with a recovery coefficient, Bottom: comparison of calculated dose and spill-out corrected dose to healthy liver tissue

The tumour and healthy liver dose values plotted in figure 38 have been modified by multiplication with a recovery coefficient obtained by comparing measured and calculated activity concentration for a homogeneous activity distribution in the liver using the data discussed in section 3.6. As the tumours are larger structures than the inlays of the body phantom and due to the high quality of the Monte Carlo based reconstruction, the application of a recovery coefficient is uncommon for this type of evaluation.

Therefore it is not completely unexpected that the obtained results are rather unpromising. The dose values are overcorrected and overestimate doses to tumour and liver in the majority of cases.

Furthermore the doses for all pixels have been summarized in histograms, omitting only the lowest 5 % of values. Two examples of those (patients EE and MH) can be found in figure 39. For both patients the majority of doses is below 10 Gy and can probably be assigned to the background or regions outside of the liver. For both patients a significant number of pixels with a dose higher than 60 Gy are visible. Those are probably the peak doses found in the tumourous regions. Moreover a slight minimum between 35 and 40 Gy can be observed and a possible explanation for that is a kind of border region. High doses can be assigned to the tumour and lower ones to healthy liver tissue. However this minimum is not visible in all patients and is not pronounced enough to be really considered significant.

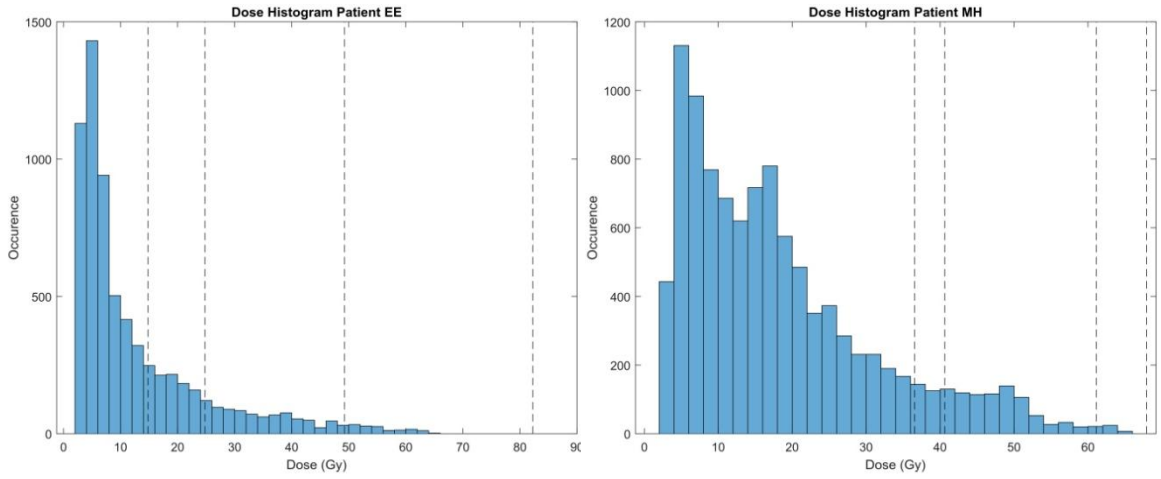

Figure 39: histograms of the dose distribution for patients EE and MH. The dashed lines indicate the ranges for calculated doses to healthy liver and tumour, no recovery coefficient is applied

In summary, estimations of doses to tumours and healthy liver tissue can be obtained from the patient data and a general comparison with calculated values can be performed. Although this comparison points to a relatively good agreement between calculated and measured doses detailed insights cannot be gained as calculated and measured dose values are both affected with high uncertainly. This is not so much due to the statistical

errors that can be allowed for and have been discussed in the uncertainty budget, but due to systematic problems. For the calculated doses the unknown tumour volumes can only be roughly approximated and an estimation of the generated uncertainty is hard to achieve. Equally challenging is the representation of the pixelized dose distribution in one value and the decisions made in summing up the data.

However in almost all cases a distinct separation between the doses assigned to tumour and healthy liver tissue and a difference from a hypothetical homogeneous distribution can be observed. This is in accordance with the principle of SIRT and therefore it can be considered as a basic proof for the quality of the dose estimation performed in this section. In summary it was shown that the quantitative evaluation of Y-90 SPECT allows computing dose values directly from post-treatment imaging. The dose distributions presented in this section can be used to perform much more detailed dosimetry than when using pre-calculated values.

4 Conclusions

To the best of my knowledge this project is the first to perform quantitative evaluation of Y-90 SPECT/CT images using real patient data and HybridRecon. Although reconstructions using Monte Carlo simulation are widely considered to be the gold standard in quantitative SPECT image reconstruction, high calculation times have usually inhibited wider use in clinical practice. With the implemented algorithms described in section 2.3 this is no big issue with HybridRecon, but the general quality of the reconstruction and the quantitative values need yet to be evaluated.

Proof of concept can already be concluded from the measurements performed on a Jaszczak and a NEMA IEC Body phantom in the beginning of this thesis. The SUV value for the Jaszczak phantom was very precise, the activity only slightly underestimated and a conversion factor from counts to activity was established with a very small uncertainty.

Despite the pronounced underestimation of the activity in the respective inlays of the body phantom the results are equally promising. The total activity is estimated fairly accurately and the spill-out effect causing the large underestimation of activities in small structures is well documented and can be corrected for. Therefore the activity is measured precisely for larger structures and no systematic errors seem to be introduced, when reconstructing images containing small centres of activity.

The same overall conclusion can be drawn from the total activity measured in all patient images. The selective uptake of activity can be observed qualitatively and is in accordance with the theory of SIRT.

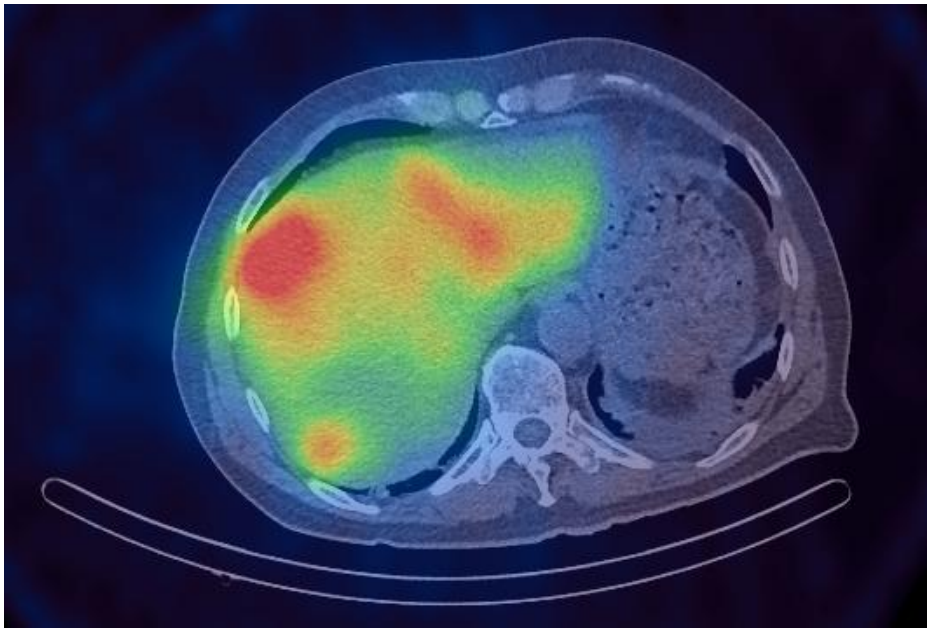

Figure 40: patient ZP, example for the well defined difference in activity uptake in tumours and healthy liver tissue, combined SPECT and CT image

Although the total activity is distributed in a larger part of the image than should be expected to be the distribution in the real patient, the total measured values are still in rather good agreement with the applied activity for most cases. The four outliers yielding completely different results have been imaged consecutively and therefore an error during imaging or in the detector set-up seems much more likely than a reconstruction error only visible in these four patients.

Moreover the images confirm the basic assumptions of SIRT treatment. The applied activity can be detected in the liver area thereby making a large shunting of activity into other organs for example the gastro-intestinal tract highly unlikely. Additionally the selective absorption in tumourous tissue can be observed and the quantitative reconstruction could provide further indications of the development of the disease to an observer with profound medical knowledge.

The image quality of Y-90 SPECT is low in comparison with Tc-99m SPECT or other optimized imaging techniques in nuclear medicine. Nevertheless overcoming the problems introduced by the continuous bremsstrahlung spectrum allows a direct quantitative and qualitative evaluation of the SIRT treatment and can help to reduce the necessity to rely on pre-treatment imaging for dose calculations and deeper understanding of the disease.

In further projects quantitative Y-90 SPECT imaging could also help to solve the pending question, whether the Tc-99m-MAA SPECT is actually an accurate representation of the distribution of SIRT microspheres.

A big issue affecting comparability of different image evaluations is the arbitrary definition of VOIs widely used in nuclear medicine. It is common in clinical practice to expand a VOI until all activity that is considered relevant is included, but this approach introduces a large bias and depends on the operator a good deal. Therefore different ideas for a comprehensible definition of VOIs were employed during this thesis. For finding criteria to construct VOIs it was referred to suggestions found in the literature. Even if the use of the selected criteria beyond this project is unclear the stringent approach guarantees reproducibility.

Equally uncommon in clinical practice are the creation of an uncertainty budget and the observation of metrological aspects. The efforts made in the MRT dosimetry project as part of the EMPIR programme try to establish a well defined metrology in nuclear medicine and molecular radiotherapy. The guidelines (Gear, et al., 2016) concerning uncertainties were consequently applied in this project and only slight changes to the formulae given in the paper were introduced to allow for the specific application.

Therefore this thesis does not only evaluate different measures like doses and activities, but also emphasizes metrological aspects. Thus an estimation of the quality of the results is achieved and the employed methods are reproducible and traceable.

The computation of the conversion factor and the calibration using the Jaszczak phantom allows tracing the measurement to the primary standard used for calibrating the ISOMED 2010, which was used in turn to define the necessary activity for the phantom measurement. Every step performed to compute activity and dose values is included in the uncertainty budget and all values can be found in the appendix.

The quantitative reconstruction allows assigning an activity concentration to every voxel and in a further step to calculate a dose for each voxel. This poses a huge advantage over more general dosimetric approaches like the partition model using pre-defined tumour and liver volumes. As a result it was possible in this thesis to perform dose evaluations based only on the information of the SPECT scan instead of relying heavily on pre-treatment calculations. The dose calculations performed for the body phantom illustrate that measured values can be obtained, which are in good agreement with the theoretical assumptions. The dosimetry performed using the patients' data also yields promising results for many cases and a deeper evaluation is mainly prohibited by the large uncertainty affecting the calculations based on the partition model.

If all necessary values for performing precise pre-treatment dose calculations were collected for a series of patients a detailed comparison with doses obtained by analyzing Y-90 SPECT scans could be made. For this project the missing measurement of tumour volumes is the main issue impeding an in-depth comparison.

Although these tumour volumes cannot be obtained in some cases without well defined tumour edges and although the partition model is mainly directed at doing dosimetry, when one large tumour is treated implementing dose calculations in the clinical routine could yield valuable results for later evaluations. This can be regarded as one practical example of the objectives of the MRT dosimetry project. If standardized dosimetry is combined with new approaches like post-treatment dose calculations relying on quantitative SPECT new insights could be gained.

The approaches for dose evaluation only using the Y-90 SPECT scan introduced in this thesis provide a metrologically sound method for post-treatment dose measurements in SIRT. Using and maybe refining the introduced techniques could provide much deeper insights into the Y-90 dose distribution than are available now, when only pre-treatment calculations are in common use. The effort made to avoid any arbitrary elements as much as possible and to provide a detailed estimation of the relevant uncertainties could help to advance this part of nuclear medicine in the direction the MRT dosimetry project is taking it.

Furthermore Hermes and other companies are developing Monte Carlo based dosimetry software. If a combination of Monte Carlo based image reconstruction and sophisticated dosimetry is available, precise dose values could be assigned to every voxel also including possible interactions and disregarding the current approach of local dose deposition. The three dimensional dose profiles would provide a new gold standard and yield even further information on the effectiveness of SIRT treatment.

With this future perspectives a re-evaluation of the formulae used for calculating the necessary activity and the applied dose before the treatment will be possible, combining them with actual post-treatment results. In this way SIRT treatment could become more effective and unnecessary damage due to excessive doses could be further avoided.

5 Bibliography

Allesio, Adam and Kinahan, Paul. 2006. PET Image Reconstruction. [book auth.] Robert E. Henkin. *Nuclear Medicine.* 2nd edition. Philadelphia, Edinburgh : Elsevier Mosby , 2006.

Allred, Jonathan, et al. 2018. The value of 99mTc-MAA SPECT/CT for lung shunt estimation in Y-90 radioembolization: a phantom and patient study. *EJNMMI Research.* 2018, 8:50.

Berger, M. J., et al. 2017. *NIST Standard Reference Database 124.* Data extracted from the ESTAR database, July 2017.

Bexelius, Tobias and Sohlberg, Antti O. 2018. Implementation of GPU accelerated SPECT reconstruction with Monte Carlo-based scatter correction. *Annals of Nuclear Medicine.* 2018, 32, pp. 337–347.

Bolch, Wesley E., et al. 2009. MIRD Pamphlet No. 21: A Generalized Schema for Radiopharmaceutical Dosimetry—Standardization of Nomenclature. *Journal of Nuclear Medicine.* 2009, 50, pp. 477–484.

Botta, Francesca, Ferrari, Mahila and Cremonesi, Marta. 2018. Clinical dosimetry with Tc-99m MAA for Y-90 SIRT: practical Methods and Results. *MRT Dosimetry - 2nd scientific workshop for stakeholders: Prague, Czech Republic, 26-27 September 2018.* [Online] 2018. [Cited: 15 November 2018.] http://mrtdosimetry-empir.eu/wp-content/uploads/2018/10/10_MRTdosimetryWorkshop_Botta_sm.pdf.

Browne, E. and Tuli, J. K. 2017. *Nuclear Data Sheets 145, 25.* Data extracted from the ENSDF database, version 2018-10-05, [IAEA Nuclear Data Section], 2017.

Browne, E. 1997. *Nuclear Data Sheets 82, 379.* Data extracted from the ENSDF database, version 2018-10-05, [IAEA Nuclear Data Section], 1997.

Buscombe, John and Navalkissoor, Shaunak. 2012. Molecular radiotherapy. *Clinical Medicine.* 2012, 12:4, pp. 381-386.

de Jong, Hugo W.A.M., Slijpen, Eddy T.P. and Beekman, Freek J. 2001. Acceleration of Monte Carlo SPECT Simulation using Convolution-Based Forced Detection. *IEEE Transactions on Nuclear Science.* 2001, 48:1, pp. 58-64.

Dieudonne, Arnaud, et al. 2016. Absorbed-dose calculation for treatment of liver neoplasms with Y-90 microspheres. *Clin. Transl. Imaging.* 2016, 4, pp. 273-282.

EN 61675-1. 2014. *Radionuclide imaging devices - Characteristics and test conditions - Part 1: Positron emission tomographs.* s.l. : European Committee for Electrotechnical Standardization , 2014.

Erlandsson, Kjell, et al. 2012. A review of partial volume correction techniques for emission tomography and their applications in neurology, cardiology and oncology. *Physics in Medicine and Biology.* 2012, 57, pp. 119-159.

Figl, Michael. 2014. CT Reconstruction. [book auth.] Wolfgang Birkfellner. *Applied Medical Image Processing - A Basic Course.* 2nd edition. Boca Raton, London, New York : CRC Press, 2014, pp. 339-369.

Gear, Jonathan I. 2018. Methods for determining uncertainty in clinical dose calculation: Practice. *MRT Dosimetry - 2nd scientific workshop for stakeholders: Prague, Czech Republic, 26-27 September 2018.* [Online] 2018. [Cited: 15 October 2018.] http://mrtdosimetry-empir.eu/wp-content/uploads/2018/10/03b_MRTdosimetryWorkshop_Gear_sm.pdf.

Gear, Jonathan I., et al. 2016. Abdo-Man: a 3D-printed anthropomorphic phantom for validating quantitative SIRT. *EJNMMI Physics.* 2016, 3:17.

Gear, Jonathan I., et al. 2018. EANM practical guidance on uncertainty analysis for molecular radiotherapy absorbed dose calculations. *European Journal of Nuclear Medicine and Molecular Imaging.* 2018.

Gemmell, Howard G. and Staff, Roger T. 2003. Single-photon emission-computed tomography (SPECT). [ed.] Peter F. Sharp, Howard G. Gemmell and Francis W. Smith. *Practical Nuclear Medicine.* 2nd edition. New York : Oxford University Press, 2003, pp. 13-24.

Hermes Medical Solutions. 2017. HybridRecon TM Oncology Handbook. 2.1 Stockholm, 3 November 2017.

Hsieh, Te-Chun, et al. 2016. Treating hepatocellular carcinoma with Y-90 bearing microspheres: a review. *BioMedicine.* 2016, 6:4, pp. 1-7.

Hudson, H. Malcolm and Larkin, Richard S. 1994. Accelerated Image Reconstruction using Ordered Subsets of Projection Data. *IEEE Transactions on Medical Imaging.* 1994, 13:4, pp. 601-609.

Hui, Wang, et al. 2018. alternative treatment strategies to sorafenib in patients with advanced hepatocellular carcinoma: a meta-analysis of randomized Phase iii trials. *OncoTargets and Therapy.* 2018, 11, pp. 5195–5201.

Kinahan, Paul E. and Fletcher, James W. 2010. PET/CT Standardized Uptake Values (SUVs) in Clinical Practice and Assessing Response to Therapy. *Seminars in Ultrasound, CT and MRI.* 2010, 31:6, pp. 496–505.

Kinahan, Paul E., Defrise, Michel and Clackdoyle, Rolf. 2004. Analytic Image Reconstruction Methods. [ed.] Miles N. Wernick and John N. Aarsvold. *Emission Tomography - The Fundamentals of PET and SPECT.* Amsterdam, Boston, Heidelberg : Elsevier Academic Press, 2004, pp. 421-442.

Lenoir, Laurence, et al. 2012. Usefulness and pitfalls of MAA SPECT/CT in identifying digestive extrahepatic uptake when planning liver radioembolization. *European Journal of Nuclear Medicine and Molecular Imaging.* 2012, 39, pp. 872–880.

Lichten, William. 1999. *Data and Error Analysis.* 2. New Jersey : Prentice-Hall, Inc., 1999.

MetroMRT. 2015. Final publishable JRP Report. *MetroMRT - Metrology for molecular radiation therapy.* [Online] 2015. [Cited: 26 October 2018.] http://projects.npl.co.uk/metromrt/news-events/metromrt-final-publishable-jrp-report-draft.pdf.

Mikell, Justin K., et al. 2015. Comparing voxel-based absorbed dosimetry methods in tumors, liver, lung, and at the liver-lung interface for 90Y microsphere selective internal radiation therapy. *EJNNMI Physiks.* 2015, 2:16.

MRT Dosimetry. 2017. Publishable Summary for 15HLT06 MRTDosimetry Metrology for clinical implementation of dosimetry in molecular radiotherapy. *MRT Dosimetry.* [Online] May 2017. [Cited: 26 October 2018.] http://mrtdosimetry-empir.eu/wp-content/uploads/downloads/2017/05/MRTDosimetry-Publishable-Summary.pdf.

Pardo, Fernando, et al. 2017. The Post-SIR-Spheres Surgery Study (P4S): Retrospective Analysis of Safety Following Hepatic Resection or Transplantation in Patients Previously Treated with Selective Internal Radiation Therapy with Yttrium-90 Resin Microspheres. *Annals of Surgical Oncology.* 2017, 24, pp. 2465–2473.

Patton, James A. and Turkington, Timothy G. 2008. SPECT/CT Physical Principles and Attenuation Correction. *J. Nucl. Med. Technol.* 2008, 36, pp. 1-10.

Porter, Charlotte A., et al. 2018. Phantom and clinical evaluation of the effect of full Monte Carlo collimator modelling in post-SIRT yttrium-90 Bremsstrahlung SPECT imaging. *EJNMMI Research.* 2018, 8:7.

Robinson, Andrew. 2018. Introduction to MRTDosimetry project. *MRT Dosimetry - 2nd scientific workshop for stakeholders: Prague, Czech Republic, 26-27 September 2018.* [Online] 2018. [Cited: 25 October 2018.] http://mrtdosimetry-empir.eu/wp-content/uploads/2018/10/01_MRTdosimetryWorkshop_Robinson_sm.pdf.

Shcherbinin, S., et al. 2008. Accuracy of quantitative reconstruction in SPET/CT imaging. *Phys. Med. Biol.* 2008, 53, pp. 4595-4604.

Simon, Norman, et al. 1968. Intra-arterial irradiation of carcinoid tumors of the liver. *American Journal of Roentgenology.* 1968, 102:3, pp. 552-561.

Sirtex Medical Limited. 2016. SIR-Spheres® Microspheres - package insert. [Online] May 2016. [Cited: 02 August 2018.] https://www.sirtex.com/media/155127/pi-ec-12.pdf.

Sohlberg, Antti O. and Kajaste, Markus T. 2011. Fast Monte Carlo-simulator with full collimator and detector modelling for SPECT. *Ann. Nucl. Med.* 2011, 26, pp. 92-98.

Sohlberg, Antti, Watabe, H. and Iida, H. 2008. Acceleration of Monte Carlo-based scatter compensation for cardiac SPECT. *Physics in Medicine and Biology.* 2008, 53, pp. 277–285 .

Spahr, Nadine, et al. 2017. Predictive SIRT dosimetry based on a territorial model. *EJNMMI Physics.* 2017, 4:25.

Stabin, Michael G. and da Luz, Lydia C.Q.P. 2003. Decay data for internal and external dose assessment. *RADAR - the RAdiation Dose Assessment Resource.* [Online] March 2003. [Cited: 5 December 2018.] https://www.doseinfo-radar.com/RADARDecay.html.

The international Commission on Radiation Units and Measurements. 2011. ICRU REPORT No. 85 - FUNDAMENTAL QUANTITIES AND UNITS FOR IONIZING RADIATION (Revised). *Journal of the ICRU.* 2011, 11:1.

The MathWorks, Inc. 2017. *MATLAB R2017b (9.3.0.713579).* 14 September 2017.

Voutsinas, Nicholas, et al. 2018. Treatment of Primary Liver Tumors and Liver Metastases, Part 1: Nuclear Medicine Techniques. *Journal of Nuclear Medicine.* 2018, 59, pp. 1649–1654.

Wang, Eric A., et al. 2017. Treatment options for unresectable HCC with a focus on SIRT with Yttrium-90 resin microspheres. *Int J Clin Pract.* 2017, 71:11.

Wasan, Harpreet S., et al. 2017. First-line selective internal radiotherapy plus chemotherapy versus chemotherapy alone in patients with liver metastases from colorectal cancer (FOXFIRE, SIRFLOX, and FOXFIRE-Global): a combined analysis of three multicentre, randomised, phase 3 trials. *Lancet Oncol.* 2017, 18, pp. 1159–1171.

Westcott, Mark A., et al. 2016. The development, commercialization, and clinical context of yttrium-90 radiolabeled resin and glass microspheres. *Advances in Radiation Oncology.* 2016, 1, pp. 351-364.

Zeng, Gengsheng Lawrence, et al. 2004. Single-Photon Emission Computed Tomography. [ed.] Miles N. Wernick and John N. Aarsvold. *Emission Tomography - The Fundamentals of PET and SPECT.* Amsterdam, Boston, Heidelberg : Elsevier Academic Press, 2004, pp. 127-152.

6 List of Figures

If not stated otherwise all figures were created by the author using HybridRecon, Hybrid Viewer and gnuplot version 5.2.4 by Williams, et al. (2018).

7 List of Tables

All tables were created by the author.

Appendix A Summary of Results

A.1 Count Rate Uncertainty

Uncertainty of the count rate in a Jaszczak phantom, not quantitative reconstruction and evaluation with ROIs with 5 cm diameter conversion to cps with $count\ rate(cps) = (total(a.u.)/\#\ cells) \cdot t_{acquisition}\ (s)\ \#frames$

									acquisition time (s)		**25**
									number of frames		**64**
	cells	**total (a.u.)**	**mean (a.u.)**	**min (a.u.)**	**max (a.u.)**	**area (cm²)**	**count rate (cps)**	$(\bar{x} - x_i)^2$	**count rate/ area (a.u.)**	**count rate/area (cps/cm^2)**	$(\bar{x} - x_i)^2$
Roi 1	85,00	1334,32	15,70	12,38	18,83	19,54	0,8340	7,61E-06	68,30	0,0427	1,69E-07
Roi 2	84,00	1284,56	15,29	11,50	17,56	19,31	0,8029	1,15E-03	66,51	0,0416	2,33E-06
Roi 3	84,00	1259,28	14,99	11,70	17,65	19,31	0,7871	2,47E-03	65,21	0,0408	5,48E-06
Roi 4	84,00	1221,80	14,55	10,83	17,10	19,31	0,7636	5,34E-03	63,29	0,0396	1,25E-05
Roi 5	84,00	1169,06	13,92	10,04	16,31	19,31	0,7307	1,12E-02	60,55	0,0378	2,76E-05
Roi 6	84,00	1149,35	13,68	9,88	16,61	19,31	0,7183	1,40E-02	59,51	0,0372	3,48E-05
Roi 7	84,00	1206,00	14,36	11,47	17,10	19,31	0,7538	6,88E-03	62,47	0,0390	1,64E-05
Roi 8	84,00	1315,35	15,66	11,25	19,00	19,31	0,8221	2,14E-04	68,12	0,0426	2,70E-07
Roi 9	84,00	1408,82	16,77	11,17	20,94	19,31	0,8805	1,92E-03	72,95	0,0456	6,24E-06
Roi 10	84,00	1451,76	17,28	12,75	22,44	19,31	0,9074	4,99E-03	75,17	0,0470	1,51E-05
Roi 11	84,00	1458,53	17,36	12,57	22,93	19,31	0,9116	5,61E-03	75,52	0,0472	1,68E-05
Roi 12	84,00	1459,37	17,37	12,76	21,99	19,31	0,9121	5,68E-03	75,56	0,0472	1,71E-05
Roi 13	84,00	1487,36	17,71	13,62	21,53	19,31	0,9296	8,63E-03	77,04	0,0481	2,55E-05
Roi 14	84,00	1493,27	17,78	14,60	22,94	19,31	0,9333	9,33E-03	77,34	0,0483	2,75E-05
Roi 15	84,00	1482,72	17,65	13,88	23,17	19,31	0,9267	8,10E-03	76,78	0,0480	2,39E-05

Roi 16	84,00	1423,67	16,95	12,87	22,22	19,31	0,8898	2,82E-03	73,73	0,0461	8,93E-06
Roi 17	84,00	1389,10	16,54	12,71	21,28	19,31	0,8682	9,91E-04	71,95	0,0450	3,51E-06
Roi 18	84,00	1412,00	16,81	12,95	22,87	19,31	0,8825	2,10E-03	73,12	0,0457	6,80E-06
Roi 19	84,00	1433,82	17,07	13,33	23,37	19,31	0,8961	3,53E-03	74,26	0,0464	1,10E-05
Roi 20	84,00	1395,32	16,61	13,36	21,38	19,31	0,8721	1,25E-03	72,25	0,0452	4,26E-06
Roi 21	84,00	1305,40	15,54	12,35	19,35	19,31	0,8159	4,34E-04	67,60	0,0423	7,15E-07
Roi 22	84,00	1223,39	14,56	11,22	20,11	19,31	0,7646	5,20E-03	63,34	0,0396	1,23E-05
Roi 23	85,00	1185,42	13,95	10,96	19,24	19,54	0,7409	9,18E-03	60,68	0,0379	2,67E-05
Roi 24	85,00	1263,77	14,87	12,01	18,58	19,54	0,7899	2,20E-03	64,69	0,0404	7,11E-06
Roi 25	85,00	1356,09	15,95	12,99	19,62	19,54	0,8476	1,18E-04	69,38	0,0434	7,23E-08
Roi 26	85,00	1378,69	16,22	13,07	20,03	19,54	0,8617	6,24E-04	70,56	0,0441	1,01E-06
Roi 27	87,00	1345,83	15,47	11,49	18,61	20,00	0,8411	1,97E-05	67,29	0,0421	1,07E-06
Roi 28	87,00	1287,79	14,80	12,26	16,72	20,00	0,8049	1,01E-03	64,38	0,0402	8,17E-06
Roi 29	87,00	1241,44	14,27	11,64	16,83	20,00	0,7759	3,70E-03	62,07	0,0388	1,85E-05
mean							**0,8367**			**0,0431**	
absolute uncertainty (cps)								**0,0651**			**0,0036**
relative uncertainty (%)								**7,78 %**			**8,26 %**

A.2 Phantom Activity Measurement

A parameterized recovery coefficient was calculated using a nonlinear least-squares Marquardt-Levenberg algorithm and $f(x) = a \cdot e^{bV} + c$ the resulting parameters and their covariance matrix are given below

parameter	value	abs. uncert.	rel uncert. (%)	covariance matrix		
a	-0,2451	0,0213	8,68%	4,530E-04	4,915E-04	-9,176E-05
b	-0,2996	0,0693	23,12%	4,915E-04	4,802E-03	5,760E-04
c	0,2073	0,0130	6,26%	-9,176E-05	5,760E-04	1,686E-04

NEMA IEC Body phantom quantitative reconstruction, evaluation with VOIs corresponding to the real inlays, uncertainties calculated in MATLAB according to the uncertainty budget given in section 3.2, results with and without recovery factor

inlay d (mm)	mean A_{Conc} (Bq/mL)	min A_{Conc} (Bq/mL)	max A_{Conc} (Bq/mL)	volume (mL)	applied A (MBq)	activity (MBq)	recovery coefficient	A_{Corr} (MBq)	abs. uncert. (MBq)	relative uncert. (%)
37	1955124,75	749596,88	3569690,50	26,02	257,84	50,88	0,21	245,77	59,15	24,09
28	2004554,50	1057390,62	3788684,50	11,47	111,74	22,99	0,20	115,51	27,42	23,80
22	1651395,12	896729,69	2971967,25	5,73	54,20	9,47	0,16	58,81	14,36	24,44
17	874119,75	590207,81	1173131,25	2,43	25,01	2,12	0,09	22,56	6,55	29,00
13	285725,91	262642,19	320975,00	0,77	11,18	0,22	0,03	6,49	5,13	78,31
10	171722,39	162626,56	179565,62	0,33	5,09	0,06	0,00	-28,40	-467,71	1792,11

Jaszczak phantom quantitative reconstruction, evaluation with VOIs with different thresholds (percent of maximum concentration value), uncertainties calculated in MATLAB according to the uncertainty budget given in section 3.2, comparison with real values

	cells	mean A_{Conc} (Bq/mL)	min A_{Conc} (Bq/mL)	max A_{Conc} (Bq/mL)	threshold % of max.	volume (mL)	activity (MBq)	abs. uncert. (MBq)	relative uncert. (%)
Voi 11	39617,00	85045,82	50817,25	127135,28	60,00	4368,19	371,50	87,14	23,46
Voi 10	46625,00	82249,96	50817,25	127135,28	55,00	5140,90	422,84	99,10	23,44
Voi 9	54610,00	80811,70	49011,15	127135,28	50,00	6021,33	486,59	113,97	23,42
Voi 8	58596,00	79381,77	45994,51	127135,28	45,00	6460,83	512,87	120,09	23,42
Voi 7	62461,00	77789,41	38737,12	127135,28	40,00	6886,98	535,73	125,41	23,41
Voi 6	66744,00	75840,25	35881,50	127135,28	35,00	7359,23	558,13	130,62	23,40
Voi 1	71615,00	73468,38	24961,46	127135,28	30,00	7896,31	580,13	135,74	23,40
Voi 2	78402,00	70094,52	22573,38	127135,28	25,00	8644,65	605,94	141,73	23,39
Voi 3	89911,00	64717,02	18353,96	127135,28	20,00	9913,64	641,58	150,01	23,38
Voi 4	98080,00	61339,91	17100,75	127135,28	18,00	10814,36	663,35	155,06	23,38
Voi 5	109786,00	57099,95	14505,08	127135,28	16,00	12105,07	691,20	161,52	23,37
real values		**81826,09**				**6900,00**	**564,60**	**112,92**	**20,00**

A.3 Calculation of Best Threshold Value

Threshold value for constructing a VOI yielding the most precise total activity, best threshold as % of maximum concentration value calculated using a nonlinear least-squares Marquardt-Levenberg algorithm and $A = a + b \cdot A_{Threshold}^{c}$

Patient	applied A (MBq)	a	b	c	threshold % of max.	$(\overline{x} - x_i)^2$
BM	1790,00	-2265,08	1751,55	-0,2919	4,6200	3,3094
DB	1650,00	-2843,98	3133,14	-0,1872	5,0600	1,9021
EE	1120,00	-452,68	530,36	-0,4022	4,9400	2,2475
ER	1840,00	-2885,47	4997,75	-1,0658	49,2500	NaN
KK	1740,00	-4452,99	5271,17	-0,7961	36,0600	NaN
MH	1340,00	-5033,72	4718,41	-0,1769	13,1900	45,5738
MK	2700,00	-129,60	172,41	-1,7123	14,2800	NaN
OH	1770,00	-116,08	784,64	-0,4821	6,0800	0,1290
RL	1830,00	450,30	226,62	-0,7515	9,3000	8,1844
SE	1290,00	-3842,45	3680,40	-0,1277	5,0300	1,9858
SF	1620,00	-531,53	2094,77	-1,8112	33,1200	NaN
Sjo	1940,00	-2185,91	2360,99	-0,2564	6,1900	0,0621
Sju	1690,00	-319,73	1094,55	-0,3960	6,5200	0,0065
SM	2770,00	37,96	610,04	-0,5639	7,3400	0,8115
WC	1706,00	-1230,59	1343,53	-0,2998	3,0900	11,2169
WH	580,00	-152,11	41,83	-2,0686	46,0900	NaN
ZP	2150,00	-31,63	579,30	-0,5692	5,9100	0,2800
mean					**6,4392**	
absolute uncertainty						**0,7939**
relative uncertainty						**12,33 %**

A.4 Patient Dataset Evaluation of Total Activity

Evaluation of the dataset using VOIs constructed with different thresholds, results for total activity and VOI volume for all patients, uncertainties calculated in MATLAB according to the uncertainty budget given in section 3.2

VOI 1 threshold criteria: 20 % of maximum activity concentration value

patient	mean A_{Conc} (Bq/mL)	min A_{Conc} (Bq/mL)	max A_{Conc} (Bq/mL)	mean SUV	activity (MBq)	abs. uncert. (MBq)	relative uncert. (%)	volume (mL)	abs. uncert. (mL)	relative uncert. (%)
BM	379843,59	233928,31	1220386,25	25,76	526,91	150,39	28,54	1387,19	58,44	0,04
DB	928376,19	553754,69	2878312,25	38,61	655,74	191,27	29,17	706,33	37,27	0,05
EE	464985,44	219068,41	1355807,75	37,69	460,09	132,66	28,83	989,48	46,66	0,05
ER	655420,38	267534,34	2140242,00	22,80	12717,98	3457,90	27,19	19404,31	339,30	0,02
KK	655332,75	358247,25	2264660,25	29,42	7138,52	1954,72	27,38	10892,97	230,90	0,02
MH	403084,31	232025,48	1366444,12	17,78	1443,11	402,56	27,90	3580,16	109,96	0,03
MK	447994,62	264177,72	1385252,62	16,76	861,91	243,84	28,29	1923,94	72,69	0,04
OH	995157,19	533008,00	2664836,50	50,45	972,07	280,40	28,85	976,80	46,26	0,05
RL	426008,00	194412,20	972061,00	15,48	1228,78	344,34	28,02	2884,42	95,21	0,03
SE	428386,84	294741,97	1476300,38	22,08	637,76	181,66	28,48	1488,74	61,26	0,04
SF	853804,19	556522,62	2983081,50	41,73	4822,65	1333,91	27,66	5648,43	149,03	0,03
Sjo	640437,88	365998,72	1830831,62	24,39	1326,79	374,67	28,24	2071,69	76,36	0,04
Sju	1084473,62	660933,50	3304112,75	30,48	1044,13	301,33	28,86	962,80	45,82	0,05
SM	387787,56	190882,48	954412,44	14,04	1587,64	441,71	27,82	4094,08	120,25	0,03
WC	697466,38	440379,00	2382780,50	32,37	699,51	201,61	28,82	1002,93	47,08	0,05
WH	169032,06	61217,41	545834,44	28,61	4412,78	1196,06	27,10	26106,17	413,51	0,02
ZP	611033,38	319090,75	1646324,38	21,30	1058,70	300,33	28,37	1732,63	67,78	0,04

VOI 2 threshold criteria: constant SUV value of 4.0

patient	mean A_{Conc} (Bq/mL)	min A_{Conc} (Bq/mL)	max A_{Conc} (Bq/mL)	mean SUV	activity (MBq)	abs. uncert. (MBq)	relative uncert. (%)	volume (mL)	abs. uncert. (mL)	relative uncert. (%)
BM	134222,34	49981,18	1220386,25	9,10	1615,49	441,78	27,35	12035,93	0,00	0,02
DB	266457,88	75983,16	2878312,25	11,08	1949,82	537,02	27,54	7317,55	0,00	0,02
EE	118029,59	22405,43	1355807,75	9,57	1429,76	390,95	27,34	12113,55	0,00	0,02
ER	356663,03	56204,42	2140242,00	12,41	23993,81	6451,30	26,89	67273,05	104,65	0,01
KK	302416,41	43748,53	2264660,25	13,58	18644,53	5016,21	26,90	61651,85	39,42	0,01
MH	178067,27	41159,09	1366444,12	7,86	8480,86	2286,28	26,96	47627,27	61,62	0,01
MK	228621,52	86325,96	1385252,62	8,55	1945,52	534,61	27,48	8509,80	576,21	0,02
OH	197419,14	30415,77	2664836,50	10,01	2843,91	775,93	27,28	14405,43	310,48	0,02
RL	278184,22	92303,89	972061,00	5,04	1648,91	455,70	27,64	5927,39	293,69	0,03
SE	190856,33	65192,85	1476300,38	9,84	1184,42	327,08	27,62	6205,79	415,25	0,03
SF	329947,38	18025,76	2983081,50	16,12	23188,11	6232,73	26,88	70278,20	52,91	0,01
Sjo	237394,08	30506,88	1830831,62	9,04	2226,86	611,05	27,44	9380,42	185,32	0,02
Sju	430930,00	124381,95	3304112,75	12,11	1955,27	542,94	27,77	4537,33	68,95	0,03
SM	266410,44	90569,78	954412,44	9,64	2145,49	590,04	27,50	8053,32	1340,47	0,02
WC	209534,97	60319,41	2382780,50	9,72	1578,29	434,50	27,53	7532,34	37,22	0,02
WH	93610,89	4722,49	545834,44	15,84	7521,22	2019,76	26,85	80345,54	57,11	0,01
ZP	273710,53	88879,16	1646324,38	9,54	2088,99	574,98	27,52	7632,12	53,81	0,02

VOI 3 threshold criteria: calculated best value, 6.4 % of maximum activity concentration value

patient	mean A_{Conc} (Bq/mL)	min A_{Conc} (Bq/mL)	max A_{Conc} (Bq/mL)	mean SUV	activity (MBq)	abs. uncert. (MBq)	relative uncert. (%)	volume (mL)	abs. uncert. (mL)	relative uncert. (%)
BM	164284,38	59627,32	1220386,25	/	1415,45	388,59	27,45	9058,30	204,18	0,02
DB	441146,69	166635,89	2878312,25	/	1451,50	405,55	27,94	3314,62	104,46	0,03
EE	196123,77	57927,24	1355807,75	/	961,25	266,69	27,74	4753,35	132,84	0,03
ER	688467,62	345031,78	2140242,00	/	38430,35	10420,69	27,12	25036,28	402,13	0,02
KK	675918,25	358247,25	2264660,25	/	19958,08	5438,12	27,25	16077,70	299,32	0,02
MH	251987,86	121413,05	1366444,12	/	2201,74	602,59	27,37	11311,81	236,78	0,02
MK	186630,27	66308,65	1385252,62	/	10936,97	2979,72	27,24	16240,32	301,33	0,02
OH	442565,94	150249,05	2664836,50	/	1719,12	477,15	27,76	4646,50	130,84	0,03
RL	157694,34	34960,68	972061,00	/	2268,56	623,59	27,49	8317,88	192,90	0,02
SE	215754,33	82358,34	1476300,38	/	1130,20	317,94	28,13	2429,47	84,92	0,03
SF	853804,19	556522,62	2983081,50	/	38406,68	10338,92	26,92	57182,53	697,42	0,01
Sjo	271001,97	86408,21	1830831,62	/	1898,46	540,13	28,45	1552,94	63,01	0,04
Sju	587974,31	195118,83	3304112,75	/	1700,28	470,89	27,70	5244,41	141,83	0,03
SM	153298,27	39685,27	954412,44	/	2978,85	839,47	28,18	2254,68	80,79	0,04
WC	336718,06	134818,80	2382780,50	/	1125,89	316,74	28,13	2424,28	84,80	0,03
WH	228730,94	128156,78	545834,44	/	31777,94	8595,33	27,05	32411,92	477,66	0,01
ZP	240018,31	64235,16	1646324,38	/	2046,54	566,40	27,68	5458,16	145,66	0,03

A.5 Patient Dataset Activity Concentration

Comparison of activity concentration calculated using values for applied activity and real liver volume and concentrations measured in VOIs corresponding to the liver volume, difference between the values expressed as recovery coefficient, uncertainties calculated in MATLAB according to the uncertainty budget given in section 3.2

patient	applied A (MBq)	V_{Liver} (mL)	calc. A_{Conc} (MBq/mL)	meas. A_{Conc} (MBq/mL)	abs. uncert. (MBq/mL)	relative uncert. (%)	recovery coefficient
BM	1790	1989	0,8999	0,3330	0,0780	23,48	0,37
DB	1650	1846	0,8938	0,6110	0,1430	23,48	0,68
EE	1120	1670	0,6707	0,3650	0,0860	23,48	0,54
ER	1840	NaN	NaN	NaN	NaN	NaN	NaN
KK	1740	2510	0,6932	0,9360	0,2200	23,48	1,35
MH	1340	1240	1,0806	0,5770	0,1360	23,48	0,53
MK	2370	2413	0,9822	0,4520	0,1060	23,48	0,46
OH	1770	1083	1,6343	0,9480	0,2230	23,48	0,58
RL	1830	1395	1,3118	0,5060	0,1190	23,48	0,39
SE	1290	1937	0,6660	0,3500	0,0820	23,48	0,53
SF	1620	1734	0,9343	1,1900	0,2790	23,48	1,27
Sjo	1940	2175	0,8920	0,5180	0,1220	23,48	0,58
Sju	1690	1028	1,6440	1,0560	0,2480	23,48	0,64
SM	2770	2310	1,1991	0,4640	0,1090	23,48	0,39
WC	1706	1753	0,9732	0,4780	0,1120	23,48	0,49
WH	580	3009	0,1928	0,2860	0,0670	23,48	1,48
ZP	2150	1476	1,4566	0,6530	0,1530	23,48	0,45

A.6 Phantom Dose Measurement

Dose calculated from phantom specifications and applied activity, uncertainty calculated as given in section 3.8.3

inlay d (mm)	volume (mL)	m (kg)	applied A (GBq)	$A_{0\setminus i}/A_i$.	D (Gy)	absolute uncert. (Gy)	relative uncert. (%)
3,70	26,52	0,0276	0,2578	0,80	464,30	105,03	22,62
2,80	11,49	0,0120	0,1117	3,16	464,30	104,38	22,48
2,20	5,58	0,0058	0,0542	7,58	464,30	104,27	22,46
1,70	2,57	0,0027	0,0250	17,60	464,30	104,24	22,45
1,30	1,15	0,0012	0,0112	40,59	464,30	104,24	22,45
1,00	0,52	0,0005	0,0051	90,36	464,30	104,24	22,45
cold area	9652,16	10,0382	0,00	NaN	0,00	0,00	0,00
total	9700,00	10,0880	0,4651				

Dose values measured in the activity concentration distribution analyzed in MATLAB, uncertainties calculated in MATLAB according to the uncertainty budget given in section 3.2, no recovery factor applied

inlay d (mm)	max. D (Gy)	absolute uncert. (Gy)	relative uncert. (%)	mean D (Gy)	absolute uncert. (Gy)	relative uncert. (%)
3,70	176,08	41,51	23,57	155,93	36,76	23,57
2,80	170,51	40,19	23,57	150,60	35,50	23,57
2,20	148,63	35,04	23,57	140,12	33,03	23,57
1,70	76,28	17,98	23,57	73,49	17,32	23,57
1,30	34,33	8,09	23,57	30,65	7,23	23,57
1,00						
cold area				29,74	7,01	23,57

Dose values measured in the activity concentration distribution analyzed in MATLAB, uncertainties calculated in MATLAB according to the uncertainty budget given in section 3.2, spill-out correction with recovery factor

inlay d (mm)	recovery coefficient	max. D (Gy)	absolute uncert. (Gy)	relative uncert. (%)	mean D (Gy)	absolute uncert. (Gy)	relative uncert. (%)
3,70	0,21	631,62	153,98	24,38	572,98	139,69	24,38
2,80	0,20	550,78	132,62	24,08	490,40	118,08	24,08
2,20	0,16	474,62	117,08	24,67	430,55	106,21	24,67
1,70	0,09	387,69	112,77	29,09	351,77	102,32	29,09
1,30	0,03	365,91	286,44	78,28	329,40	257,86	78,28

A.7 Patient Dataset Dose Evaluation

Calculation of the dose for a hypothetical homogeneous activity distribution in the liver, uncertainties calculated according to the budget given in section 3.8.3

patient	weight (kg)	height (m)	applied A (GBq)	V_{Liver} (mL)	D (Gy)	absolute uncert. (Gy)	relative uncert. (%)
BM	115,00	169,00	1,79	1989,00	42,98	4,81	0,11
DB	65,00	157,00	1,65	1846,00	42,69	4,77	0,11
EE	86,00	174,00	1,12	1670,00	32,03	3,58	0,11
MH	56,00	169,00	1,84	1240,00	70,87	7,92	0,11
MK	85,00	174,00	1,74	2413,00	34,44	3,85	0,11
OH	70,00	180,00	1,34	1083,00	59,09	6,61	0,11
RL	63,00	165,00	2,37	1395,00	81,14	9,07	0,11
SE	63,00	160,00	1,77	1937,00	43,64	4,88	0,11
Sjo	70,00	174,00	1,83	2175,00	40,18	4,49	0,11
Sju	45,00	168,00	1,29	1028,00	59,93	6,70	0,11
SM	95,00	174,00	1,62	2310,00	33,49	3,74	0,11
WC	75,00	165,00	1,94	1753,00	52,85	5,91	0,11
ZP	71,00	172,00	1,69	1476,00	54,68	6,11	0,11

Doses to tumour and healthy liver tissue calculated using the tumour volumes estimated from the BSA model and uncertainties calculated according to the budget given in section 3.8.3

patient	A_T/A_{Liver}	BSA (m^2)	m_{Tumour} (kg)	m_{NT} (kg)	D_T (Gy)	absolute uncert. (Gy)	relative uncert. (%)	D_{NT} (Gy)	absolute uncert. (Gy)	relative uncert. (%)
BM	0,50	2,23	NaN	NaN	NaN	NaN	NaN	NaN	NaN	NaN
DB	68,00	1,66	0,37	1,55	216,07	54,02	0,25	0,77	0,19	0,25
EE	1,18	2,01	NaN	NaN	NaN	NaN	NaN	NaN	NaN	NaN
MH	0,93	1,64	497,34	497,34	497,34	497,34	497,34	497,34	497,34	497,34
MK	1,25	2,00	NaN	NaN	NaN	NaN	NaN	NaN	NaN	NaN
OH	8,12	1,89	NaN	NaN	NaN	NaN	NaN	NaN	NaN	NaN
RL	1,52	1,69	1,27	0,18	55,83	13,98	0,25	260,95	65,44	0,25
SE	1,00	1,66	608,17	608,17	608,17	608,17	608,17	608,17	608,17	608,17
Sjo	3,61	1,84	0,43	1,83	166,02	41,51	0,25	10,76	2,69	0,25
Sju	0,59	1,49	0,00	1,07	7535,61	1926,24	0,26	37,80	9,53	0,25
SM	0,26	2,10	NaN	NaN	NaN	NaN	NaN	NaN	NaN	NaN
WC	0,51	1,82	0,58	1,25	56,43	14,57	0,26	51,20	12,91	0,25
ZP	0,89	1,84	0,08	1,45	478,02	120,35	0,25	30,58	7,69	0,25

Doses to tumour and healthy liver tissue calculated using tumour volumes estimated by drawing VOIs with threshold criteria also given in the table, uncertainties calculated according to the budget given in section 3.8.3

patient	V_{Tumour} meas. (mL)	threshold % of max.	m_{Tumour} (kg)	m_{NT} (kg)	D_T (Gy)	absolute uncert. (Gy)	relative uncert. (%)	D_{NT} (Gy)	absolute uncert. (Gy)	relative uncert. (%)
BM	508,74	32,00	0,53	1,54	56,01	14,49	0,26	38,50	9,71	0,25
DB	273,78	32,00	0,28	1,64	283,66	70,92	0,25	0,73	0,18	0,25
EE	437,84	32,00	0,46	1,28	66,13	16,58	0,25	19,91	5,00	0,25

MH	564,97	40,00	0,59	0,70	74,95	18,85	0,25	67,45	16,95	0,25
MK	721,22	32,00	0,75	1,76	64,01	16,04	0,25	21,83	5,48	0,25
OH	534,32	32,00	0,56	0,57	106,64	26,66	0,25	12,79	3,20	0,25
RL	637,85	60,00	0,66	0,79	107,04	26,80	0,25	59,32	14,88	0,25
SE	242,68	32,00	0,25	1,76	174,17	43,76	0,25	24,95	6,27	0,25
Sjo	580,30	32,00	0,60	1,66	117,94	29,49	0,25	11,89	2,97	0,25
Sju	181,49	40,00	0,19	0,88	125,97	32,20	0,26	45,77	11,53	0,25
SM	453,38	60,00	0,47	1,93	35,21	10,31	0,29	33,07	8,37	0,25
WC	193,29	32,00	0,20	1,62	161,90	41,82	0,26	39,34	9,92	0,25
ZP	600,92	40,00	0,62	0,91	63,25	15,92	0,25	48,80	12,27	0,25

Doses to tumours calculated from activity concentration measured using the VOIs defined above, mean and maximum values given, uncertainties calculated in MATLAB according to the uncertainty budget given in section 3.2

patient	**max A_{Conc} (Bq/mL)**	**max. D_T (Gy)**	**absolute uncert. (Gy)**	**relative uncert. (%)**	**mean A_{Conc} (Bq/mL)**	**mean D_T (Gy)**	**absolute uncert. (Gy)**	**relative uncert. (%)**
BM	1220386,25	58,29	13,74	23,57	529532,66	25,29	5,96	23,57
DB	2878312,25	137,47	32,41	23,57	1127183,93	53,83	12,69	23,57
EE	1355807,75	64,75	15,26	23,57	625888,75	29,89	7,05	23,57
MH	1366444,12	65,26	15,38	23,57	512732,55	24,49	5,77	23,57
MK	1385252,62	66,16	15,60	23,57	571005,96	27,27	6,43	23,57
OH	2664836,50	127,27	30,00	23,57	1097474,78	52,42	12,36	23,57
RL	972061,00	46,43	10,94	23,57	662002,91	31,62	7,45	23,57
SE	1476300,38	70,51	16,62	23,57	564791,66	26,97	6,36	23,57
Sjo	1830831,62	87,44	20,61	23,57	825143,56	39,41	9,29	23,57
Sju	3304112,75	157,80	37,20	23,57	1380891,38	65,95	15,55	23,57

SM	954412,44	45,58	10,75	23,57	639014,48	30,52	7,19	23,57
WC	2382780,50	113,80	26,83	23,57	909908,06	43,46	10,24	23,57
ZP	1646324,38	78,63	18,54	23,57	665929,63	31,81	7,50	23,57

Doses to healthy liver tissue calculated from activity concentration measured using VOIs corresponding to the real liver volume, excluding the tumour region, mean and minimum values given, uncertainties calculated in MATLAB according to the uncertainty budget given in section 3.2

patient	mean A_{Conc} (Bq/mL)	mean. D_{NT} (Gy)	absolute uncert. (Gy)	relative uncert. (%)	min. A_{Conc} (Bq/mL)	min. D_{NT} (Gy)	absolute uncert. (Gy)	relative uncert. (%)
BM	367134,22	17,53	4,13	23,57	204735,79	9,78	2,31	23,57
DB	709527,54	33,89	7,99	23,57	291871,15	13,94	3,29	23,57
EE	396047,63	18,92	4,46	23,57	166206,51	7,94	1,87	23,57
MH	444017,29	21,21	5,00	23,57	375302,04	17,92	4,23	23,57
MK	439221,90	20,98	4,95	23,57	307437,84	14,68	3,46	23,57
OH	795292,80	37,98	8,95	23,57	493110,82	23,55	5,55	23,57
RL	426205,71	20,36	4,80	23,57	190408,52	9,09	2,14	23,57
SE	377500,52	18,03	4,25	23,57	190209,39	9,08	2,14	23,57
Sjo	541179,99	25,85	6,09	23,57	257216,43	12,29	2,90	23,57
Sju	998567,43	47,69	11,24	23,57	616243,49	29,43	6,94	23,57
SM	422794,07	20,19	4,76	23,57	206573,67	9,87	2,33	23,57
WC	572563,60	27,35	6,45	23,57	235219,14	11,23	2,65	23,57
ZP	507237,12	24,23	5,71	23,57	348544,62	16,65	3,92	23,57

Mean dose values measured in the activity concentration distribution analyzed in MATLAB, uncertainties calculated in MATLAB according to the uncertainty budget given in section 3.2, no recovery factor applied

patient	mean D_T (Gy)	absolute uncert. (Gy)	relative uncert. (%)	mean D_{NT} (Gy)	absolute uncert. (Gy)	relative uncert. (%)
BM	42,76	10,08	23,57	14,97	3,53	23,57
DB	104,95	24,74	23,57	37,98	8,95	23,57
EE	56,35	13,28	23,57	17,81	4,20	23,57
MH	57,29	13,51	23,57	20,41	4,81	23,57
MK	47,60	11,22	23,57	14,18	3,34	23,57
OH	111,16	26,20	23,57	40,29	9,50	23,57
RL	40,39	9,52	23,57	14,00	3,30	23,57
SE	60,60	14,29	23,57	19,44	4,58	23,57
Sjo	75,49	17,80	23,57	21,48	5,06	23,57
Sju	135,72	31,99	23,57	47,51	11,20	23,57
SM	37,26	8,78	23,57	13,80	3,25	23,57
WC	84,55	19,93	23,57	23,18	5,47	23,57
ZP	67,66	15,95	23,57	23,55	5,55	23,57

Dose values measured in the activity concentration distribution analyzed in MATLAB, mean and maximum values given, uncertainties calculated in MATLAB according to the uncertainty budget given in section 3.2, spill-out correction with recovery factor

patient	recovery coefficient	max. D_T (Gy)	absolute uncert. (Gy)	relative uncert. (%)	mean D_T (Gy)	absolute uncert. (Gy)	relative uncert. (%)	mean D_{NT} (Gy)	absolute uncert. (Gy)	relative uncert. (%)
BM	0,37	150,10	38,43	25,61	107,58	27,55	25,61	35,18	9,01	25,61
DB	0,68	179,85	46,05	25,61	153,61	39,34	25,61	55,59	14,24	25,61
EE	0,54	118,30	30,29	25,61	103,56	26,52	25,61	32,72	8,38	25,61
MH	0,53	121,62	31,14	25,61	107,28	27,47	25,61	38,21	9,79	25,61
MK	0,46	117,96	30,21	25,61	103,41	26,48	25,61	30,80	7,89	25,61
OH	0,58	217,68	55,74	25,61	191,70	49,09	25,61	69,48	17,79	25,61
RL	0,39	120,42	30,84	25,61	104,68	26,81	25,61	36,28	9,29	25,61
SE	0,53	131,39	33,64	25,61	115,39	29,55	25,61	37,01	9,48	25,61
Sjo	0,58	144,23	36,93	25,61	129,95	33,28	25,61	36,98	9,47	25,61
Sju	0,64	239,32	61,28	25,61	211,37	54,13	25,61	73,99	18,95	25,61
SM	0,39	111,70	28,60	25,61	96,21	24,64	25,61	35,63	9,12	25,61
WC	0,49	192,72	49,35	25,61	172,16	44,09	25,61	47,21	12,09	25,61
ZP	0,45	172,01	44,05	25,61	150,85	38,63	25,61	52,51	13,45	25,61

Appendix B MATLAB Scripts

B.1 Uncertainty Calculations

Implementation of the uncertainty budget and formulae discussed in section 3.2 in a MATLAB script. The respective values are used for uncertainty calculations for activity, activity concentration or dose, with and without calibration factor

```
%-------------------------------------------------------------------------
%--------Calculation of Uncertainty according to EANM guidelines-----------
%-------------------------------------------------------------------------

%----- manual input:
%-------------------
% activity values A (vector), volumes V (Vector), dose D (vector),
% if needed parameters for calculation of recovery coefficient
% activity concentration AConc (vector), description e.g. Patient Names PatNames
(string array)

%---input uncertainties
%----------------------
errC=0.076          %relative uncertainty count rate
errCArea=0.082      %relative uncertainty count rate per unit area
a=4.76              %voxel size (mm)
Q=1.0/1.1           %conversion factor cps--> Bq
errA0=0.2           %relative uncertainty calibration activity A0
errCref=0.0032      %conversion cps--> Bq
errRange=0.094      %relative uncertainty to dose constant because of range
errThres=0.123      % of best threshold value, set 0 if not needed
errRemp=0.01        %relative estimated uncertainty of empirical recovery
                    coefficient, set 0 if not needed
parametricR=0       %set 1 if parametric recovery coefficient is used

%---derived quantities
errVox=sqrt(a^2/6)          %uncertainty voxelisation
errQ2=errA0^2+errCref^2     %err(Q)^2

%---uncertainty of recovery coefficient
%---manual input of fit parameters para (vector) and covariance matrix V_b
if parametricR==1
    l=length(V);
    for i=1:l
        R(i)=Recov(para(1),para(2),para(3),V(i));
        %calculating vector with partial derivatives
        gb(1,i)=dRda(para(2), V(i));
        gb(2,i)=dRdb(para(1), para(2), V(i));
        gb(3,i)=1.0;
        gb(4,i)=dRdV(para(1), para(2), V(i));
    end
    gb_T=gb';           %transposing vector of partial derivatives
    %calculating volume related uncertainty
    for i=1:l
        d(i)=((6*V(i)/pi)^(1/3))*10;
        errV(i)=3*errVox/d(i)+errThres;
    end
    for i=1:l
        for k=1:4
            for j=1:4   %covariance matrix extended to match dimensions
                if k<4 && j< 4
                    V_bV(k,j)=V_b(k,j);
```

```
                elseif k<4 || j<4
                    V_bV(k,j)=0;
                else
                    V_bV(k,j)=errV(i)^2;
                end
            end
        end
    aux=gb_T(i,:)*V_bV;
    errR2(i)=aux*gb(:,i);   %squared uncertainty of recovery coefficient
    errR(i)=sqrt(errR2(i));
    relerrR=R(i)/errR(i);
    end
end

if exist('A') %activity
    l1=length(A);
    %calculating volume related uncertainty
    for i=1:l1
        d(i)=((6*V(i)/pi)^(1/3))*10;
        errV(i)=3*errVox/d(i)+errThres;
    end
    %calculated total uncertainty
    for i=1:l1
        errA(i)=A(i)*sqrt(errC^2+(1.0/Q^2)*errQ2+errV(i)^2);
        RelerrA(i)=(errA(i)/A(i))*100;
    end

    %---printing output
    %------------------
    fid=fopen ("Uncert_Activity.txt", 'wt')
    text1=sprintf("Uncertainty of activity values\n")
    text2=sprintf("Patient\tV_VOI(mL)\tmeasured A(MBq)\tabsolute Uncer.
                   (MBq)\trelative Uncer (per cent)\n")
    fprintf(fid, text1)
    fprintf(fid, text2)
    for i=1:l1
        text3=sprintf("%s\t%6.3f\t%6.3f\t\t%6.3f\t%6.3f\n",PatNames(i), V(i),
                    A(i),errA(i),RelerrA(i));
        fprintf(fid, text3)
    end
    fprintf(fid, "Fractional uncertainties\n")
    fprintf(fid, "Volume uncertainty\nVolume(mL)\tUncer(V) (mL)\tUncer(V)
                   (per cent), Uncer(V Voxel) (mL)\tUncer (V Threshold)(mL)\n")
    for i=1:l1
        text4=sprintf("%6.3f\t%6.3f\t%6.3f\t%6.3f\t%6.3f\n",V(i), (errV(i)*d(i)),
                    errV(i)*100, errVox, errThres);
        fprintf(fid, text4)
    end
elseif exist ('AConc')    %activity concentration
    l2=length(AConc);
    %------total uncertainty
    for i=1:l2
        if parametricR==0
            errR(1:l2)=errRemp;
        end
        errAConc(i)=AConc(i)*sqrt(errCArea^2+errQ2+errR(i)^2);
        RelerrAConc(i)=errAConc(i)/AConc(i);
    end

    %---printing output
    %------------------
    fid=fopen ("Uncert_A_Conc.txt", 'wt')
    text1=sprintf("Uncertainty of activity concentration values\n")
```

```
    text2=sprintf("Patient\tmeasured AConc(Bq/mL))\tabsolute Uncer.
                  (Bq/mL)\trelative Uncer (per cent)\n")
    fprintf(fid, text1)
    fprintf(fid, text2)
    for i=1:12
        text3=sprintf("%s\t%6.3f\t%6.3f\t%6.3f\n",PatNames(i),
                    AConc(i),errAConc(i),RelerrAConc(i));
        fprintf(fid, text3)
    end
    fprintf(fid, "Recovery Coefficient Uncertainty (per cent)\n")
    ll=length(errR);
    for i=1:12
        text12=sprintf("%6.3f\n",errR(i))
        fprintf(fid, text12)
    end
elseif exist ('D')    %dose
    l3=length(D);
    if parametricR==0
        errR(1:12)=errRemp;
    end
    for i=1:13
        errAConc2(i)=errCArea^2+errQ2+errR(i)^2
        errD(i)=D(i)*sqrt(errAConc2(i)+errRange^2);
        RelerrD(i)=errD(i)/D(i);
    end

    %---printing output
    %------------------
    fid=fopen ("Uncert_Dose.txt", 'wt')
    text1=sprintf("Uncertainty Dose Evaluation\n")
    text2=sprintf("Patient\t Dose (Gy)\t abs. Uncert. (Gy)\t rel. Uncert.
                  (per cent)\t AConc rel Uncert. \n")
    fprintf(fid, text1)
    fprintf(fid, text2)
    for i=1:13
        text3=sprintf("%s\t%6.3f\t%6.3f\t%6.3f\t%6.3f\n",PatNames(i), D(i),
                    errD(i), RelerrD(i)*100, sqrt(errAConc2(i)));
        fprintf(fid, text3)
    end
    fprintf(fid, "Recovery Coefficient Uncertainty (per cent)\n")
    ll=length(errR);
    for i=1:13
        text12=sprintf("%6.3f\n",errR(i))
        fprintf(fid, text12)
    end
end

%---remaining output
%-------------------
fprintf(fid, "Count Rate uncertainty\nUncer(C) (per cent) \tUncert.
             count rate/area (per cent)\n")
text5=sprintf("%6.3f\t%6.3f\n",errC*100, errCArea*100);
fprintf(fid, text5)
fprintf(fid, "Conversion factor uncertainty\nUncer(Q) (per cent)\tUncer(A0)
             (per cent)\tUncer (Cref) (per cent\n")
text10=sprintf("%6.3f\t%6.3f\t%6.3f\n",(sqrt(errQ2)*100), errA0*100,
errCref*100);
fprintf(fid, text10)
fprintf(fid, "Betas Particle Range Uncertainty (per cent)\n")
text11=sprintf("%6.3f\n",errRange*100)
fprintf(fid, text11)
fclose (fid)
```

```
%---functions
%recovery factor parameterized form, R(V)=a*exp(b*V)+c
function R=Recov(a,b,c,V)
    R=a*exp(b*V)+c;
end
%partial derivatives
function el1=dRda(b, V)      %dR/da
    el1=exp(b*V);
end
function el2=dRdb(a, b, V)   %dR/db
    el2=a*V*exp(b*V);
end
function el3=dRdV(a, b, V)   %dR/dV
    el3=a*b*exp(b*V);
end
```

B.2 Evaluation of Dose Distribution

MATLAB script for the construction of a dose distribution from several activity concentration profiles retrieved from the layer with the highest activity concentration and subsequent evaluation of this dose distribution.

```
%-------------------------------------------------------------------------
%---------------Dose Calculation from activity distribution---------------
%---------------for all patients, layer with highest A Conc---------------
%-------------------------------------------------------------------------

%----- manual input:
%-------------------
%description e.g. Patient Names PatNames (string array)
%position of AConc profiles pixels (vector)
%calculated doses to tumour and healthy liver CalcDose(Matrix)
%respective uncertainties CalcDoseErr(Matrix)
%if necessary recovery coefficient RecovCeoff (vector)

close all
AConcData={};        %cell with input data
DoseData={};         %cell with output data
filenamen=dir('*.xlsx');
l1_out=size(filenamen,1);
GradValue=10.0;      %exponential value for decrease of concentration values
Neighbour=1;         %moving mean over how many neighbours?
doRecov=0;           %dose values modified with recovery coefficient?

%---reading in files, creating position vectors
%-----------------------------------------------
for i=1:l1_out
    HorPos(1)=Pixels(i,1);  %starting position
    VertPos(1)=Pixels(i,3);
    aux1=(Pixels(i,2)-Pixels(i,1))/17.0;
    aux2=(Pixels(i,4)-Pixels(i,3))/17.0;
    for j=2:18              %creating the grid
        HorPos(j)=Pixels(i, 1)+aux1*(j-1);
        VertPos(j)=Pixels(i, 3)+aux1*(j-1);
    end
    AConcData{i,1}=HorPos;  %array of positions of AConc profiles
    AConcData{i,2}=VertPos;
    %reading in excel sheets
    temptable=xlsread(filenamen(i).name);
    aux1=size(temptable, 2);
```

```
    %array of each position assigned to a value
    HorPixels=temptable(:, (2:3:aux1/2));
    % corresponding array of concentration values
    HorValues=temptable(:, (3:3:aux1/2));
    VerPixels=temptable(:, ((aux1/2)+2:3:aux1));
    VerValues=temptable(:, ((aux1/2)+3:3:aux1));
    %saving to cell
    AConcData{i, 3}=HorPixels;
    AConcData{i, 4}=HorValues;
    AConcData{i, 5}=VerPixels;
    AConcData{i, 6}=VerValues;
    l2_out=size(HorPixels,2);
end

%---creating activity concentration distribution
%-----------------------------------------------
for i_out=1:l1_out
    k=1;
    for i=1:l2_out %reading out of cell into arrays
        Horizontal(:, k)=AConcData{i_out, 3}(:, i);
        Horizontal(:, k+1)=AConcData{i_out, 4}(:, i);
        Vertical(:, k)=AConcData{i_out, 5}(:, i);
        Vertical(:, k+1)=AConcData{i_out, 6}(:, i);
        k=k+2;
    end
    HorPos=AConcData{i_out, 1};
    VertPos=AConcData{i_out, 2};
    l=length(Vertical(:, 1));
    l2=length(Horizontal(:,1));
    if l~=l2    %checking quadratic matrix, other configuration would not work
        print "Error no quadratic Field of View"
    end
    Aux1=1:l;
    NoVert=length(VertPos);
    NoHor=length(HorPos);
    k=1;
    j=1;
    %matching profile positions (VertPos) to pixel position
    while j<=NoVert
        xold=inf;
        for i=1:l
            x=abs(VertPos(j)-Vertical(i,j));
            if x < xold
                xold=x;
                VertPlace(k)=i;
            end
        end
        j=j+2;
        k=k+1;
    end
    k=1;
    j=1;
    while j<=NoHor
        xold=inf;
        for i=1:l
            x=abs(HorPos(j)-Horizontal(i,j));
            if x < xold
                xold=x;
                HorPlace(k)=i;
            end
        end
        j=j+2;
        k=k+1;
```

```
end
for j=1:(NoVert/2)
    for i=1:l  %creating decrease to both sides of activity profile
        if i<=VertPlace(j)
            VertMulti(i,j)=(l-VertPlace(j))+i;
        else
            VertMulti(i,j)=l-(i-VertPlace(j));
        end
    end
    %accentuating decrease with an exponential factor defined above
    VertMulti(:,j)=VertMulti(:,j).^GradValue;
    AuxMax=max(VertMulti(:,j));
    AuxVar=1.0/AuxMax;
    VertMulti(:,j)=VertMulti(:,j)*AuxVar;
end
for j=1:(NoHor/2)
    for i=1:l
        if i<=HorPlace(j)
            HorMulti(i,j)=(l-HorPlace(j))+i;
        else
            HorMulti(i,j)=l-(i-HorPlace(j));
        end
    end
    HorMulti(:,j)=HorMulti(:,j).^GradValue;
    AuxMax=max(HorMulti(:,j));
    AuxVar=1.0/AuxMax;
    HorMulti(:,j)=HorMulti(:,j)*AuxVar;
end
%creating distribution from profiles
DataGrid=Aux1'*Aux1;
AuxDataGrid=DataGrid;
HorDataGrid=DataGrid;
VertDataGrid=DataGrid;
for j=2:2:NoVert
    for k=1:l
        AuxDataGrid(:,k)=Vertical(:,j); %placing activity profile in each row
        %multiplying profile with decreasing factor generated above,
        %value decreases the more the further from real position
        AuxDataGrid(:,k)=AuxDataGrid(:,k).*VertMulti(k, (j/2));
    end
    VertDataGrid=VertDataGrid+AuxDataGrid; %summing vertical distributions
end
for j=2:2:NoHor
    for k=1:l
        AuxDataGrid(k,:)=Horizontal(:,j);
        AuxDataGrid(k,:)=AuxDataGrid(k,:).*HorMulti(k, (j/2));
    end
    HorDataGrid=HorDataGrid+AuxDataGrid; %summing horizontal distributions
end
%creating the full AConc distribution
DataGrid=VertDataGrid+HorDataGrid;
%Renormalization
N1(1)=max(max(Vertical));
N1(2)=max(max(Horizontal));
N3=mean(N1);
Temp1=max(max(DataGrid));
Temp2=N3/Temp1;
DataGrid_Norm=DataGrid.*Temp2;
```

```
    %---------calculating D from A Conc
    %---D(Gy)=(49.67e-6/1.04*c(Bq/cm^3)
    %----------------------------------
    for i=1:size(DataGrid_Norm,1)
        for j=1:size(DataGrid_Norm,2)
            Dose(i,j)=(47.8e-6.*DataGrid_Norm(i,j));
        end
    end
    %---applying a moving mean over next neighbours to smooth out artefacts
    NoNeigh=((2*Neighbour)+1)^2;
    for i=1+Neighbour:(l-Neighbour)
      for j=1+Neighbour:(l-Neighbour)
          x=1;
          for k=-Neighbour:1:Neighbour
              for k2=-Neighbour:1:Neighbour
                  x=x+Dose(i+k, j+k2);
              end
          end
          xMean=x/NoNeigh;
          Dose_Mean(i,j)=xMean;
      end
    end
    %creating output
    DoseData{i_out, 1}=DataGrid_Norm;
    DoseData{i_out, 2}=Dose;
    DoseData{i_out, 3}=Dose_Mean;
    %applying a recovery coefficient if needed
    if doRecov==1
        Dose_Recov=Dose.*RecovCoeff(i_out);
        DoseData{i_out, 4}=Dose_Recov;
    end
end

%----sorting dose values from matrix to predefined intervals
%-----------------------------------------------------------
for i_out=1:l1_out
    Dose=DoseData{i_out, 2}(:,:);
    i1=length(Dose);
    %creating vector for sorting dose values to compare with
    %calculated values for DT and DNT
    auxVec(1)=CalcDose(i_out,1)-CalcDoseErr(i_out,2);
    auxVec(2)=CalcDose(i_out,1)+CalcDoseErr(i_out,2);
    auxVec(3)=CalcDose(i_out,2)-CalcDoseErr(i_out,1);
    auxVec(4)=CalcDose(i_out,2)+CalcDoseErr(i_out,1);
    for ii=1:4
        if auxVec(ii)<0
            auxVec(ii)=0.0;
        end
    end
    aux3=max(max(Dose));
    CalcGrid(2:5)=auxVec;
    CalcGrid(1)=aux3*0.05; %throwing away lowest 5 % of values
    CalcGrid(6)=inf;
    i3=length(CalcGrid);
    CalcGridCount(1:i3-1)=0;
    l=1;
    ll=1;
    lll=1;
    for i=1:i1 %sorting values into the intervals
        for j=1:i1
            for k2=2:i3
                 if Dose(i,j)<=CalcGrid(k2) && Dose (i,j) > CalcGrid(k2-1)
                    CalcGridCount(k2-1)=CalcGridCount(k2-1)+1;
```

```
                end
            end
            if Dose(i, j) >= CalcGrid(1)
                %putting all dose values from the matrix in one vector
                to use for histogram plot
                Scatterplot(l)=Dose(i,j);
                l=l+1;
            end
        end
    end
    %creating output
    aux7=length(Scatterplot);
    Aux_Scatter=(1:aux7);
    DoseData{i_out, 7}=aux3;
    DoseData{i_out, 8}=CalcGrid;
    DoseData{i_out, 9}=CalcGridCount;
    DoseData{i_out, 12}=Scatterplot;
    DoseData{i_out, 13}=Aux_Scatter;
    %if desired do the same with recovery coefficient corrected dose
    if doRecov==1
        Dose_Recov=DoseData{i_out, 4}(:,:);
        aux6=max(max(Dose_Recov));
        CalcGridCount_Recov(1:i3-1)=0;
        for i=1:i1
            for j=1:i1
                for k2=2:i3
                    if Dose_Recov(i,j)<=CalcGrid(k2) && Dose_Recov (i,j) >
                    CalcGrid(k2-1)
                        CalcGridCount_Recov(k2-1)=CalcGridCount_Recov(k2-1)+1;
                    end
                end
                if Dose_Recov(i, j) >= CalcGrid(1)
                    Scatterplot_Recov(ll)=Dose_Recov(i,j);
                    ll=ll+1;
                end
            end
        end
        aux10=length(Scatterplot_Recov);
        Aux_Scatter_Recov=(1:aux10);
        DoseData{i_out, 10}=CalcGridCount_Recov;
        DoseData{i_out, 14}=Scatterplot_Recov;
        DoseData{i_out, 15}=Aux_Scatter_Recov;
    end
    %cleaning up
    clear GridVec GridCount CalcGrid CalcGridCount CalcGridCount_Recov
          Scatterplot Aux_Scatter Scatterplot_Recov Aux_Scatter_Recov
end

%---evaluating max and mean dose to tumour and healthy liver
%-------------------------------------------------------------
for i_out=1:l1_out
    DoseVec=DoseData{i_out, 12};
    j1=length(DoseVec);
    aux1a=max(DoseVec);
    j=1;
    k=1;
    for i=1:j1
        %D greater than 80% of max is considered tumour dose
        if DoseVec(i)>=aux1a*0.8
            DTVec(j)=DoseVec(i);
            j=j+1;
        elseif DoseVec(i)>=aux1a*0.1 && DoseVec(i) < aux1a*0.8
```

```
            %D greater than 5% and lower than 70 % of max is considered
             healthy liver dose
            DNTVec(k)=DoseVec(i);
            k=k+1;
        end
    end
    DTmean=mean(DTVec);       %mean dose to tumour
    DNTmean=mean(DNTVec);     %mean dose to healthy tissue
    %creating output
    Output(i_out, 1)=aux1a  %max. dose to tumour
    Output(i_out, 2)=DTmean
    Output(i_out, 3)=DNTmean
    DoseData{i_out, 16}=DTVec;
    DoseData{i_out, 17}=DNTVec;
    %if desired do the same with recovery coefficient corrected values
    if doRecov==1
        DoseVec_Recov=DoseData{i_out, 14};
        j2=length(DoseVec_Recov);
        aux1b=max(DoseVec_Recov);
        j=1;
        k=1;
        for i=1:j2
            if DoseVec_Recov(i)>=aux1b*0.8
                DTVec_Recov(j)=DoseVec_Recov(i);
                j=j+1;
            elseif DoseVec_Recov(i)>=aux1b*0.1 && DoseVec_Recov(i)< aux1b*0.8
                DNTVec_Recov(k)=DoseVec_Recov(i);
                k=k+1;
            end
        end
        DTmean_Recov=mean(DTVec_Recov);
        DNTmean_Recov=mean(DNTVec_Recov);
        Output(i_out, 4)=aux1b
        Output(i_out, 5)=DTmean_Recov
        Output(i_out, 6)=DNTmean_Recov
        DoseData{i_out, 18}=DTVec_Recov;
        DoseData{i_out, 19}=DNTVec_Recov;
    end
    %clearing up
    clear DoseVec DoseVecRecov DTVec DNTVec DTVec_Recov DNTVec_Recov
end

%---creating plots
%-----------------
i_plot=1
for i_out=1:11_out
    Dose=DoseData{i_out, 2};
    Dose_Mean=DoseData{i_out, 3};
    Dose_Vec=DoseData{i_out, 12};
    LinePos=DoseData{i_out, 8};
    auxtitle=sprintf("Dose Distribution Patient %s", PatNames (i_out));
    auxtitle2=sprintf("Smoothed Dose Distribution Patient %s", PatNames (i_out));
    auxtitle3=sprintf("Dose Histogram Patient %s", PatNames (i_out));
    %creating surface (3D) plot of dose distribution
    figure(i_plot)
        colormap (jet)
        view(-135,65)
        surf(Dose, 'DisplayName', 'Dose (Gy)', 'FaceColor', 'interp')
        colorbar
        xlabel ("(mm)")
        ylabel ("(mm)")
        zlabel ("Dose (Gy)")
        title (auxtitle)
```

```
    %creating surface (3D) plot of dose distribution smoothed with moving mean
    figure(i_plot+1)
        colormap (jet)
        view(-135,65)
        surf(Dose_Mean, 'DisplayName', 'Dose (Gy)', 'FaceColor', 'interp')
        colorbar
        xlabel ("(mm)")
        ylabel ("(mm)")
        zlabel ("Dose (Gy)")
        title (auxtitle2)
    %creating histogram plot of all dose values
    figure(i_plot+2)
        hold on
            histogram(DoseData{i_out, 12}, 'DisplayName', 'Measured Data')
            if doRecov==1 %if desired also for recovery corrected
                histogram(DoseData{i_out, 14}, 'DisplayName',
                    'Recovery Coeff. Data')
                legend
            end
        hold off
        xlabel ("Dose (Gy)")
        ylabel ("Occurrence")
        title (auxtitle3)
        auxPlot=ylim
        %marking calculated ranges for DT and DNT in histogram plots
        line([LinePos(2) LinePos(2)],[auxPlot(1) auxPlot(2)], 'linestyle', '--',
        'color', 'black');
        line([LinePos(3) LinePos(3)],[auxPlot(1) auxPlot(2)], 'linestyle', '--',
      'color', 'black');
        line([LinePos(4) LinePos(4)],[auxPlot(1) auxPlot(2)], 'linestyle', '--',
     'color', 'black');
        line([LinePos(5) LinePos(5)],[auxPlot(1) auxPlot(2)], 'linestyle', '--',
     'color', 'black');
        if doRecov==1 %if desired also for recovery corrected
            Dose_R=DoseData{i_out, 4}
            auxtitle4=sprintf("Dose Distribution corrected with recovery
             coefficient Patient %s", PatNames (i_out))
            figure(i_plot+3)
                    colormap (jet)
                    view(-135,65)
                    surf(Dose_R, 'DisplayName', 'corrected Dose (Gy)',
                    'FaceColor', 'interp')
                    colorbar
                    xlabel ("(mm)")
                    ylabel ("(mm)")
                    zlabel ("corrected Dose (Gy)")
                    title (auxtitle)
            i_plot=i_plot+1;
        end
    i_plot=i_plot+3
end

%---saving plots to .pdfs
for j=1:i_plot
    fileaux(j)=sprintf("Dose_Patients_%ia", j)
    fileaux2(j)=sprintf("%s.pdf", fileaux{j})
    ff=figure(j)
    set (ff, 'PaperOrientation', 'Landscape', 'PaperType', 'a5')
    box on
    print('-bestfit', ff, fileaux{j}, "-dpdf")
end
close all
```

```
%---data output to text file
%---------------------------
fid=fopen ("Dose_Patient_Data.txt", 'wt')
text1=sprintf("Dose Evaluation out of activity concentration distribution\n")
text2=sprintf("Patient\t max. Dose (Gy)\t mean Tumour Dose (Gy)\t
             mean Liver Dose (Gy)\n")
fprintf(fid, text1)
fprintf(fid, text2)
for i=1:l1_out      %printing dose values
    text3a=sprintf("%s\t%6.3f\t%6.3f\t%6.3f\t\n",PatNames(i), Output(i, 1),
             Output(i, 2), Output(i, 3))
    fprintf(fid, text3a)
end
if doRecov==1       %if desired printing recovery corrected dose values
    text3=sprintf("Dose Evaluation out of activity concentration distribution
             including recovery coefficient\n")
    text4=sprintf("Patient\t max. Dose (Gy)\t mean Tumour Dose (Gy)\t mean Liver
             Dose (Gy)\n")
    fprintf(fid, text3)
    fprintf(fid, text4)
    for i=1:l1_out
        text3=sprintf("%s\t%6.3f\t%6.3f\t%6.3f\t\n",PatNames(i), Output(i, 4),
             Output(i, 5), Output(i, 6))
        fprintf(fid, text3)
    end
end

%printing output from matching doses with intervals done above
text5=sprintf("Occurrence in Intervals defined by Dose Calculation\n")
fprintf(fid, text5)
    for i=1:l1_out
        CalcGrid=DoseData{i, 8};
        CalcGridCount=DoseData{i, 9};
        text3=sprintf("%s\t0 - %6.3f\t%6.3f\t - %6.3f\t%6.3f\t - %6.3f\t%6.3f\t -
             %6.3f\t%6.3f\t - %6.3f\t%6.3f\n",PatNames(i), CalcGrid(2),
CalcGridCount(1),CalcGrid(3), CalcGridCount(2),CalcGrid(4),
CalcGridCount(3),CalcGrid(5), CalcGridCount(4),CalcGrid(6), CalcGridCount(5))
        fprintf(fid, text3)
    end
fclose (fid)
```

Appendix C Conference Talks

C.1 MRT Dosimetry, 2nd Scientific Workshop Prague

In the course of the project *Metrology for clinical implementation of dosimetry in molecular radiotherapy* (MRT Dosimetry) the second scientific workshop with the title "*European workshop on the principles and clinical implementation of dose calculation in molecular radiotherapy"* took place in Prague, Czech Republic on 26th and 27th September 2018. The aim of this meeting was to discuss new dosimetry techniques in molecular radiotherapy, their metrological aspects and possible implementation in clinical practice.

These topics were also highlighted during the talks of the invited speakers. George Sgouros (John Hopkins University, USA) presented interesting arguments for convincing physicians to implement dosimetry, while Maurice Cox (National Physics Laboratory, UK) and Jonathan Gear (Institute of Cancer Research, UK) summarized the techniques for evaluating uncertainties explained in their paper and used during this project.

Among many other contributions to follow, dosimetry in SIRT was also discussed at length. Francesca Botta (European Institute of Oncology, ITA) explained her dosimetry approach relying on the results from the Tc-99m-MAA SPECT and during the afternoon session on the second day I got the chance to present my project in a talk titled "*Challenges in post-treatment dose calculations using image-based quantification of Y-90 SPECT/CT data*". Although at that point the project was still work in progress I received very interested and positive feedback, as quantitative Y-90 SPECT was indeed considered a novelty. Additionally I was able to include several ideas presented during the talks in my evaluation, like the approach to estimate uncertainties, and I was offered an anthropomorphic liver phantom by Jon Gear to perform further measurements.

The stay in Prague and my contribution to the workshop was also made possible by Österreichischer Verband für Strahlenschutz (ÖVS), which thankfully covered my travel expenses.

On the next pages the submitted abstract and my presentation can be found.

C.1.1 Abstract

TITLE

Challenges in post-treatment dose calculations using image-based quantification of Y-90 SPECT/CT data

AUTHOR

K. Lotter, M. Diemling, A. Sohlberg, H. Wiedner, A. Haug, FJ. Maringer

ABSTRACT

Quantifying SPECT/CT data from treatment of liver carcinoma with Y-90 microspheres poses unique challenges, as a continuous bremsstrahlung spectrum is used for acquisition. In this study the commercially available software package HybridRecon (Hermes Medical Solutions) is used for evaluation of images from 17 patients, a Jaszczak and a NEMA IEC Body Phantom. The Monte-Carlo based approach for scatter and attenuation correction and collimator modelling allows quantification and tries to overcome the Y-90 specific challenges.

The whole dataset was analyzed and a large influence of the VOI threshold selection on the resulting total activities was found. To counter this problem a mathematical relation between threshold and activity was investigated, real and measured liver volumes, activity concentrations and energy dose were estimated.

In conclusion this study is a proof of concept of quantitative Y-90 SPECT reconstruction with credible results for measured activities, albeit high uncertainties for some patients.

C.1.2 Presentation

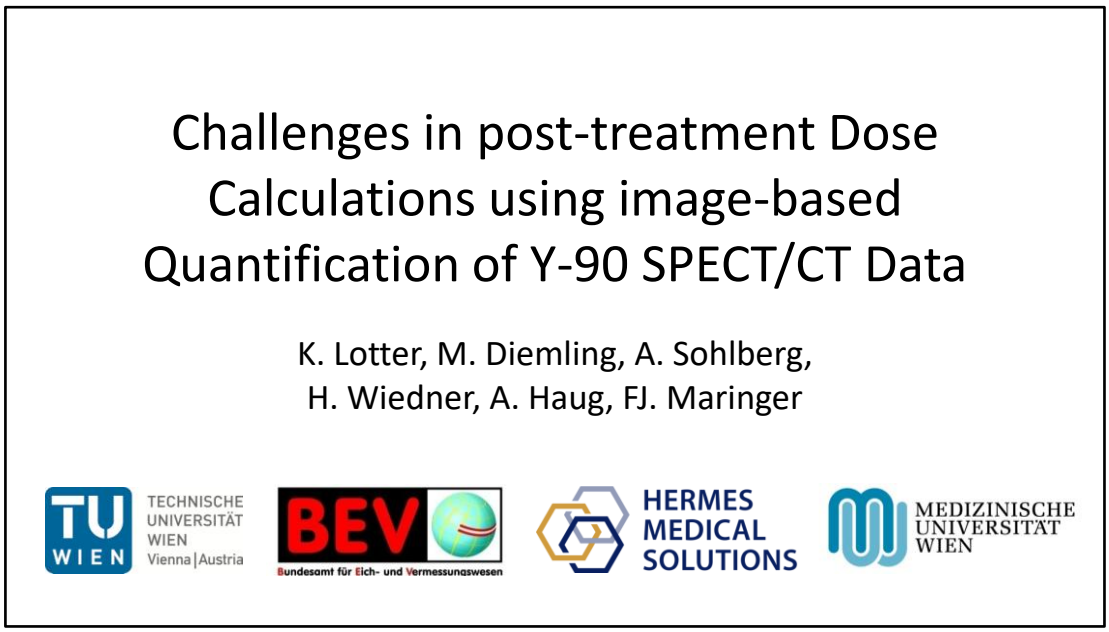

- Motivation
- Study details
- Jaszczak & Body Phantom Measurements
- VOI Threshold Selection
- Total Activity & Volume
- Dose Calculations
- Conclusions & Outlook

Cancer Treatment using Y-90

- Treatment of non-resectable liver cancer using Y-90 SIRT
- Applicable for primary carcinoma and metastasis
- Y-90: pure high-energy β-emitter, 64 h half-life
- Transarterial infusion of active microspheres (20 – 30 µm)
- Staying permanently in the patient's body
- Evaluation of doses to healthy liver and tumour

  → quantified post treatment imaging

SIRT post-treatment Imaging

- Low probability branch of e^- - e^+ pair generation → PET
- SPECT possible, utilizing bremsstrahlung photons
- Continuous spectrum complicates reconstruction and quantification
- Software with Monte-Carlo based scatter and attenuation correction and collimator modelling

→ Quantification of SIRT SPECT/CT data

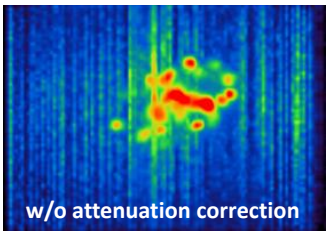

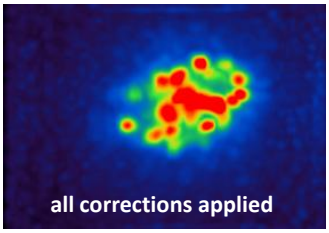

This study

- 17 SIRT patients treated at *AKH Vienna* between May 2017 and May 2018
- *Sirtex* resin-based *SIR-Spheres*
- Applied activities 0.58 – 2.77 GBq
- SPECT/CT using *Siemens Symbia Intevo* with ME-Collimator
- Reconstruction & Evaluation with *Hermes Medical Solutions' Hybrid Recon* 2.2 & *Hybrid Viewer* 3.0
- Measurement of Jaszczak and NEMA IEC Body Phantom

Phantom Measurements @ AKH Vienna

Jaszczak Phantom

A = 564 MBq

$t_{measurement}$ = 15, 30 min

Necessary for calibration

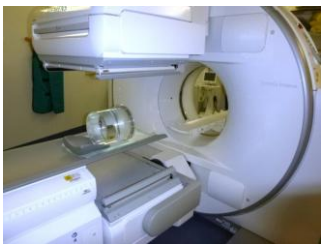

NEMA IEC Body Phantom

A = 465 MBq

$t_{measurement}$ = 15, 30 min, 8 h

Evaluation of reconstruction

Phantom Measurements @ AKH Vienna

Jaszczak Phantom

For correct volume, activity 3 % underestimated

Mean SUV ≈ 1.0

Very precise results

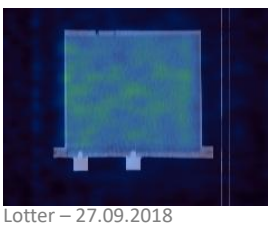

NEMA IEC Body Phantom

For spheres activity severely underestimated

Total activity correct, but VOI definition arbitrary

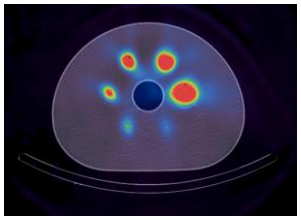

Quantitative Evaluation

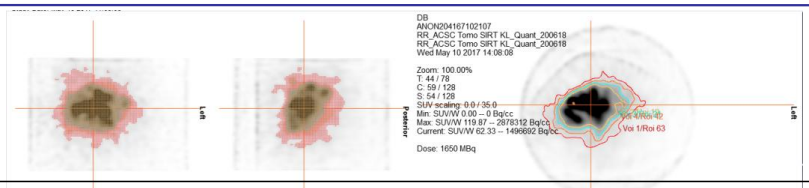

DB	SUV min	SUV max	Bq/cc	V (cm^3)	A tot(MBq)
Voi 1	3,16	119,87	266050,69	7335,08	1951,50
Voi 2	11,75	119,87	600625,69	1912,25	1148,55
Voi 3	8,39	119,87	491192,97	2741,41	1346,56
Voi 4	5,50	119,87	382051,22	4140,95	1582,05
applied			**V_{Liver} ca.**	2300,00	1650,00

→ Large impact of threshold selection for Volume of Interest (VOI)

Threshold Selection

- Stringent criteria necessary
- Evaluation of dataset with 4 different VOI thresholds
  - 20 % of max. SUV value (Shcherbinin et.al., 2008)
  - SUV = 4.0
- Thresholds with background corrections tested but discarded

Relation between Threshold and Activity

- Mathematical relation between VOI threshold (MBq/mL) and VOI total activity investigated
- Best guess $A_{tot} = \frac{a}{A_{Conc}} * b$
- Fit using nonlinear least-squares Marquardt-Levenberg algorithm; parameters a, b

→ Calculation of threshold yielding correct total activity

→ Investigation of common behaviour

Relation between Threshold and Activity - SF

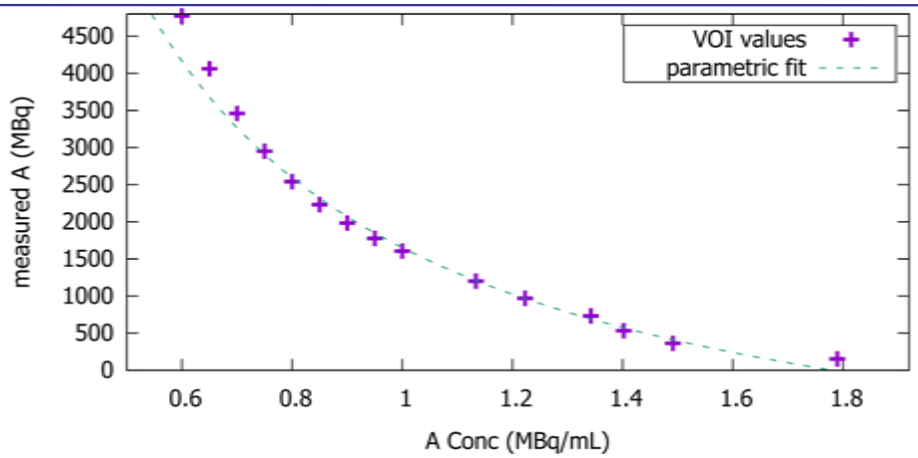

Threshold Selection

- Stringent criteria necessary
- Evaluation of dataset with different VOI thresholds
  - 20 % of max. SUV value (Shcherbinin et.al., 2008)
  - SUV = 4.0
- Thresholds with background corrections tested but discarded
- Excluding outliers best common threshold is 6,4 % of max. SUV value

Total activity

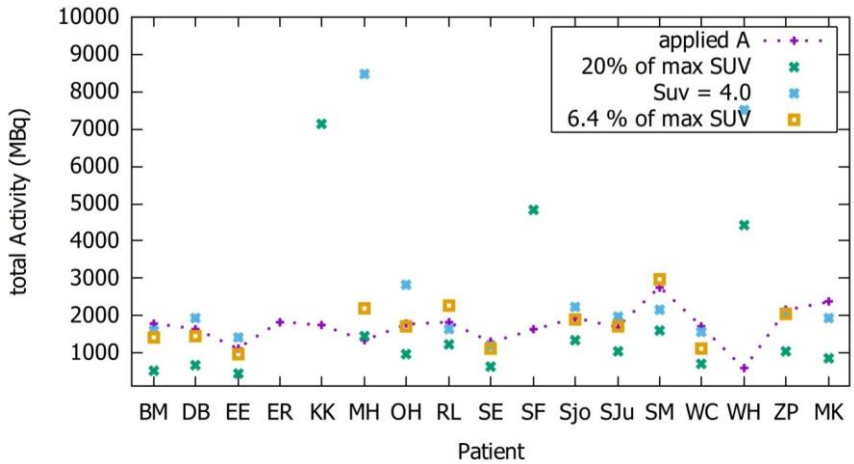

- 20 % threshold yields correct estimation of V
- Confirming Shcherbinin et.al.
- Activity underestimated

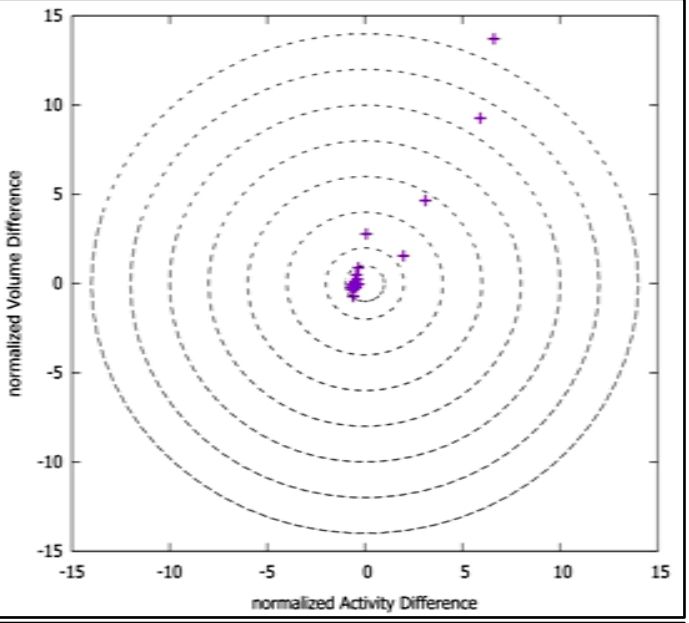

Activity → Dose ?

Main challenge: activity very inhomogeneously distributed

Constant dose:

$$\overline{D}(Gy) = \frac{49.67 * A_0\ (GBq)}{M(kg)}$$

Example: A= 1.12 GBq

D= 36 Gy

$$D(Gy) = \frac{49.67 * 10^{-6}}{1.04} * c(Bq\ cm^{-3})$$

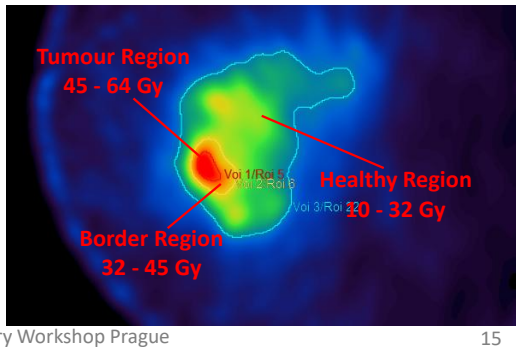

Formulae from:
Dieudonne, A., Hobbs, R., et al.,
Clin. Transl. Imaging (2016) 4:273-282

More refined approach

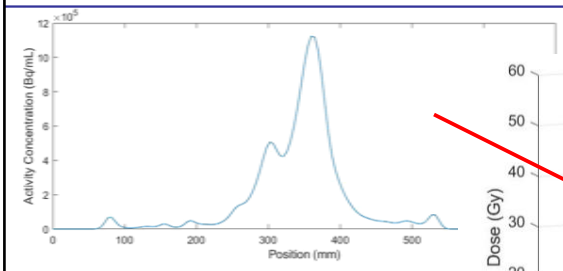

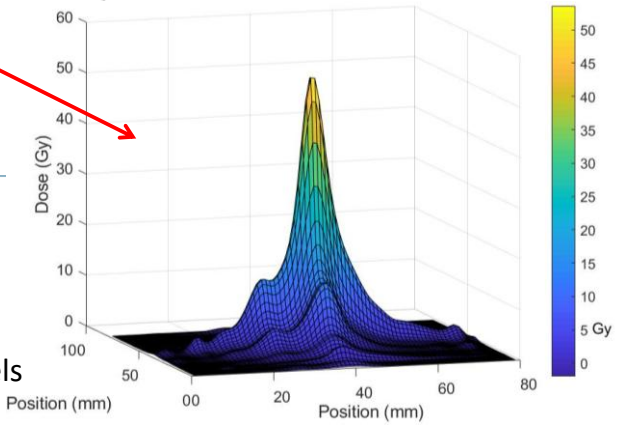

Calculating a dose profile out of the activity distribution

But: only for one layer and interaction between voxels is not taken into account

16

Conclusions & Outlook

- Quantitative reconstruction yields reasonable results
- Criteria for VOI thresholds improve reproducibility
  - 20% of max SUV for most accurate volumes as in *Shcherbinin et.al.*
  - Mathematical relation for best threshold value found
    → use beyond this study needs to be investigated
- Rough estimation of dose possible, but interactions between microspheres should be modelled

Outlook:

- Monte-Carlo based dose evaluation, yielding 3D dose model and values for tumour doses and healthy liver doses

Thank you for your attention!

TU WIEN TECHNISCHE UNIVERSITÄT WIEN Vienna | Austria
BEV Bundesamt für Eich- und Vermessungswesen
HERMES MEDICAL SOLUTIONS
MEDIZINISCHE UNIVERSITÄT WIEN

References

- **Dieudonne, Arnaud, et al.** Absorbed-dose calculation for treatment of liver neoplasms with Y-90 microspheres. *Clin. Transl. Imaging.* 4:273-282, 2016.
- **Shcherbinin, S., et al.** Accuracy of quantitative reconstruction in SPET/CT imaging. *Phys. Med. Biol.* 53: 4595-4604, 2008.
- **Porter, Charlotte A., et al.** Phantom and clinical evaluation of the effect of full Monte Carlo collimator modelling in post-SIRT yttrium-90 Bremsstrahlung SPECT imaging. *EJNMMI Research.* 8:7, 2018.
- **Sohlberg, Antti O. und Kajaste, Markus T.** Fast Monte Carlo-simulator with full collimator and detector modelling for SPECT. *Ann. Nucl. Med.* 26:92-98, 2011.

TU WIEN TECHNISCHE UNIVERSITÄT WIEN Vienna | Austria
BEV Bundesamt für Eich- und Vermessungswesen
HERMES MEDICAL SOLUTIONS
MEDIZINISCHE UNIVERSITÄT WIEN

C.2 ÖVS Herbsttagung 2018

On 13th November 2018 the autumn meeting of the Austrian Radiation Protection Association (Österreichischer Verband für Strahlenschutz, ÖVS) was hosted in the rooms of Bundesamt für Eich- und Vermessungswesen, Schiffamtsgasse 1-3, Vienna. The subject of the meeting named *"Strahlenschutz in der Medizin – Messtechnik"* was to discuss radiation protection in medicine and related measurement techniques. As a follow up from my contribution to the workshop in Prague I was invited to present a German version of my talk as one of four speakers scheduled for this meeting.

The talk was called "*Herausforderungen bei der Bild-basierten Dosisermittlung*". In accordance with the topic I laid more emphasis on the dosimetric aspects and on the efforts to implement routine dosimetry in clinical practice. Together with the other presentations on dosimetry I was able to introduce some new approaches to the viewer and to give insight in pending dosimetric questions.

C.2.1 Presentation

The presentation for this talk is given below.

- Dosimetrie in der molekularen Radiotherapie
- Y-90 SIRT
- Patientendaten & Phantom-Messungen
- Quantitative Auswertung
- SIRT Dosisberechnungen
- Zusammenfassung & Ausblick

Molekulare Radiotherapie

- Gruppe von Krebstherapien mit nicht-umschlossenen Quellen
- Radionuklid reichert sich an gewissen Orten im Körper an
- wird oft durch Stoffwechsel teilweise wieder ausgewaschen

→ zeitabhängige Aktivitäts- und Dosisverteilung

- genaue Dosimetrie ist schwierig und wird häufig nicht durchgeführt, nur Berechnungen vor der Behandlung

→ EMPIR Projekt zur MRT-Dosimetry

MRT DOSIMETRY

- Zusammenarbeit von Metrologie-Instituten, Kliniken und wissenschaftlichen Partnern aus ganz Europa
- seit Jahren standardisierte Dosimetrie in der Tele- und Brachytherapie
- ohne Dosimetrie unberechenbare Behandlungsergebnisse
- Gefahr von Schäden durch unnötig viel Aktivität
- gefordert durch EU-Richtlinie 2013/59/EURATOM

→ Projekt schafft Voraussetzungen für standardisierte Dosimetrie

→ unterstützt die Implementierung in den behandelnden Kliniken

Tumor Therapie mit Y-90

- Behandlung von primären Leberkarzinomen und Metastasen mit Y-90 SIRT (Selective Internal Radiation Therapy)
- Y-90: reiner hochenergetischer β-Strahler, 64 h HWZ
- transarterielle Infusion von aktiven Mikrosphären (20 – 30 µm)
- verbleiben dauerhaft im Körper
- Bestimmung der Dosis für gesundes Lebergewebe und Tumor

→ quantitative Bildgebung nach der Behandlung

SIRT Bildgebung

- Zerfallskanal mit e^- - e^+ Paarbildung → PET aber sehr geringe Intensität
- Bremsstrahlung-Photonen → SPECT
- Kontinuierliches Spektrum erschwert Rekonstruktion und Quantifizierung
- Software mit Monte-Carlo basierten Korrekturen für Streuung und Abschwächung und Modellierung des Kollimators

→ Quantifizierung der SIRT SPECT/CT Daten

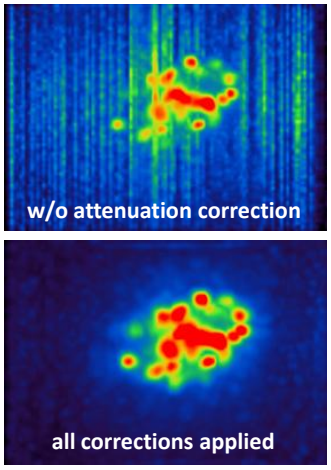

Verfügbare Daten

- 17 Patienten wurden am AKH Wien zwischen Mai 2017 und 2018 mit SIRT behandelt
- *SIR-Spheres* der Firma *Sirtex* auf Kunstharzbasis
- verabreichte Aktivitäten zwischen 0,58 – 2,77 GBq
- SPECT/CT an *Siemens Symbia Intevo* mit ME-Kollimator
- Rekonstruktion & Auswertung mit *Hybrid Recon* 2.2 & *Hybrid Viewer* 3.0 von *Hermes Medical Solutions* (Schweden)
- Messungen mit einem Jaszczak und NEMA IEC Body Phantom

Phantom-Messungen am AKH Wien

A ≈ 500 MBq, $t_{Messung}$ = 15, 30 min, 8 h

Jaszczak Phantom

notwendig zur Kalibrierung

Aktivität 3% unterschätzt,

bei realem Volumen

NEMA IEC Body Phantom

für einzelne Kugeln, wird die Aktivität deutlich unterschätzt

A_{Tot} korrekt, willkürliches VOI

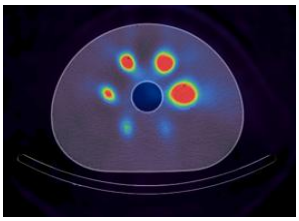

Quantitative Auswertung

$$SUV = \frac{c(A_{Bild})}{c(A_{Inj.})}$$

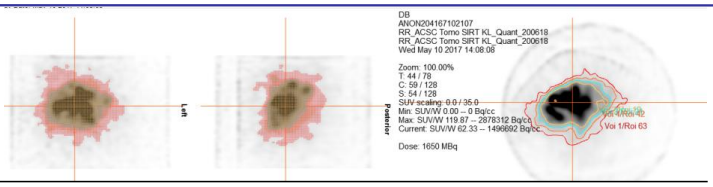

DB	SUV min	SUV max	Bq/cc	V (cm^3)	A tot(MBq)
Voi 1	3,16	119,87	266050,69	7335,08	1951,50
Voi 2	11,75	119,87	600625,69	1912,25	1148,55
Voi 3	8,39	119,87	491192,97	2741,41	1346,56
Voi 4	5,50	119,87	382051,22	4140,95	1582,05
applied			**V_{Liver} ca.**	2300,00	1650,00

→ großer Einfluss des VOI Thresholds auf die gemessene Aktivität

Wahl des Thresholds

- klares Kriterium notwendig
- Thresholds unter Einbeziehung des Hintergrunds wieder verworfen
- Auswertung des Datensatzes mit verschiedenen VOI Thresholds
  - 20 % des max. SUV Wertes (Shcherbinin et.al., 2008)
  - SUV = 4.0
- Suche nach mathematischem Zusammenhang zwischen VOI Threshold (MBq/mL) und eingeschlossener Gesamtaktivität
- Fit aller Daten → bester gemeinsamer Wert ist 6,4 % des max. SUV Wertes (Ausreißer wurden ausgeschlossen)

Gesamtaktivität

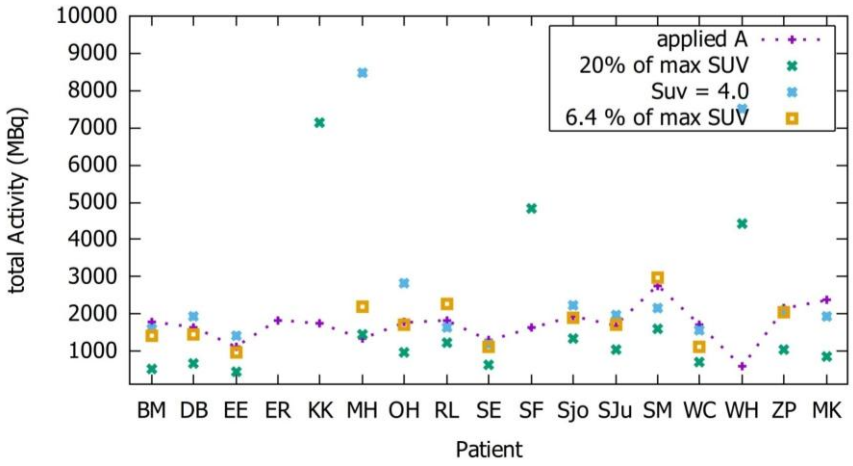

Aktivität→ Dosis ?

konstante Dosis: $\bar{D}(Gy) = \frac{49.67 * A_0\ (GBq)}{M(kg)}$

z.B.: A = 1,12 GBq, m_L = 1,7 kg → D = 32 Gy

aber: die Aktivität ist sehr inhomogen verteilt

$$D_T = \frac{49{,}67 * A_0(1-L)}{m_T\left(1+\frac{A_{NL}}{A_T}\right)} \approx 60\ Gy$$

teils nicht genau bekannt oder schwer zu bestimmen

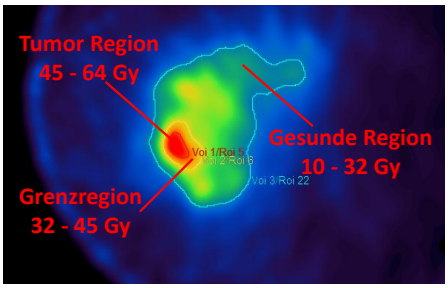

Formel aus: Dieudonne, A., Hobbs, R., et al., Clin. Transl. Img. (2016) 4:273-282

Genauere Betrachtung

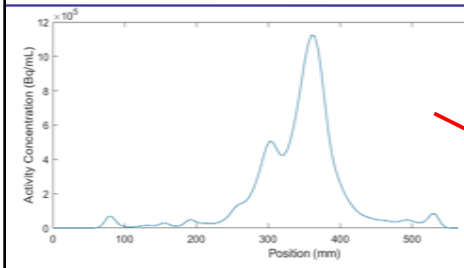

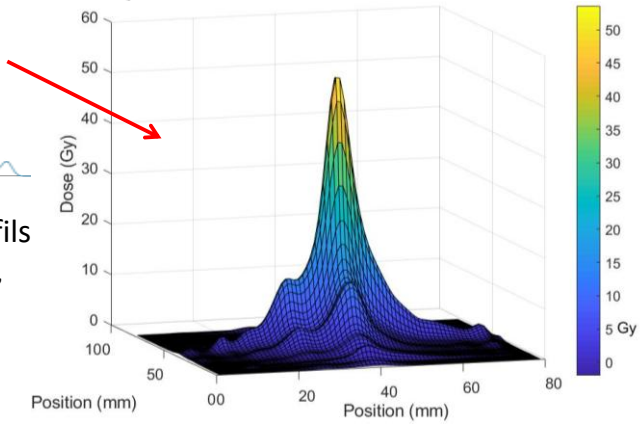

Berechnung eines Dosisprofils aus der Aktivitätsverteilung,

betrachtet aber nur eine Schicht, vernachlässigt WW zwischen Voxeln

Vergleich gemessene & gerechnete Dosis

Body Phantom

A= 0,46 GBq, A_{conc} = const.

→in jeder Kugel D = 480 Gy

Beispielpatient

A = 1,94 GBq, mehrere Tumore

D_{Tumor} ≈ 50 - 110 Gy

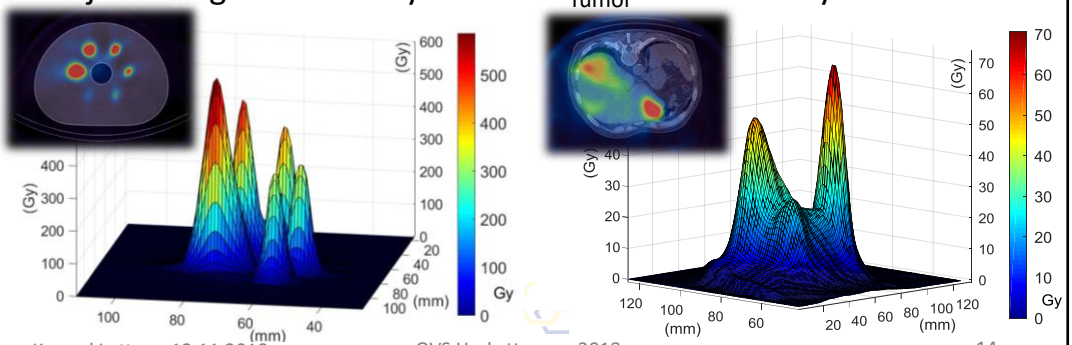

Ausblick

Weitere Messungen an 3D-gedrucktem anthropomorphen Leberphantom

Weitere Programmentwicklung:

MC basierte Dosisberechnung

→3D Dosis Model

Berücksichtigung der WW

Gesamtdosen für Tumor und gesunde Leber

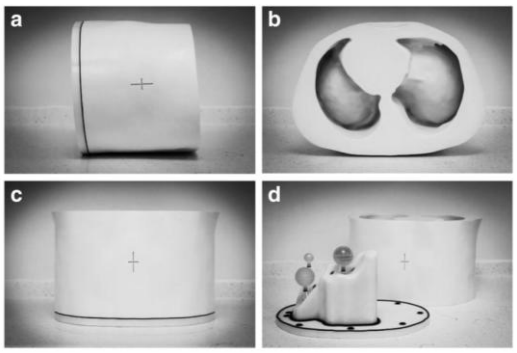

Gear, J., Craig, A., et al., EJNMMI Physics (2016) 3:17

Zusammenfassung

- Quantitative Rekonstruktion erzielt sinnvolle Resultate
- Kriterien für den Threshold erhöhen die Reproduzierbarkeit
- ungefähre Abschätzung der Dosis aus Bildgebung nach der Behandlung möglich, aber WW nicht berücksichtigt
- gute Übereinstimmung mit Formeln für Berechnungen vor der Behandlung

Entwicklung in Richtung präziserer Dosimetrie

→ genauere Bestimmung der notwendigen Aktivitätsmenge

→ bessere Vermeidung von strahleninduzierten Schäden

Vielen Dank für Ihre Aufmerksamkeit!

Literatur

- **Dieudonne, Arnaud, et al.** Absorbed-dose calculation for treatment of liver neoplasms with Y-90 microspheres. *Clin. Transl. Imaging.* 4:273-282, 2016.
- **Shcherbinin, S., et al.** Accuracy of quantitative reconstruction in SPET/CT imaging. *Phys. Med. Biol.* 53: 4595-4604, 2008.
- **Porter, Charlotte A., et al.** Phantom and clinical evaluation of the effect of full Monte Carlo collimator modelling in post-SIRT yttrium-90 Bremsstrahlung SPECT imaging. *EJNMMI Research.* 8:7, 2018.
- **Sohlberg, Antti O. und Kajaste, Markus T.** Fast Monte Carlo-simulator with full collimator and detector modelling for SPECT. *Ann. Nucl. Med.* 26:92-98, 2011.

C.3 ICRM 2019 Salamanca

The 22nd International Conference on Radionuclide Metrology and its Applications (ICRM) will take place in Salamanca, Spain from 27th to 31st May 2019. An abstract with the title "*Assessing Activity and Dose Values Computed by Image-Based Quantification of Y-90 SPECT/CT Data*" and focusing mainly on the metrological aspects of this project on Y-90 dosimetry was submitted.

The proposal was accepted and I am looking forward to present this project at ICRM 2019 as an oral presentation in the session "Radionuclide Metrology in Life Sciences". A Full Paper will be published in *Applied Radiation and Isotopes*.

The contribution will summarize the evaluations performed during this project and present results focusing on metrological aspects like the uncertainty budget and the traceability of dose evaluations. Additionally measurements on the anthropomorphic liver phantom will be performed and included as soon as AKH Vienna has sufficient capacities to allow those.

C.3.1 Abstract

TITLE

ASSESSING ACTIVITY AND DOSE VALUES COMPUTED BY IMAGE-BASED QUANTIFICATION OF Y-90 SPECT/CT DATA

AUTHOR

K. Lotter[1], M. Diemling[2], A. Sohlberg[2], H. Wiedner[3], A. Haug[4], FJ. Maringer[1, 3]

[1]*Technische Universität Wien - Technical University of Vienna, Karlsplatz 13, 1040 Wien, Austria*
[2]*HERMES Medical Solutions, Skeppsbron 44, 111 30 Stockholm, Sweden*
[3]*Bundesamt für Eich- und Vermessungswesen, Arltgasse 35, 1160 Wien, Austria*
[4]*Division of Nuclear Medicine, Medical University of Vienna, Spitalgasse 23, 1090 Wien, Austria*

KEYWORDS

SIRT, dosimetry, SPECT quantification, molecular radiotherapy, activity concentration

ABSTRACT

Selective internal radiation therapy (SIRT) is a promising treatment for liver carcinoma by injecting Y-90 bearing microspheres in the hepatic artery. Typical challenges of dose calculations involving internal radiotherapy do not apply, as the spheres get trapped permanently in the micro-vessels. Therefore, it is imminently important to determine activity and dose with an accurate and traceable method.

Utilizing the continuous bremsstrahlung spectrum, SPECT/CT images can be acquired.

In this study the commercially available software package HybridRecon (Hermes Medical Solutions) is used for evaluation of phantom measurements and data from 17 patients treated at AKH Vienna (with Y-90 activities ranging from 0.58 GBq to 2.77 GBq). The Monte-Carlo based approach for scatter and attenuation correction and collimator modelling allows quantification and yields activity concentration data.

The whole dataset was analyzed and a large influence of the Volume of Interest threshold selection on the resulting activities was found. To counter this problem a mathematical relation between threshold and activity was introduced. The accuracy of the computed results was verified by comparing applied and measured activities and the under-estimation of the activity concentration was quantified.

Using the activity concentration data different approaches for dose estimations were considered, neglecting interactions between the voxels, due to the very limited range of the emitted radiation.

Relying mainly on the phantom measurements, an uncertainty budget for activity concentration and dose was calculated and applied.

In conclusion, this study is a proof of concept of quantitative Y-90 SPECT reconstruction with credible results for measured activities, although with high uncertainties for some patients. The activity concentration values from the quantified SPECT images can be used to estimate the internal absorbed dose, making this approach much easier traceable, than calculations relying on pre-treatment Tc-99m-MAA SPECT scans. In future studies a Monte-Carlo based 3D-dose model including interactions could be envisaged.

Curriculum Vitae

Konrad Lotter, BSc
Born: 5th December 1993 in Vienna
E-mail: konradlotter@gmx.at

Education

Since 10. 2015: Technische Universität Wien

Master's programme in Technical Physics
Project on measurement of radon in water samples

2. 2017 - 7. 2017: Camlin Technologies (Switzerland) AG, Zurich

Six-month Internship at an ETH spin-off developing tuneable mid-infrared semiconductor Lasers Responsible for band gap and transmission measurements, independent work on data evaluation and development of analysis tools in Octave

2012 – 2015: Technische Universität Wien

Bachelor's programme in Technical Physics
Bachelor project on *The Analysis of elemental concentration Patterns in Ceramics from the Island Sai*

2004 – 2012: BRG Pichelmayergasse, Vienna

2012: Dr. Hans Riegel-Awards, 2nd in Physics
For the work: *Maritime Navigation in coastal Waters*

Publications and Conference Presentations

2017

H. Wiedner, K. Lotter, P. Karner, H. Friedmann, F.J. Maringer. Radon in drinking water: comparison and evaluation of two ionisation chamber activity measurement methods. *Appl Radiat Isot.* 2018 Apr, 134, pp. 477-481.

2018

K. Lotter, M. Diemling, A. Sohlberg, H. Wiedner, A. Haug, FJ. Maringer. Challenges in post-treatment dose calculations using image-based quantification of Y-90 SPECT/CT data. *European Workshop on the Principals and clinical Implementation of Dose Calculation in Molecular Radiotherapy*, Prague 2018

K. Lotter, M. Diemling, A. Sohlberg, H. Wiedner, A. Haug, FJ. Maringer. Herausforderungen bei der Bild-basierten Dosimetrie. *ÖVS Herbsttagung*, Vienna 2018

2019

K. Lotter, M. Diemling, A. Sohlberg, H. Wiedner, A. Haug, FJ. Maringer. Assessing Activity and Dose Values Computed by Image-Based Quantification of Y-90 SPECT/CT Data. *International Conference on Radionuclide Metrology and its Applications,* Salamanca 2019